TECHNICAL MEMORANDUM

643

A Study on the Spectral and Radiometric Specifications of a Post-EPS Microwave Imaging Mission

Carole Peubey, William Bell, Peter Bauer and Sabatino Di Michele

Research Department

May 2011

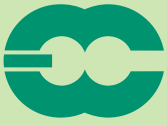

European Centre for Medium-Range Weather Forecasts
Europäisches Zentrum für mittelfristige Wettervorhersage
Centre européen pour les prévisions météorologiques à moyen terme

Series: ECMWF Technical Memoranda

A full list of ECMWF Publications can be found on our web site under:
http://www.ecmwf.int/publications/

Contact: library@ecmwf.int

European Centre for Medium-Range Weather Forecasts
Shinfield Park, Reading, RG2 9AX, England

Abstract

This study contributes to the specification of EUMETSAT's post-EPS Microwave Imager and Sounder missions and makes use of tools developed as part of previous similar studies at ECMWF, including 1D-Var and information content analyses as well as observing system experiments. The sensitivity of analysis and forecast errors to spectral shifts in microwave channels was investigated. The maximum tolerable drift for temperature sounding channels has been found to be around 1.5 MHz. The use of a variational correction scheme significantly reduced the negative impact of larger drifts. Cross polarisation errors were shown to cause biases in retrieved ocean surface wind speed (10%) and column water vapour (3%). The specification of channels in the range 15-22 GHz and 31-37 GHz, given radio frequency protection issues, was investigated. A framework for the quantitative analysis of resolution and sampling strategies was developed, based on linear estimation theory and using entropy reduction as a *figure of merit*. The capability of digital detection (*spectrally resolved microwave radiometry*) to reproduce conventional analog passbands was investigated. Finally data from F18 SSMIS, the third in a series of five combined imager-sounder instruments, was assessed through observing system experiments as part of an ongoing assessment of the potential for combined imaging and sounding.

Contents

Executive Summary

This report describes the results of a EUMETSAT study on the refinement of the spectral and radiometric specifications of a post-EPS (now *EPS-Second Generation*) microwave imaging (MWI) mission. The study forms part of a larger effort, supported by EUMETSAT and ESA, to define options for the post-EPS microwave sounding (MWS) and imaging missions. The study aimed to support phase-0 and phase-A studies by assessing several potentially important performance characteristics of the MWI mission. The study made extensive use of tools developed as part of similar previous studies carried out by ECMWF, including observing system experiments (OSEs), 1D-Var analyses and information content (IC) analyses.

The study was concerned with the following issues:

- The specification of channel passband stability (**WP2000**)
- The specification of cross polarisation tolerance (**WP3000**)
- The selection of channels in the 15-22 GHz and 31-37 GHz regions, given regulations governing the allocation of bandwidth in this part of the microwave spectrum (**WP4100**)
- The use of digital detection (*spectrally resolved radiometry*) in the 50-60 GHz spectral region (**WP4200**)
- The development of a scheme for the quantitative evaluation of sampling and resolution strategies for microwave sounders and imagers (**WP5000**)
- The evaluation of data from F18 SSMIS, as part of an ongoing assessment of the on-orbit performance of combined imager/sounders (**WP6000**)

In **WP2000** off-line radiative transfer modelling was used to parametrize the effect of channel shift errors on measured brightness temperatures for both temperature and moisture sounding channels. For temperature sounding channels (50-60 GHz) a drift of 10 MHz induced errors of 0.2K which is expected to adversely affect analyses and forecasts. For the water vapour sounding channels (at 183 GHz) the equivalent error was 0.003K which is not expected to adversely affect analyses and forecasts.

Observing system experiments were conducted in which brightness temperature errors, resulting from specified frequency drifts in the range 1.5-20 MHz, were added to measurements from a constellation of three AMSU-A instruments. For shifts of 5 MHz or larger analyses and forecasts were measurably degraded, even with the use of variational bias correction. Variational bias correction nonetheless helps to partly reduce the negative impact of the frequency drifts. Drifts of 1.5 MHz have been found to represent the upper limit below which the impact of frequency drift remains neutral.

Cross polarisation effects (**WP3000**) are inevitable when offset parabolic reflectors are deployed in microwave imagers. Such effects can also arise as a result of feed horn manufacturing defects as well as the non-optimal alignment of feed horns. Using a 1D-Var framework this study has shown that cross polarisation errors of 2% result in biases in retrievals of surface winds (10%), total column water vapour (3%) and surface skin temperature (0.06K). A 2% cross polarisation error is judged a reasonable estimate of the magnitude of *uncorrected* cross polarisation errors. In practise this can be reduced through corrections based on pre-launch measurements. Such measurements, carried out to a relative accuracy of 10%, would reduce residual cross polarisation errors to 0.2% and render the consequent biases insignificant.

An investigation into the potential benefit of additional channels in the 15-20 GHz spectral region (**WP4100**) showed that the benefit, in terms of reducing analysis errors for water vapour and cloud

liquid water, drops off monotonically with distance from the water vapour absorption centred on 22.235 GHz. At 15 GHz the error reduction is 25% of that obtained from a channel at 22.235 GHz. This part of the study also showed that for equivalent bandwidths (400 MHz) a channel at 31.4 GHz (with *primary protection*) provides very similar error reductions as a channel at 36.5 GHz (*shared* allocation). A channel at 31.4 GHz is therefore recommended in preference to a channel in the 36-37 GHz region.

The use of digital detection systems for spectrally resolved radiometric measurements in the 50-60 GHz spectral region were explored in **WP4200**. Specifically, this component of the study examined whether there was a strong requirement on the shape of the digital sub-bands. It was shown that numerical apodisation of these sub-bands improves the representation of reconstructed analog bands. This improvement arises through better localisation of the synthesised analog band and becomes increasingly significant as the passband width narrows.

In **W5000** a model was developed for the evaluation of sampling/resolution scenarios. The approach is based on linear estimation theory and uses entropy reduction to quantify the relative merit of various sampling/resolution configurations. Geophysical fields are parametrised to capture the spatial variability of *precipitation-like* events. Initial tests of the scheme show that in the absence of spatially correlated error highly variable fields (such a convective rainfall) favour large beamwidths whereas smooth fields favour small beamwidths, regardless of sampling.

Finally, in **WP6000** data from the latest SSMIS sensor, F18, was assessed. This study is part of an ongoing evaluation of the benefit of co-located sounding chanels in an imaging instrument. Despite the improvements in F-18 SSMIS data through improved pre-launch characterisation of the reflector emissivity a new type of bias has hampered efforts to perform a *like-for-like* comparison of the performance of the SSMIS conical instrument with the established AMSU-A cross track instruments. The new bias is believed to result from radiative forcing of the warm calibration target inadvertantly introduced through design modifications aimed at mitigating indirect solar intrusions into the warm target. In observing system experiments the F18 data was blacklisted in regions affected by this bias (the *descending* node of each orbit) which left data of good quality. Impacts in the southern hemisphere were small, even compared to those achieved from a reduced coverage MetOp-A AMSU-A experiment. In the northern hemisphere the F18 data provided modest positive impact on forecasts, approaching that of a full-coverage MetOp-A experiment.

1 Aim and context of the study

This document describes a EUMETSAT study on the refinement of spectral and radiometric requirements of a post-EPS microwave imaging (MWI) mission. Overall, the study forms part of a larger effort, supported by EUMETSAT and ESA, to define options for the post-EPS microwave sounding (MWS) and imaging missions and to refine the detailed specifications of those missions. More particularly, it aims to support the post-EPS phase-0 and phase-A industrial studies by assessing several potentially important performance characteristics of the MWI mission through a series of observing system experiments (OSEs), 1D-Var analyses and information content (IC) analyses.

The MWI is a cross-purpose, multi-spectral, microwave imager serving operational meteorology and climate applications as defined in the mission requirements document (MRD, 2010). The instrument will be a passive satellite radiometer capable of measuring thermal radiance emitted by the Earth's surface and atmosphere, in discrete channels in the microwave part of the spectrum. The primary objectives of the Post-EPS MWI mission are to provide high quality imagery data for global and regional NWP through the provision of:

- Cloud and precipitation products, including bulk microphysical parameters.
- Water vapour and temperature gross profiles.
- All weather surface imagery including :
  - Sea surface temperature (SST) and ocean salinity,
  - Sea ice coverage,
  - Snow coverage, depth and water equivalent,
  - Soil moisture products,
- Sea surface winds (complementary to the scatterometer).

Microwave imagery data provides a very important constraint on tropospheric humidity over ocean in NWP models as demonstrated in a number of studies in the last decade (Anderson *et al* (2005), Kelly *et al* (2007), Bauer *et al* (2006a,b)). An additional MWI mission objective (MRD, 2010) is to provide continuity for other MWI channels (*e.g.* SSM/I, TMI, AMSR-E and SMOS) in support of long-term climate studies.

Channel positions and geometry requirements for the MWI instrument are reasonably consolidated, however, the detailed radiometric and spectral specifications necessary to meet the user requirements have still to be defined. The user requirements for the MWI are given in the post-EPS position paper for Clouds, Precipitation and Large Scale Land Surface Imaging (*AEG(CPL)*). The relationship between sensor related specifications (*eg* noise, frequency stability and cross-polarisation tolerance) and geophysical analysis/retrieval accuracy is complex. The specification of sensor characteristics therefore requires a multivariate analysis based on a range of approaches, including full OSEs, 1D-Var analyses and information content studies. These tools were used successfully as part of the study *Optimisation of the Oxygen and Water Vapour Sounding Channels Spectral and Radiometric requirements for cross track and conically scanning radiometers* (final report of ESA ESTEC Contract No20711/07/NL/HE, 2008).

Based on the first outputs of the EUMETSAT post-EPS User Consultation process initiated in 2005 (see *AEG(AS), AEG(CPL), AEG(LO)*), ESA and EUMETSAT are in the process of conducting phase-0 studies at instrument and system levels with the support of industry and representatives of the user and

science communities. These studies, aimed at trading-off possible mission concepts which meet the high level user needs previously identified, are planned for completion in 2009.

This study will make use of a range of analysis tools developed as part of recent scientific studies for EUMETSAT and ESA: 4D-Var observing system experiments, 1D-Var studies and Information content analyses. A second important objective is to assess the impact of data from a new SSMIS sensor (F-18), due for launch in July 2009, on NWP analyses and forecasts through OSEs. The findings of this work item will be important in determining the weight given to additional channels in the 50-60 GHz and 183 GHz spectral bands in a MWI mission and will represent the first quantitative evidence of the benefit of these channels in an imaging mission.

The study includes several workpackages as shown below.

- **WP2100 and WP2200.** The primary objective of the two packages is to identify those channels where geophysical parameter analysis/retrieval is most sensitive to *channel frequency shift* and to quantify the sensitivity of analysis and forecast accuracy to frequency shift. This has been established through a combination of radiative transfer studies together with full 4D-Var OSEs. Package **WP2100** is concerned with off-line radiative transfer simulations to provide a parametrization of the errors in brightness temperature (BT) induced by a range of frequency shifts. Package **WP2200** assesses the impact of these shift induced errors on NWP analyses and forecasts using the full 4D-Var assimilation and forecasting system at ECMWF. Observing System Experiments (OSEs) are run using microwave observations which have been perturbed according to the parametrization developed in **WP2100**.

- **WP3100 and WP3200.** This study aims to quantify the sensitivity of geophysical parameter analysis/retrieval to cross-polarisation errors for imager channels. The approach used in **WP3200** involves the use of 1D-Var studies to quantify the impact of residual cross-polarisation errors. In addition, the study will also draw upon the experience gained by US instrument teams engaged in the specification and/or post-launch evaluation of similar imaging missions (including SSM/I, SSMIS, Windsat, TMI and MIS) who's views will be sought in a critical review of the work package results **WP3200**.

- **WP4100.** This workpackage is concerned with the selection of channels in the 15-22, and 31-37 GHz regions of the microwave spectrum given the spectral allocation in these segments of the microwave.

- **WP4200 (ad-hoc study)** The package is concerned with an assessment of NWP user requirements on the shape of digital sub-bands in the 50-60 GHz spectral region used for temperature sounding on both post-EPS MWS and MWI missions and involves the determination of an optimal reconstruction of analog passbands using digital sub-bands.

- **WP5100 and WP5200.** These aim to develop quantitative tools for the evaluation of resolution and sampling scenarios, based on a generalisation of the information content analysis used in previous studies.

- **WP6100 and WP6200.** These workpackages are concerned with an evaluation of data from the latest SSMIS instrument, F-18, through comparison with NWP fields and observing system experiments.

2 The impact of frequency drift (WP2100 and WP2200)

2.1 Outline of Study

Any slow shift in the centre frequencies of MWI pass bands will have the effect of changing the optical depth characteristics of the atmosphere in that pass band. This effect will be largest for pass bands that are on, or close to, sharp absorption lines (*eg* the O_2 absorption lines used for temperature sounding at 50-60 GHz, or the H_2O lines at 22 and 183 GHz). The shift in frequency has the effect of the radiometer sampling higher/lower layers of the atmosphere depending on the nature of the shift. The magnitude of the error (*i.e.* the difference between brightness temperatures (BTs) measured by displaced/undisplaced channel passbands) depends on the form of the temperature profile of the atmosphere in the altitude region around the peak of the weighting function. It can also depend on other quantities such as the surface emissivity for the lower peaking channels and the satellite zenith angle of the observation. The atmospheric water vapour content can also play a role for channels in the 183 GHz spectral region.

To correctly deal with the effect of a frequency shift in an assimilation system, new radiative transfer parametrizations should be carried out at frequent intervals, taking the (known) frequency shift into account, however this is impractical in the context of an operational assimilation system. Within the ECMWF assimilation system the effect of the drifting pass bands will be partly dealt with using variational bias correction (VarBC, see Auligné *et al.*, 2007), but the effectiveness of this form of bias correction for this particular type of error is not clear.

The aim of the first workpackage (**WP2100**) was to define, firstly, a parametrization to be used to describe the form and magnitude of the BT errors and to determine the values for the channel-dependent constants in this parametrization. This was done by simulating the effect on measured BTs of prescribed frequency shifts ($\Delta\nu$) on a wide range of atmospheric profiles representing global atmospheric variability for the AMSU/MHS sounding channels which are assimilated in the ECMWF operational system (channels 4-14 and 18-20), using a line-by-line radiative transfer model.

Secondly, in **WP2200**, OSEs were run, over periods of 90 days, in which realistic systematic perturbations to the observed BTs were added, using the parameterisations derived in WP2100. The impact of this change, using both VarBC corrected as well as uncorrected data, relative to a control experiment is evaluated. Experiments were carried out relative to near full operational configurations to gain realistic estimates of the impact of the frequency shift. The effect of drifting pass bands are most likely to be an issue for the temperature sounding channels where it has been established by earlier studies that relatively small uncorrected errors in measured BTs (of order 0.1K) can adversely effect analyses and forecast quality. The performed OSE experiments are summarised in section 4. Experiment analyses and forecasts were evaluated against operational analyses.

In the remainder of Section 5.1 the background to the post-EPS MWI Mission is described, together with an outline of **WP2000**. In Section 2.2 the line-by-line calculations of the effect of frequency drift are described. Section 2.3 describes the development of the parametrization of these drift induced errors. The set-up and results from the OSEs are described in Section 2.4. Finally, conclusions together with some recommendations for further work are discussed in Section 2.5.

2.2 Radiative transfer study: calculation of the drift in BT

2.2.1 Radiative transfer models

Brightness temperatures are calculated using a line-by-line transmittance model and a radiative transfer (RT) model. The line-by-line model (AMSUTRAN, R. Saunders) is a version of the Millimeter-wave Propagation Model (MPM, Liebe 1989) model developed over several versions by Liebe and others over the last 20 years. It provides atmospheric water vapour and mixed gas (dry air) transmittances on 43 pressure levels (1013.25 to 0.1 hPa). The inputs to the models are channel passbands and atmospheric temperature and water-vapour profiles. The mixed gas profiles are taken from a climatology. Ozone absorption can be added when required (for instance for MHS, mainly to take into account the 183 GHz line), in which case the ozone profile is also from a climatology. The computation of the gaseous absorptions is performed with the Liebe89 model for water vapour, the Liebe93 model (with coefficients from MPM-92) for mixed gases and an adaptation of Liebe 93 using the HITRAN line parameters for ozone. In this study, the frequency resolution of the transmittance computation inside the AMSU channel bands has been adjusted for each channel so that the error in BT is less than 0.001K. Transmittances are then averaged over each channel. Calculations are performed for 6 different atmospheric paths (scan angles). Transmittances are then passed to the RT model (the program is part of an early version of the RTTOV package) which calculates the BT for each of the 6 paths and each specified channel. The surface emissivity is given as an input to the RT model. The spectra of AMSU-A and MHS are shown in Figures 2.1 and 2.2 respectively.

To compute the drift in BT induced by frequency shifts, perturbations in the range $\pm$30MHz have been added to the AMSU channel bands with a frequency step of 1 MHz for AMSU-A and 5 MHz for MHS. The BT calculation was then performed at every frequency shift, for different values of the emissivity and for 52 profiles based on a sampling of the ECMWF model (Chevallier, 2002). These profiles represent the range of variation in temperature and water vapour and were sampled from a large profile dataset generated using the operational suite of the ECMWF forecasting system.

As explained in Section 3, the temperature and water vapour Jacobians and weighting functions are useful quantities for the parametrization of the BT drift. These have been calculated by perturbing the water vapour and temperature at different levels and using the following formulae:

$$H_T = \frac{Tb(T+\frac{\Delta T}{2},q) - Tb(T-\frac{\Delta T}{2},q)}{\Delta T} \; ; \; H_q = \frac{Tb(T,q+\frac{\Delta q}{2}) - Tb(T,q-\frac{\Delta q}{2})}{\Delta q} \tag{1}$$

H_T H_q are Jacobians with respect to temperature (T) and water vapour (q). $Tb(T,q)$ represents the top-of-atmosphere brightness temperature for a given level characterised by temperature and water vapour T and q respectively. ΔT and Δq represent the finite perturbations applied to the temperature and moisture profiles in order to obtain the Jacobians using the central difference approximation. ΔT =1 K and Δq=0.1q. The Jacobians are shown in Figures 2.3 and 2.4 for a surface emissivity of 0.6. They are not normalised by the thickness of each pressure layer and thus depend on the choice of pressure levels. They have been used to help parametrize the drift in BT. However, for the practical implementation in the IFS it is more convenient to replace them by the weighting functions (Figures 2.3 and 2.3, right panels) calculated directly from the total transmittance t:

$$W = \frac{\partial t(z)}{\partial z} \tag{2}$$

Using Jacobians or weighting functions gave similar results in terms of goodness of the fit.

2.2.2 Results for the drift in BT

Table 1 gives the statistics for BT drifts corresponding to a 10 MHz frequency shift for AMSU-A channels 4-14. BT drifts are calculated from the set of 52 atmospheric profiles varying the surface emissivity from 0.6 to 1 and the satellite zenith angle from 0 to 50. The 10 MHz frequency drift is already well above the expected maximum drift of 1.5 MHz (V. Kangas, *pers. comm*). The largest drifts are found for the stratospheric and mesospheric channels (channels 11 to 14), with drifts over 1K for the two highest channels (13 and 14). For the other channels, which peak in the troposphere and stratosphere, the median BT drift remains within ± 0.2 K. Channel 6 is the most affected by the frequency shift, with a median of -0.18 K and standard deviation of nearly 0.1 K. This channel is of particular importance for assimilation in NWP as it is AMSU-A's lowest-peaking channel (400 hPa, Figure 2.3) which provides information about temperature that is not significantly affected by uncertainties in the surface emissivity.

Errors for MHS (2) are typically much smaller for the same frequency drift, especially for channels 4 and 5, with values in the range ± 0.004 K. The BT drift is larger for channel 3 but with most of the values remaining within ± 0.02 K. This is due largely to the symmetric alignment of the MHS passbands with respect to the 183 GHz H_2O absorption line (Figure 2.2, which gives rise to effective compensation for the effect of frequency drift.

The values of the BT drift for AMSU-A/B have to be compared with the model errors mapped into brightness temperatures, which are in the range 0.03-0.1 K for the tropospheric temperature sounding channels. It can therefore be estimated that the errors in the AMSU-A channels are at a level where some measurable negative impact on analyses and forecasts may result. On the contrary, it seems unlikely that drifts of the magnitude of those of MHS would give rise to measurable impacts on analyses or forecasts. Nevertheless, the parametrization of the MHS BT drift has been performed and implemented in the IFS to assess the resulting error in BT when considering the whole range of model profiles.

Figures 2.6-2.12 (the results of the line-by-line model are represented by stars) give an indication of the variation of the BT drift with the frequency shift for AMSU-A. The relationship is fairly linear within the ± 10 MHz range except for channels 9 and 10 (Figures 2.11-2.12). The relationship varies depending on the satellite zenith angle and, for the lower peaking channels (4 and 5), the emissivity. For instance, Figure 2.5 (BT averaged over all atmospheric profile cases) shows that for an emissivity of 1 (right panel), a positive frequency shift in the channel 4 lowers the BT (as it raises the pressure levels to which channel 4 is sensitive to) and that this effect gets stronger with increasing satellite zenith angle. For a surface emissivity of 0.6 (Figure 2.5 left panel), the impact of the satellite zenith angle is stronger than for an emissivity of 1; if the relationship between the frequency shift and BT is fairly similar at high angles, it is of opposite sign at low angles. This is because, for a positive frequency shift, the decrease in BT due

channels	4	5	6	7	8	9	10	11	12	13	14
median	-0.008	-0.106	-0.178	-0.128	-0.087	0.014	0.109	0.291	1.931	1.093	-8.628
std-dev	0.061	0.065	0.092	0.084	0.079	0.032	0.089	0.233	1.444	5.559	4.883
min	-0.184	-0.270	-0.331	-0.270	-0.216	-0.067	-0.071	-0.181	-0.929	-8.181	-22.27
max	0.121	-0.045	-0.019	0.015	0.079	0.097	0.297	0.928	6.376	14.262	0.390

Table 1: Statistics of the drift in BT (in K) induced by a frequency shift of 10 MHz for AMSU-A channels 4 to 14 for the set of 52 atmospheric profiles.

channels	3	4	5
median	-0.0029	-0.0003	0.0000
std-dev	0.0128	0.0010	0.0011
min	-0.0150	-0.0014	-0.0024
max	0.0613	-0.0032	0.0033

Table 2: The same as table 1 but for MHS channels 3 to 5.

to the atmospheric temperature Jacobian peaking higher is compensated by an increase of BT due to the *drifted* channel being less sensitive to surface emissions, while the surface is radiatively colder than the atmosphere. This compensating effect of the emissivity can also be clearly observed for MHS channel 4 and 5, as shown on Figure 2.14 and 2.15 (panel d).

AMSU-A channels 11-14 were not included in the OSEs principally because the parametrization of brightness temperature errors did not perform well for these channels. The decision not to include these channels in subsequent OSEs was supported by several factors:

- The focus of this part of the study was the refinement of the frequency stability specification for the sounding channels of a *MWI mission*, for which it is likely that the temperature sounding channel set will be a *subset* of the existing AMSU-A channel set, covering the troposphere and lower stratosphere only.
- In the case of AMSU-A, channels 11-14 use a phase locked loop oscillator (PLLO) where the local oscillator frequency is actively controlled. The (unlikely) implementation of these channels on a MWI mission would require similar technology and hence frequency stability may be less of a concern here than for those channels using free running local oscillators.

2.3 Parametrization of the drift in brightness temperature

2.3.1 Parameters

In order to simulate the effect of a frequency shift on the AMSU observations to be assimilated in the model, the errors in BT induced by the frequency shift have been parametrized. As explained in the last section, the parametrization has been calculated for AMSU-A channels 4-10 and MHS channels 3-5. It consists in a linear multivariate regression applied to the BT data produced by the RT model. Different parameters have been used for different channels. The physical quantities involved in the parametrization are summarized in Table 3 and explained below. The frequency shift ($\Delta\nu$) to the power 1 and 2 have been used for all AMSU-A channels, channels 6 to 10 also using $\Delta\nu$ to the power 4 . Cross products between the different parameters have also been used. For example, a BT drift which only depends on $\Delta\nu$ (up to a power 2) and the solar zenith angle θ would be given by:

$$\Delta BT(\Delta\nu,\theta) = c_0 + c_1\Delta\nu + c_2\Delta\nu^2 + c_3\theta + c_4\Delta\nu\theta + c_5\Delta\nu^2\theta, \quad (3)$$

where the c_i are the regression coefficients. The list of parameters and their corresponding coefficients for each of the considered channels are given in the appendix A.

AMSU-A		MHS	
channels 4-5	channels 6-10	channel 3	channels 4-5
$\Delta\nu$	$\Delta\nu$	$\Delta\nu$	$\Delta\nu$
cos(zenith angle)	cos(zenith angle)	cos(zenith angle)	cos(zenith angle)
emissivity		emissivity	emissivity
$\overline{\nabla T}^*$	$\overline{\nabla T}^*$	$\overline{\nabla T}^*$	
		WV partial column*	log(WV total column)
			normal factor

Table 3: Physical quantities (explained in the text) used in the parametrization of the drift in BT. The star indicates that the quantity is weight-averaged by the corresponding channel weighting function.

The first two parameters are $\Delta\nu$ and the emissivity (for the lower peaking channels). For the scan angle dependence of the BT drift, the parameter used is the cosine of the satellite zenith angle. To take into account the atmospheric lapse rate, the temperature gradient is another input parameter (∇T). The gradient is calculated with respect to $\log(P)$, where P is the atmospheric pressure (in Figures 2.6-2.13, the plotted temperature gradient is with respect to altitudes) and it is averaged over the layer of atmosphere to which each channel is sensitive to. For this, the temperature gradient at every level is given a weight equal to the value of the weighting function at the same level, as follows:

$$\overline{\nabla T} = \frac{\sum_i \nabla T(z_i) W(z_i)}{\sum_i W(z_i)}. \tag{4}$$

For MHS, the parametrization requires us to calculate the water vapour partial columns q_i defined at each pressure level i as:

$$q_i = r_i \frac{\Delta P_i}{g}, \tag{5}$$

where r_i is the water vapour mass mixing ratio, ΔP_i is the pressure thickness of the layer i and g is the acceleration due to gravity at sea level. For the MHS channel 3, the humidity parameter uses a weighted average of q_i calculated a similar way as in (4).

Other humidity parameters are used for MHS channels 4 and 5. Noting that for these channels the relationship between the BT drift and the logarithm of the total column of water vapour Q can be described by the combination of a linear function and a normal distribution (*e.g.* see Figure 2.14), the parameters used to take into account the dependence on humidity are:

$$Q = \log(\sum_i q_i), \tag{6}$$

$$n = \exp\left(\frac{-(Q-Q_m)^2}{2\sigma^2}\right), \tag{7}$$

where Q_m is equal to 0.7 kg.m^2 and 2.2 kg.m^2, for channels 4 and 5 respectively and σ is equal to 0.6 mm for both channels.

2.3.2 *Validation of the parametrization*

Figures 2.6 to 2.15 show the comparison of BTs obtained with the RT model and with the parametrization for a typical atmospheric case. In general, the parametrized BT agrees well with those from the RT model over a wide range of values of the different parameters. This is true of all of AMSU-A channels 4 to 10 and MHS channels 4 and 5. For those, the goodness of the fit slightly degrades at higher frequency shift, but the errors induced by the parametrization are still small for a shift of ± 30 MHz, which constitutes an extreme value compared to the most plausible shift expected of around 1.5 MHz. MHS channel 3 is the only channel for which the parametrized BT introduces in some cases significant errors compared to the amplitude of the BT drift. One of the main difficulty met in trying to parametrize the BT drift in this channel was the high scatter of the BT drift versus the temperature gradient or the water vapour column parameters.

To get a better idea of the performance of the parametrization over the whole set of atmospheric cases, the coefficient of determination R^2 has been calculated, which indicates the proportion of variance in a data-set that is accounted for by the statistical model.

A value of R^2 of 1.0 indicates that the regression line perfectly fits the data. Results shown in Table 4 confirm the good performances of the parametrization for all the channels with the exception of MHS channel 3. The best performance of the parametrization is found for AMSU-A channel 6, which, as mentioned previously, is expected to have a relatively strong impact on the model analysis and forecast.

	AMSU-A							MHS		
channels	4	5	6	7	8	9	10	3	4	5
R^2	0.93	0.91	0.96	0.92	0.89	0.84	0.75	0.19	0.91	0.91

Table 4: Coefficient of determination R^2 for the parametrization of AMSU-A channels 4 to 10 and MHS channel 3 to 5. This provides information about the goodness of fit of the parametrization.

2.3.3 *Implementation in the IFS*

Following the validation of the scheme, the parametrization of the BT drift has been implemented into the ECMWF forecast and assimilation system. The parametrization is called during the *screening run*, *i.e.* the preliminary quality control of the observations prior to assimilation. At this stage, all the parameters required by the parametrization are available and interpolated at the observation position and time. The model transmittances from which the weighting functions are calculated are given by RTTOV. The atmospheric profiles used are those of the model first-guess. The emissivity is that used in the assimilation. It is calculated with FASTEM2 (Deblonde and English, 2001) over sea and is dynamically retrieved over land (Karbou et al., 2007). The calculated BT drift is then added to the corresponding value of the AMSU observation. As for the case of *unperturbed* observations, departures from the model first-guess are then calculated before undergoing further quality control and finally being assimilated in the system.

The map of the BT drift added to AMSU-A channel 4 observations for a frequency shift of 10 MHz (Figure 2.16) shows the dependence on scan angle, with higher values at nadir. The land-sea contrast in BT corresponds to that in emissivity (Figure 2.17). The values found over land are consistent with those of the weighted-averaged temperature gradient (Figure 2.18). In particular, the low values of the BT drift over Australia correspond to strong negative gradient of temperature (on the graph strongly positive with respect to $\log(P)$) while high BT drift values over North Africa and part of Asia correspond to positive

temperature gradient (negative with respect to $\log(P)$) as expected for night over desert (experiment running for the 00 UT assimilation window).

The range of values of the BT drift found for MHS observations confirm the numbers obtained with the RT study: the majority of the drifts in BT remain far below the error in first-guess temperature. For this reason, the decision has been made to concentrate on running OSE experiments for AMSU-A and to leave MHS observations unperturbed.

2.4 Observation system experiments (OSEs)

2.4.1 Experimental settings

The experiments are carried out for a 3-month period (from 10 September to 10 December 2009) using the 36R1 version of the ECMWF assimilation system with the forecast model running at a resolution of T511 (horizontal resolution approximatively 40 km). As mentioned above, given the small amplitude of the errors introduced in the MHS-like channels and consequently the anticipated lack of measurable impact on moisture analyses and forecasts, only AMSU-A observations for channels 4 to 10 have been considered for the OSE experiments. In order to assess the response of the model to the BT drift, it is crucial to investigate whether VarBC is able to correct for the perturbation added to the AMSU-A observations and how the remaining errors impact the analysis and forecast. The impact of VarBC has then been compared to that of a static bias correction scheme where the bias correction coefficients, first initialised with the corresponding VarBC coefficients from the operational suite, remain constant during all the experiment. Two sets of five experiments each have been run, one using VarBC (VarBC-set) and the other one using the static bias correction (static-set).

The specification of the experiments is as follows:

- For all the experiments, there is a “baseline” database of assimilated observations which consists of the full observing system minus all microwave sounding data.
- Each set of experiments includes a reference experiment, where three AMSU-As in addition of the baseline are assimilated.
- The other four experiments in each set only differ from the reference experiment by the fact that different values of the frequency drifts are added to AMSU-A observations. The four “perturbed” experiments test frequency drifts of respectivelly 1.5, 5, 10 and 20 MHz.

For the calculation of the analysis and forecast scores, perturbed experiments are compared to the corresponding reference experiment.

The three AMSU-A instruments used in the OSEs are on platforms NOAA-15, NOAA-19 and MetOp-A. Channels 11 to 14 are assimilated as in the reference experiments. All the observations undergo the same quality checks as in the operationl suite. Channel 6 from NOAA-15 and channel 7 from MetOp-A, considered to be too noisy, are not assimilated.

2.4.2 Analysis scores

Figure 2.21 shows the mean difference in analysis temperature fields between perturbed AMSU-A experiments and their reference experiments for the 1.5 and 20 MHz drifts. All plots exhibit a systematic

warming over the South Pole throughout the troposphere, going from around 0.05K for the 1.5 MHz shift experiment using VarBC to up to 1 K for the 20 MHz shift experiment using the static bias correction. Elsewhere, the differences appear mostly small scale and random for the 1.5 MHz shift experiment using VarBC. For the other experiments, cooling/warming patterns alternating with height appear over the North Pole. In addition, the experiments that use the static bias correction show a clear cooling of around 100 hPa in the tropics.

Figure 2.22 shows the zonal mean errors in the temperature analysis for the same experiments as in Figure. 2.21 and the reference experiments. They are calculated taking the full resolution (T799, around 25 km resolution) ECMWF operational analysis as a proxy for truth. These errors are thus underestimated, as the operational analysis also has non-zero errors. Comparing the perturbed AMSU-A experiments with their reference experiments, larger errors are found for the experiment with the 20 MHz frequency shift using the static bias correction. The error increase in temperature analysis is particularly dramatic over high latitudes, with maximum values of 1 K around 80°S at 700 hPa. Over the tropics and mid-latitudes, the analysis error increases are between 0.05 and 0.1 K in the upper troposphere and typically less than 0.1 K in the lower troposphere. Although these errors are large, Figure 2.22 shows that most of them are actually corrected by VarBC. The errors for the 20 MHz shift experiment using VarBC are still detectable, but remain less than 0.02 K over most of the tropics and mid-latitudes and increase above high latitudes. The error increase is higher at the South Pole with a maximum of 0.5 K around 80°. Errors in temperature analysis of the two 1.5 MHz experiments are both very close to their reference experiment.

2.4.3 Forecast scores

The forecast scores are calculated as the normalised difference in root mean square errors between each perturbed AMSU-A forecast experiment and the corresponding reference forecast experiment, such that a positive score indicates a degradation of the forecast. Experiments are verified against the operational analysis. Figures 2.23 and 2.24 show the temperature and geopotential forecast scores for the VarBC-set. The scores strongly degrade with increasing frequency shift. Temperature RMS forecast scores in the tropics at 500 hPa, however, are dominated by small persistent biases in the large scale temperature fields due to forecast model biases. In principle the introduction of a biased radiance observation into the analysis which happens to be in better agreement with the biased model state will give *better* forecast scores than an experiment which assimilates unbiased data. This is likely to be the cause of the apparent improvement in scores for the experiments in which a finite drift has been added. Results can be summarized as follow:

- For the shift of 20 MHz (blue line), the negative impact of the 20 MHz frequency shift is obvious all over the troposphere, with the worst impact found in the Southern Hemisphere (poorer in conventional data hence more dependent on satellite data) where a degradation of the scores is around 10% at forecast day 1.

- For the 10 MHz shift (green line), the negative impact of the frequency shift is smaller, yet very clear, with a persistent degradation of the forecast over the Southern Hemisphere and in the upper troposphere.

- For the 5 MHz frequency shift (red line), a small negative impact at forecast day-1 is measurable but the impact is neutral at other forecast steps.

- The general impact of the 1.5 MHz frequency shift is neutral for both the temperature and geopotential scores.

This suggests that, with the use of VarBC, the upper limit for a frequency drift which does not affect the forecast is around 1.5 MHz.

Figures 2.25 and 2.26 show the temperature and geopotential forecast scores for the static-set. Note the difference of scales on the y-axis compared to 2.23 and 2.24. The impact of the 20 MHz shift is much worst than when VarBC is used, especially in the upper troposphere. with values twice larger than those in 2.23 and Figures 2.24 at 500 hPa and more than 3 times larger at 200 hPa. The 10 MHz shift experiment scores are on average worse for the static-set than for the VarBC-set up to forecast day 2 to 3. These results are consistent with those found with the analysis as they confirm the ability of VarBC to correct for part of the errors added to the AMSU-A observations.

In order to better evaluate the impact of the correction scheme for the lowest frequency shifts, the temperature scores of the two sets of experiments are shown on the same plots (Figure 2.27) for the 5 and 1.5 MHz shift. The values of the forecast scores are small (less than 2%) for all the experiments shown. For the 5 MHz shift, there is a slight but significant negative impact at day 1 in the SH. On average over the globe, the scores for the 5 MHz shift are worst for the static-set (blue line) than for the VarBC-set (red line) at 200 hPa, but also in the SH and tropics at 1000 hPa. Elsewhere, the two experiments have mostly similar scores.

The 1.5 MHz frequency shift with the static bias correction mostly leads to a neutral impact on the forecast scores as for the VarBC-set. There are nonetheless a small number of significantly positive values but also few significantly negative values, which suggest that these values may be produced by noise. It is thus reasonable to assume that overall, the impact on the scores for the 1.5 MHz shift experiment from the static-set is neutral. These results are consistent with the forecast scores for the geopotential height.

2.4.4 Note on the orbital dependency of the drift

An important motivation for the development of the parametrization was the capability to model orbitally dependent drifts, for example of the type caused by thermal cycling of the instrument around an orbit. Preliminary estimates of the magnitude of this type of frequency drift error were obtained based on pre-launch test data for NOAA-15 AMSU-A (N. Atkinson, *pers. comm.*) which included an assessment of the temperature tuning coefficient of the local oscillators. This, together with on-orbit measurements of the local oscillator temperature, enabled us to estimate the frequency drift, and hence the brightness temperature errors, for AMSU-A channels 4-8.

For a range of atmospheric profiles, the frequency drift associated with the maximum temperature variation of the local oscillator is around ± 0.05 MHz, which corresponds to errors in BT in the range ± 0.0015 K. The magnitude of this frequency drift is much lower than the 1.5 MHz frequency shift which, as discussed in the previous section, does not have a significant impact on the forecast. Even in the case where the relationship between the local oscillator temperature and the frequency shift would be underestimated by a factor of 10 (as is suspected, N.Atkinson *pers. comm.*), the resulting frequency would still be below the value of 1.5 MHz. It can then be anticipated that orbitally dependent drifts would not affect the forecast.

2.5 Conclusions and further work

A line-by-line radiative transfer modelling study has been carried out to assess the errors in measured brightness temperatures arising from drifts in the passband centre frequencies for AMSU-A channels 4-14 and for MHS/MHS channels 3-5. Frequency shifts in the range $\pm$30 MHz were simulated. For AMSU-A channels 4-10 (median) errors were in the range $\pm$0.2 K for frequency shifts of 10 MHz. These errors are similar in magnitude to the errors in model fields, projected into radiance space, and are expected to result in measurable negative impacts in forecast quality. For AMSU-A channels 11-14 simulated errors were larger; however, these channels are unlikely to feature in a microwave imaging mission and were not included in subsequent OSEs.

For MHS (median) errors are below 0.003 K for a frequency shift of 10 MHz. This weak sensitivity arises from the symmetric alignment of the bands with respect to the absorption line centre position which gives rise to an effective cancellation of the shift induced errors. Given that model errors in humidity, mapped to radiance space, are in the range 1-2 K for these channels it is unlikely that errors of 0.003K would result in a measurable degradation in forecast quality and hence OSEs were not run for MHS.

Observing System Experiments were conducted for scenarios which assumed shifts ranging from 1.5 to 20 MHz for a constellation of three AMSU-A instruments. For both these scenarios variational bias correction was activated and deactivated to assess the effectiveness of variational bias correction in compensating for this type of bias.

For 3-month OSEs, a very significant negative impact on analyses was detectable for the 20 MHz shift experiments. Errors in temperature at 500 hPa in the northern midlatitudes, for example, are increased from 0.25 K to 0.3 K with VarBC deactivated. In the southern mid-latitudes errors are increased from 0.3 K to 0.4 K. The error increase is larger still for the southern polar regions where the analysis error is increased from 0.2 K to 0.7 K. The activation of VarBC is effective in significantly reducing the magnitude of these analysis errors but the residual analysis errors remain above those for the reference experiment in most regions. On the other hand, for the shift of 1.5 MHz, the errors are reduced at a level close to those of the reference experiments.

The forecast impacts are broadly consistent with the impacts on analyses. For example, for the 20 MHz shift experiments, RMS errors in 500 hPa geopotential forecasts at T+24 hours are doubled in both (extra-tropical) hemispheres relative to a shift-free reference experiment when VarBC is deactivated. These errors are greatly reduced, but still remain significant at 3-4% , when VarBC is activated. Forecast scores for experiments testing intermediate shifts (5 and 10 MHz) show that frequency shifts equal or greater than 5 MHz give rise to measurable degradation of the forecast even when VarBC is used, also VarBC still corrects a large part of the errors. For the 1.5 MHz frequency shift, the impact has been found to be neutral for both experiments using VarBC and using the static bias correction. Hence, the value of 1.5 MHz can be seen as an upper limit below which frequency shifts do not degrade forecasts in assimilation systems with static or variational bias correction schemes. The use of a variational bias correction scheme such as VarBC still appears safer for larger frequency shifts, as it helps reduce their impact.

A motivation for the development of the parametrization scheme was to enable the simulation of orbitally dependent frequency drifts, for example drifts induced by the thermal cycling of the instrument over the course of an orbit. Preliminary calculations, based on local oscillator temperature tuning coefficients from the pre-launch testing of AMSU-A, indicate that such effects would most likely give rise to small frequency shift (less than 0.5 MHz), corresponding to small errors in brightness temperature (less than 0.015 K), which should not affect the forecast.

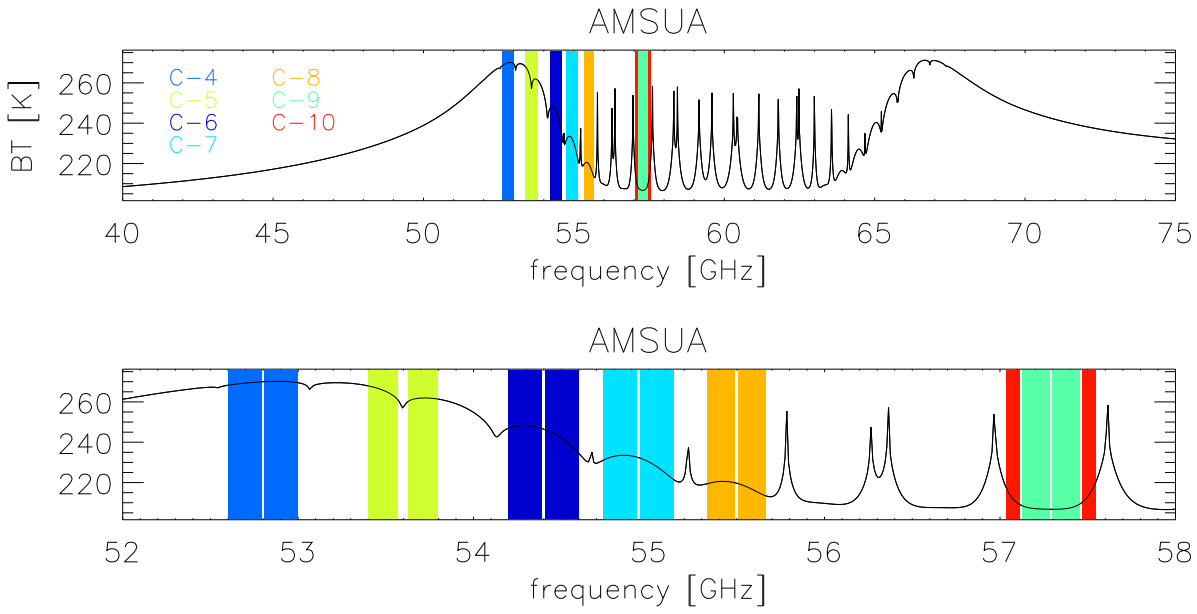

Figure 2.1: Brightness temperature calculated with the off-line radiative transfer model from typical tropical temperature and water-vapour profiles. The channels shown are those used in the parametrization study.

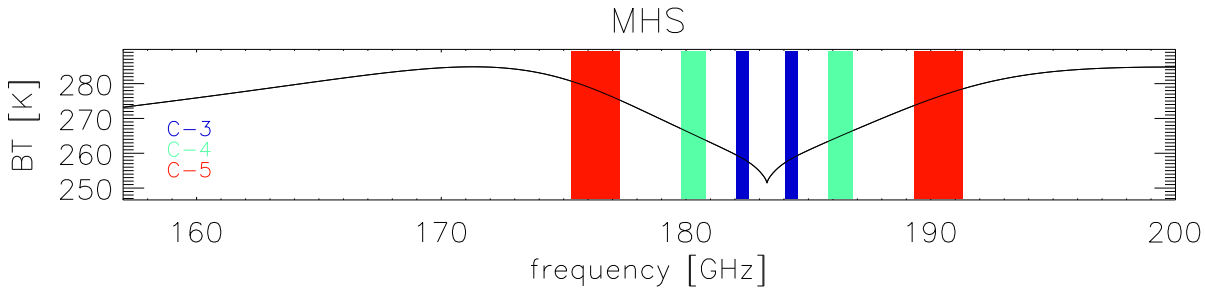

Figure 2.2: The same as in Figure 2.1.

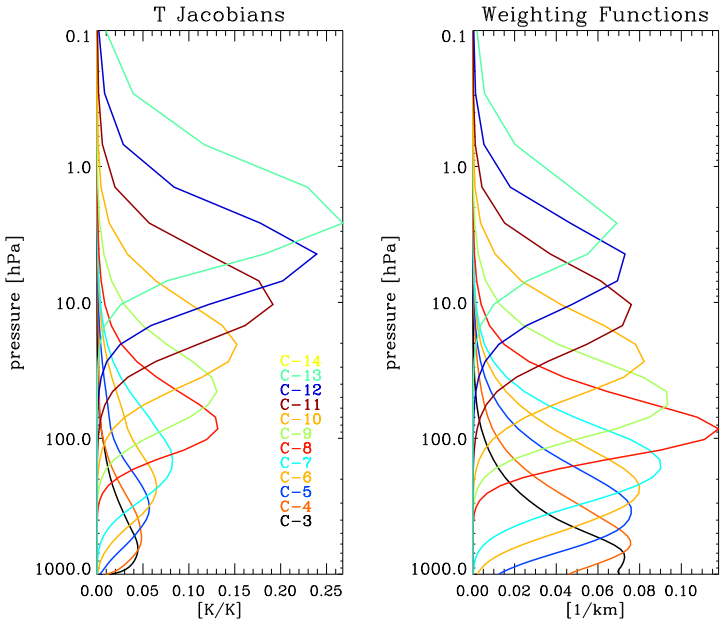

Figure 2.3: AMSU-A channels 4 to 14 (a) temperature Jacobians and (b) weighting functions calculated from typical tropical profiles.

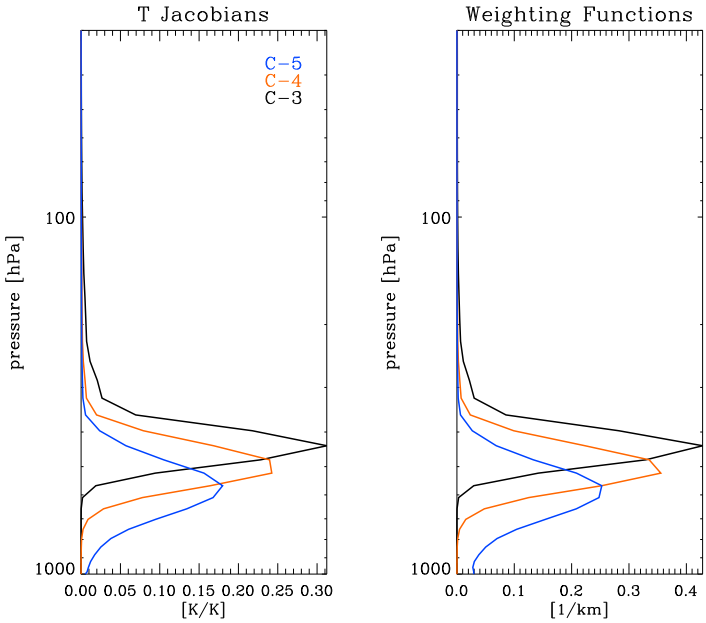

Figure 2.4: The same as in Figure 2.3 for MHS channels 3 to 5.

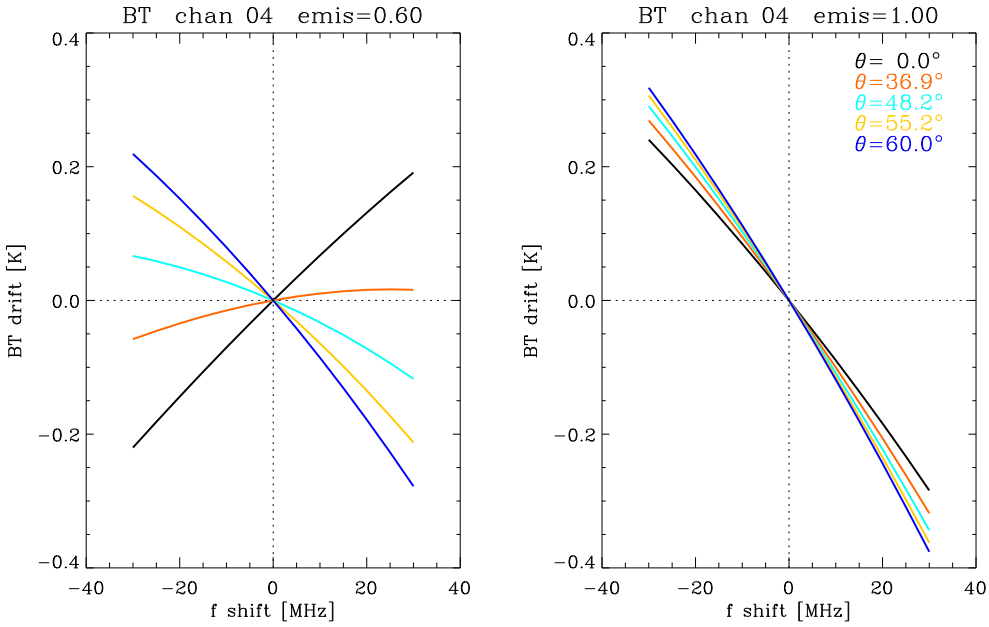

Figure 2.5: The BT drift in AMSU-A channel 4 versus frequency shift for an emissivity of 0.6 (left panel) and 0.96 (right panel) and for 5 values of the satellite zenith angle. The BT drift is the mean over the sample of BT drifts obtained from the 52 atmospheric profiles.

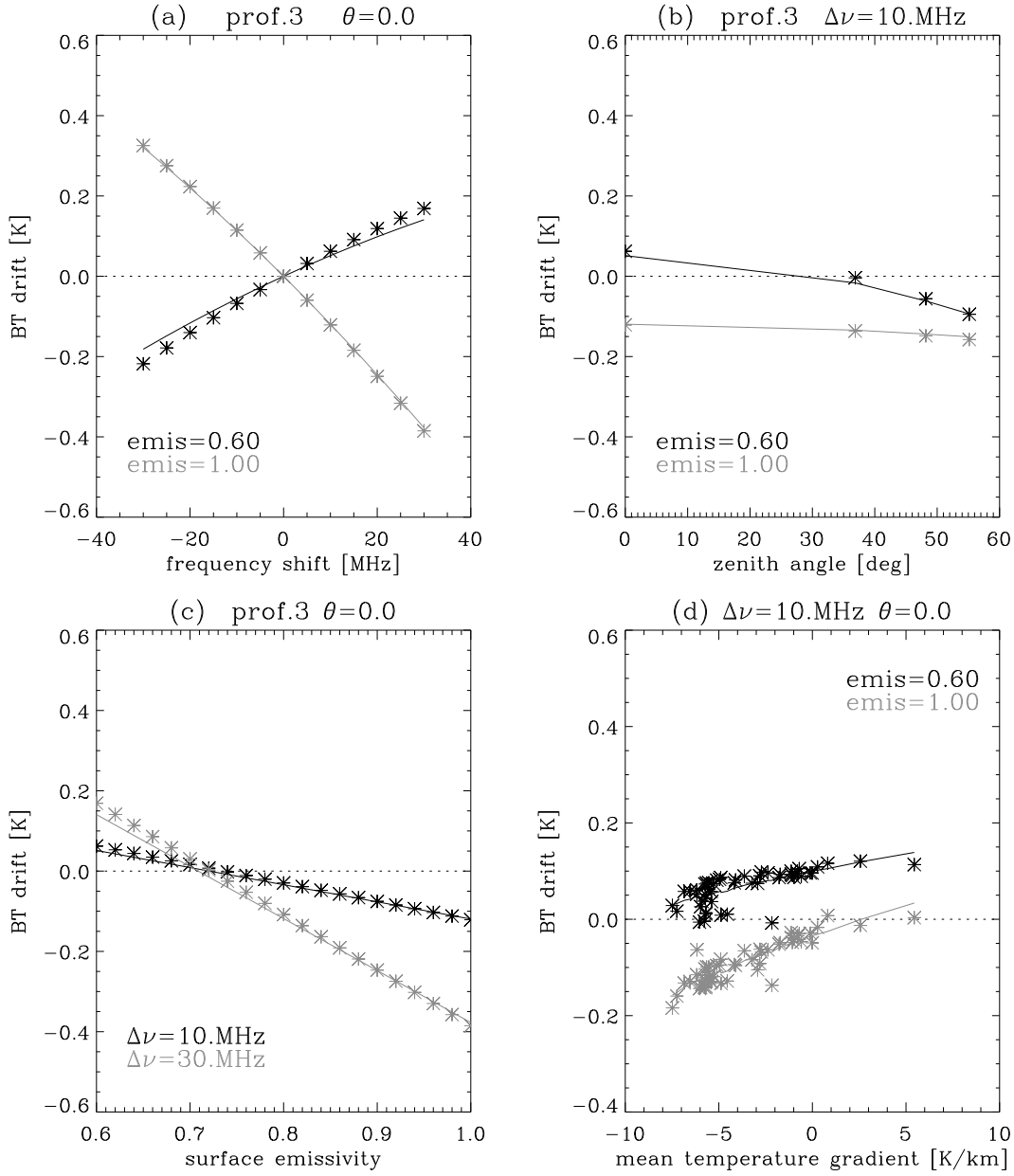

Figure 2.6: The BT drift in AMSU-A channel 4 vs frequency shift (a), satellite zenith angle (b), surface emissivity (c) and weighted-average temperature gradient (d), for discrete realisation of these parameters obtained using a line-by-line RT model (stars) and the new parametrization (line). Panels a, b and c correspond to a given profile of the database, indicated as a red star in the panel d. fig

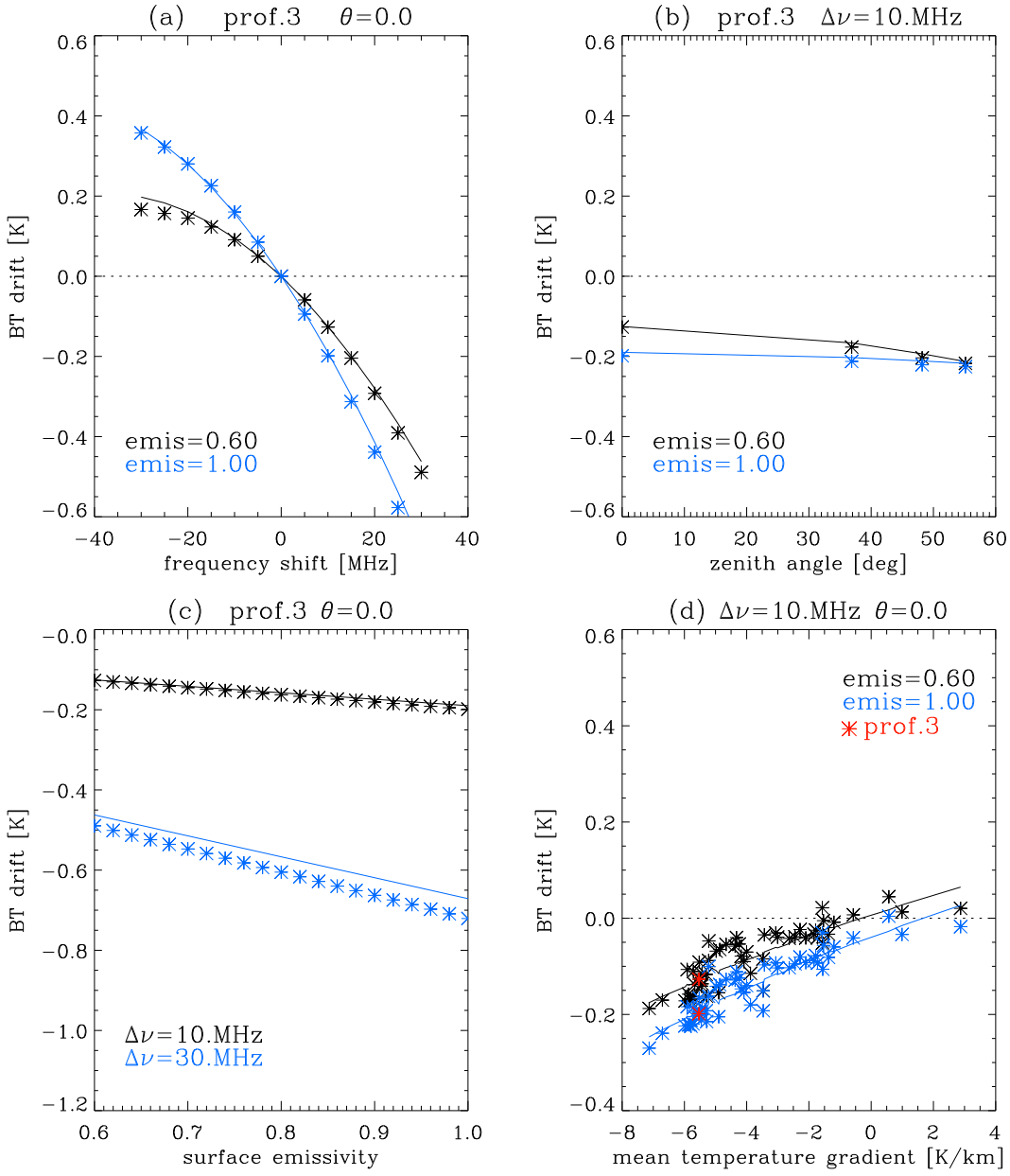

Figure 2.7: The same as Figure 2.6 but for AMSU-A channel 5

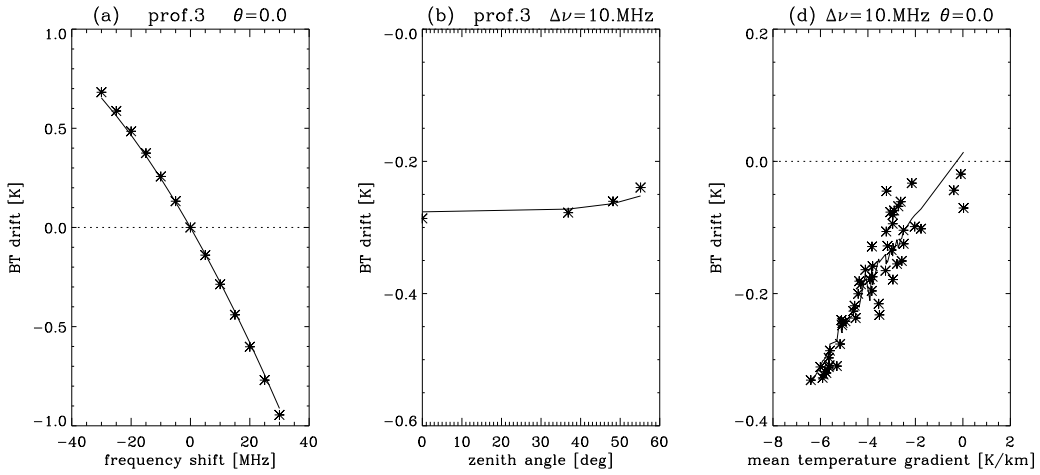

Figure 2.8: The BT drift in AMSU-A channel 6 vs frequency shift (a), satellite zenith angle (b) and weigh-average temperature gradient (d), for discrete realisation of these parameters obtained using a line-by-line RT model (stars) and the new parametrization (line).

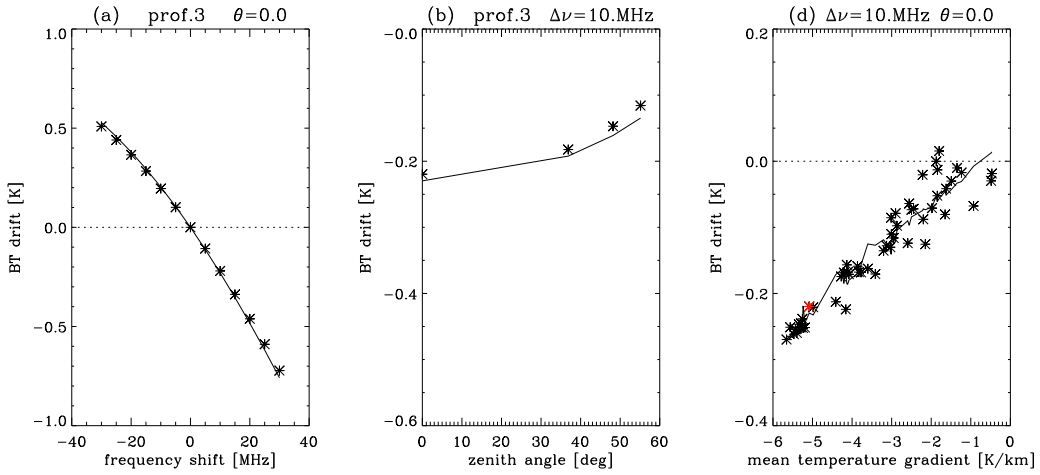

Figure 2.9: The same as Figure 2.8 but for AMSU-A channel 7.

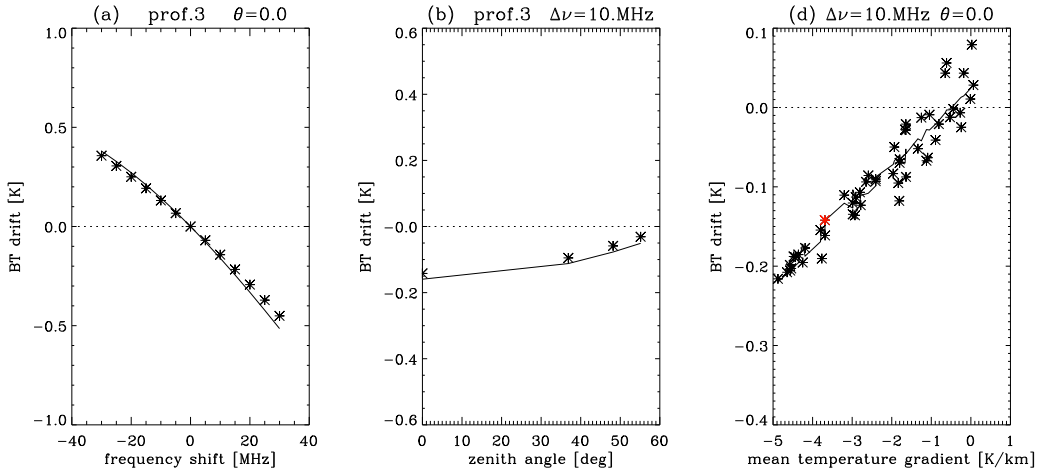

Figure 2.10: The same as Figure 2.8 but for AMSU-A channel 8.

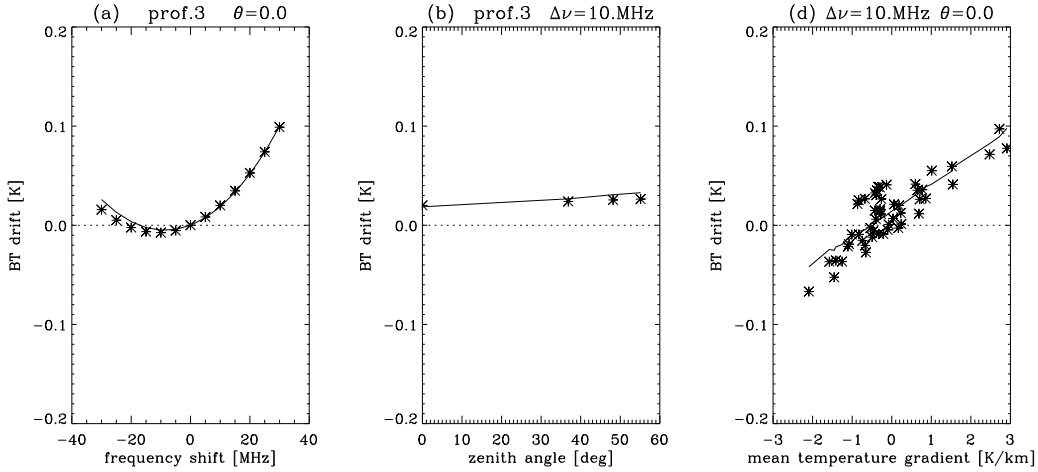

Figure 2.11: The same as Figure 2.8 but for AMSU-A channel 9.

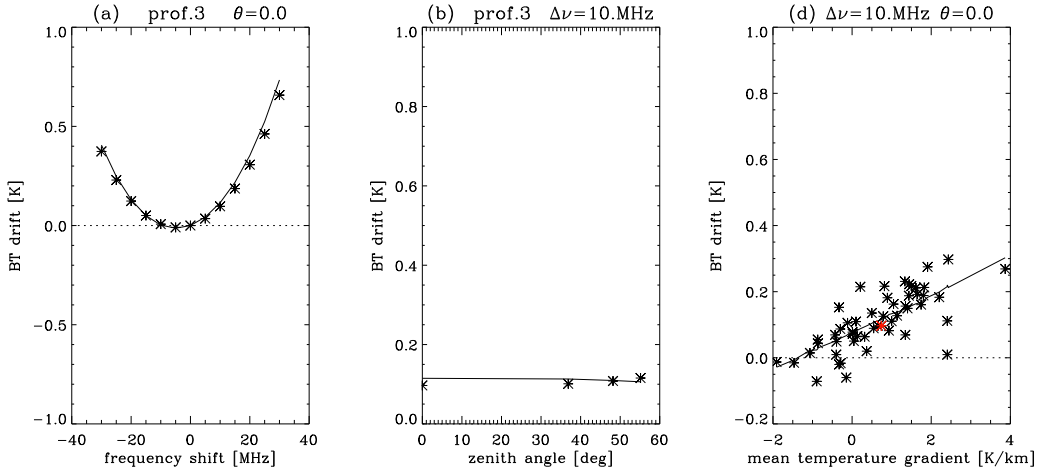

Figure 2.12: The same as Figure 2.8 but for AMSU-A channel 10.

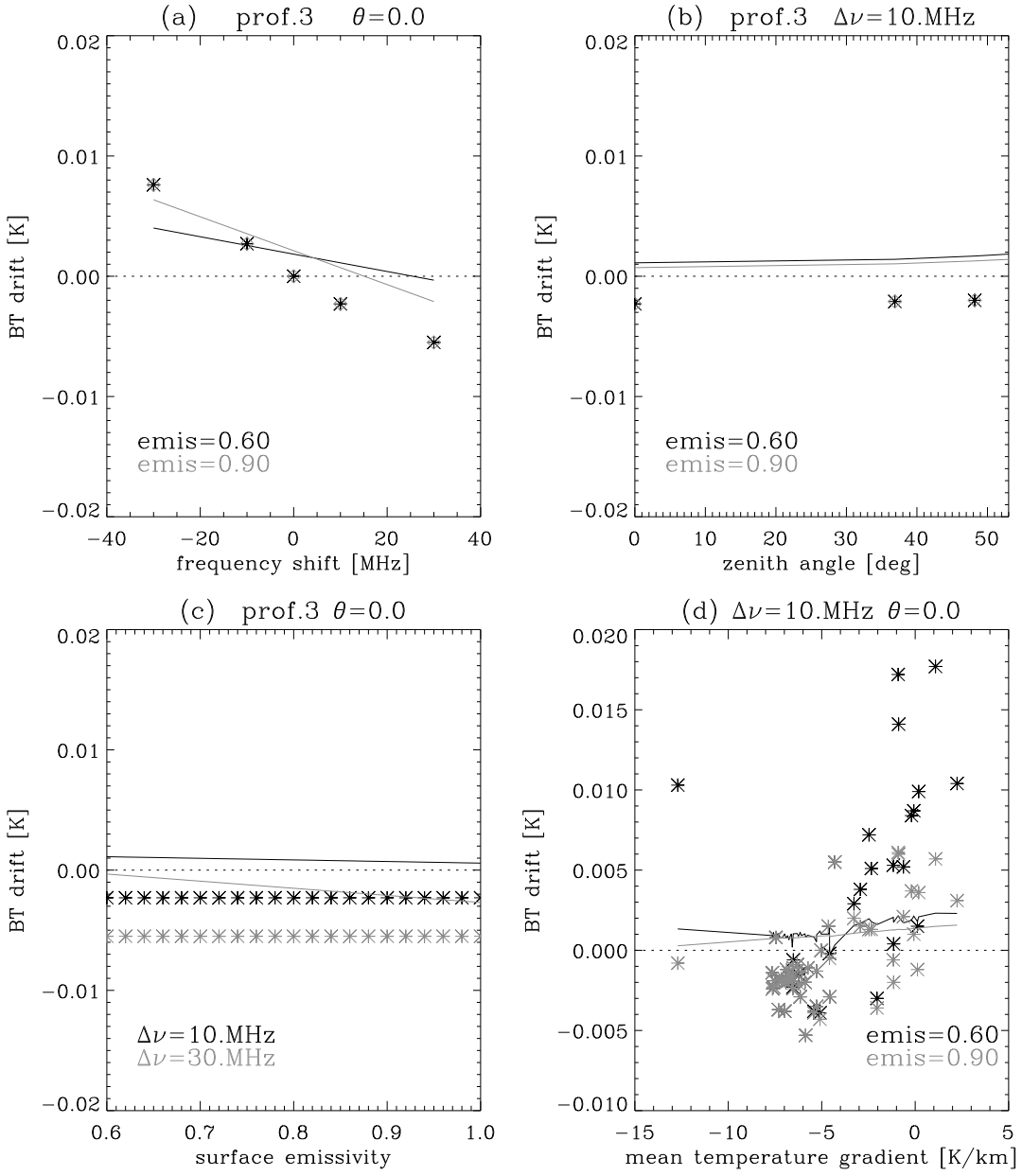

Figure 2.13: The same as Fig. 2.6 but for MHS channel 3.

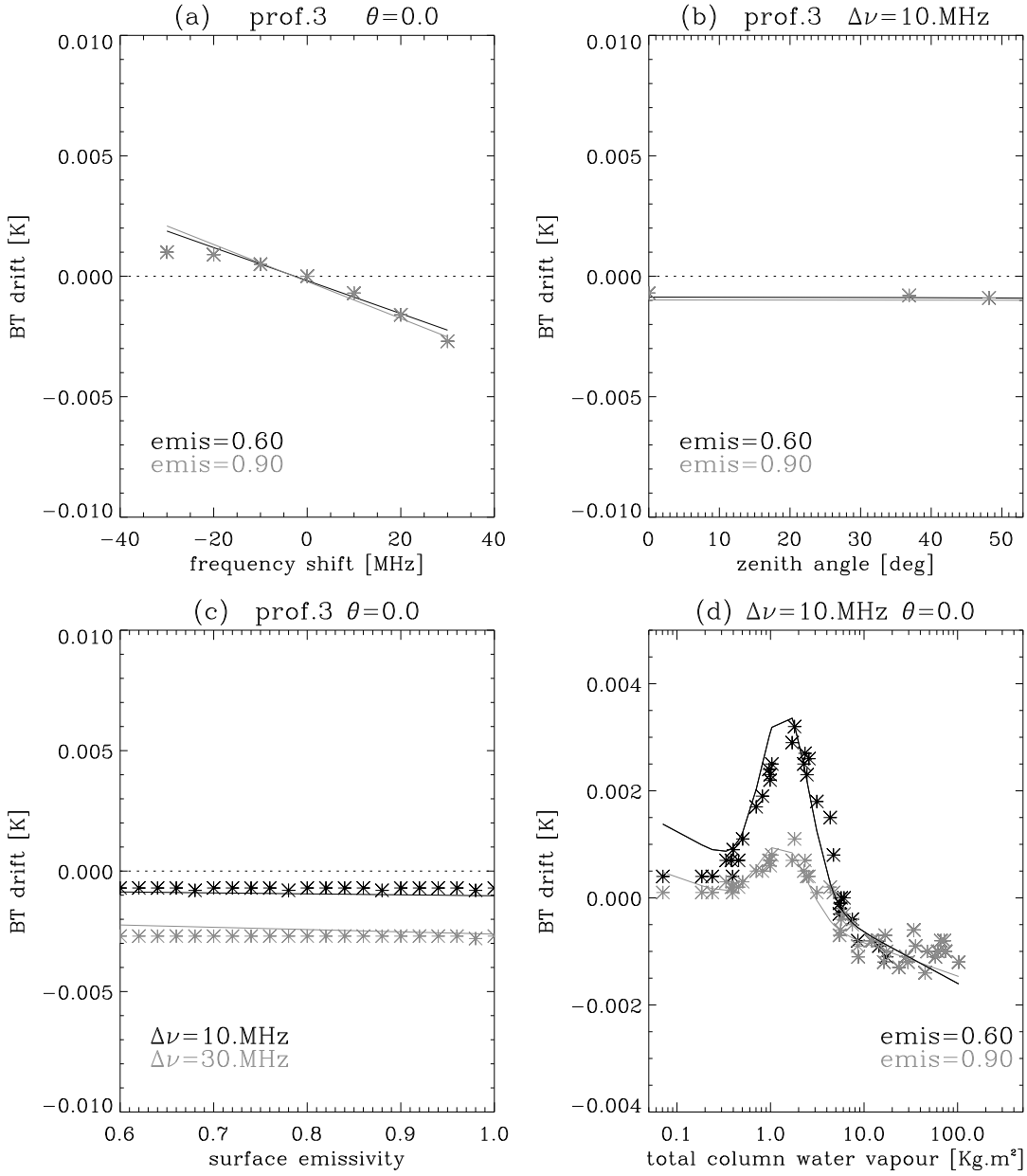

Figure 2.14: The BT drift in MHS channel 4 vs frequency shift (a), satellite zenith angle (b), surface emissivity (c) and total column water vapour (d), for discrete realisation of these parameters obtained using a line-by-line RT model (stars) and the new parametrisation (line). Panels a, b and c correspond to a given profile of the database, indicated as a red star in the panel d.

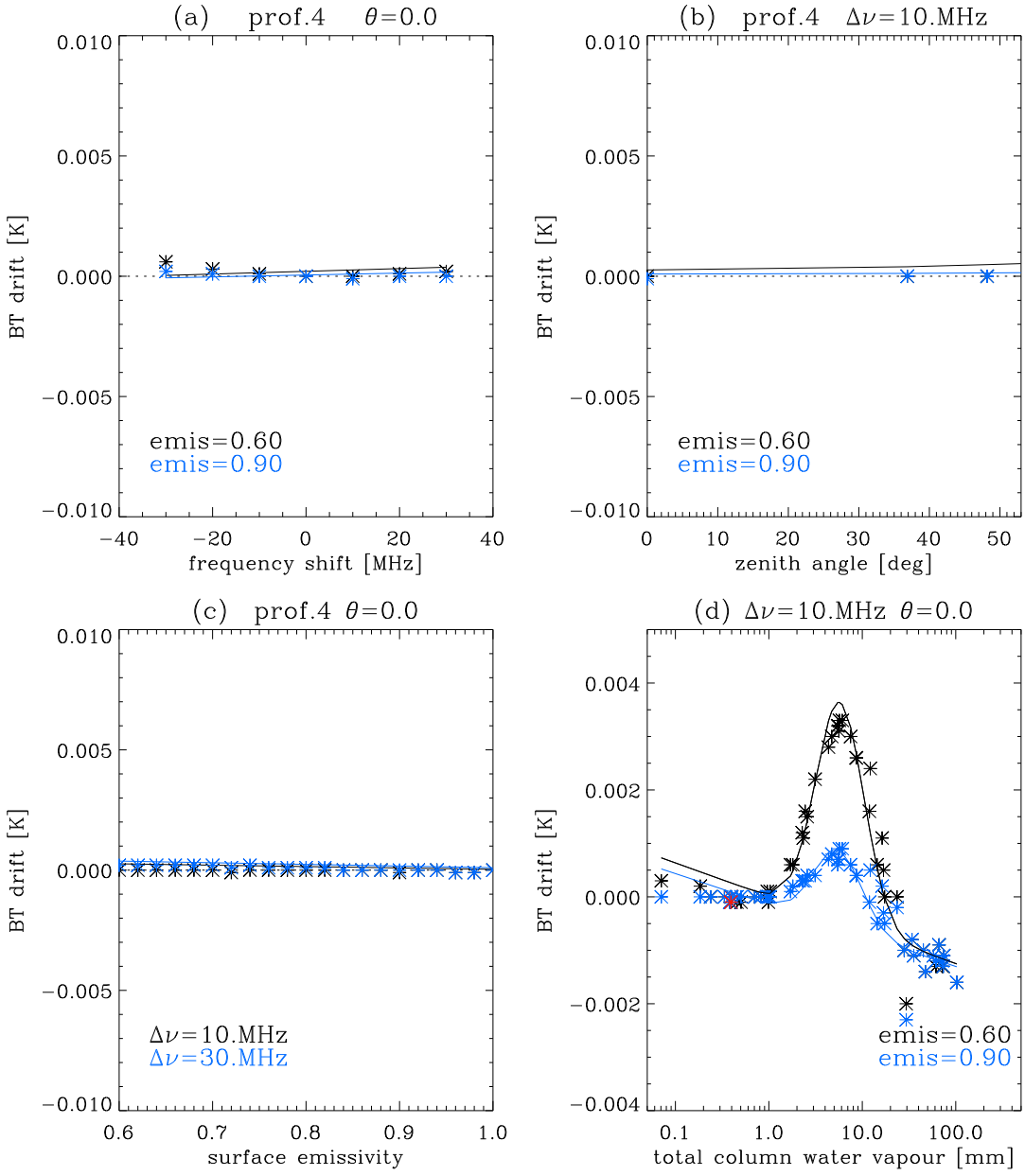

Figure 2.15: The same as Figure 2.14 but for MHS channel 5.

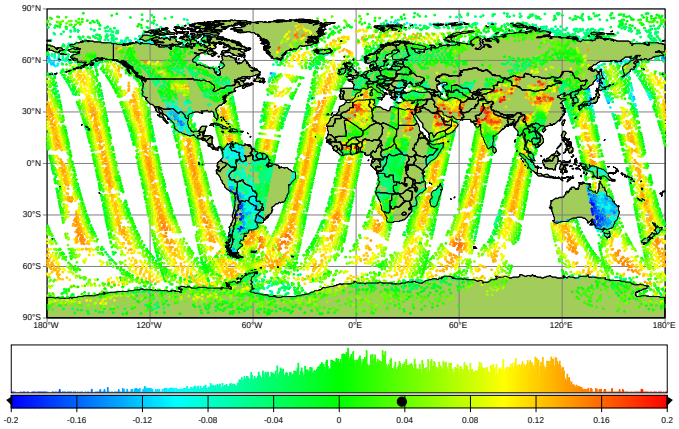

Figure 2.16: Distribution of computed errors in brightness temperature (in K) for NOAA-15 AMSU-A channel 4 for a single assimilation cycle on 17 January 2010 (00 UT assimilation window) assuming a fixed frequency drift for this channel of 10MHz.

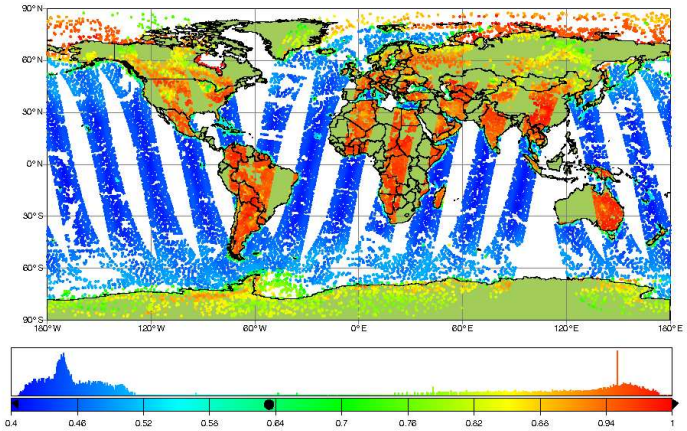

Figure 2.17: Distribution of the model surface emissivity (AMSU-A channel 4) for a single assimilation cycle on 17 January 2010.

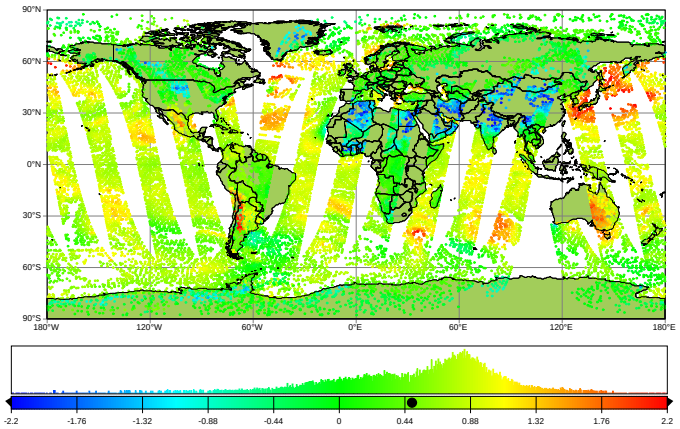

Figure 2.18: Distribution of the temperature gradient with respect to the logarithm of the pressure for a single assimilation cycle on 17 January 2010.

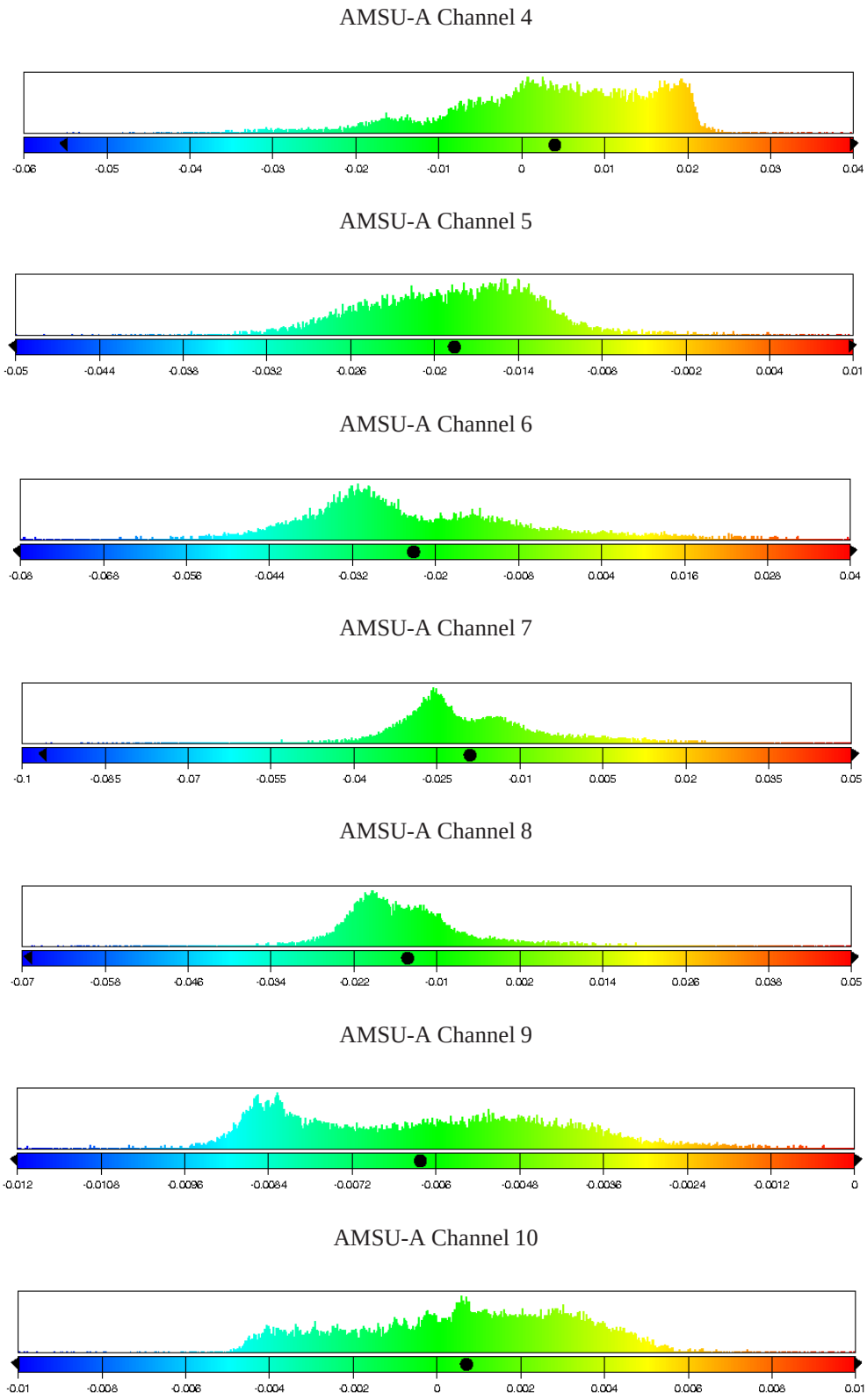

Figure 2.19: Histograms of computed errors in brightness temperature (in K) for AMSU-A channel 4 to 10 for a single assimilation cycle on 17 January 2010 assuming a fixed frequency drift of 1.5MHz.

AMSU-A Channel 4

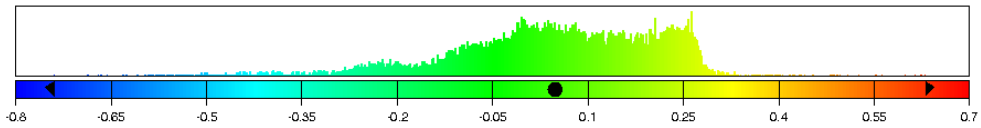

AMSU-A Channel 5

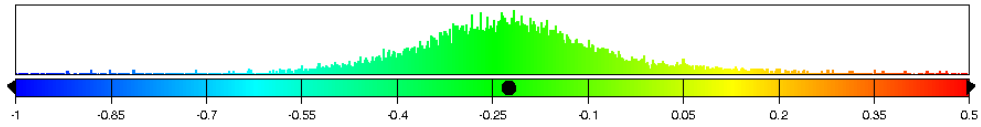

AMSU-A Channel 6

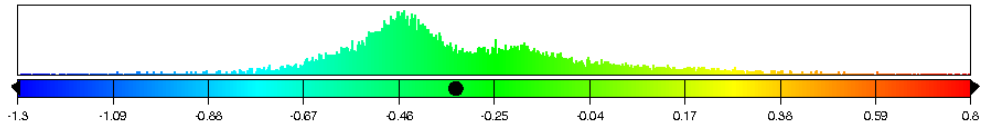

AMSU-A Channel 7

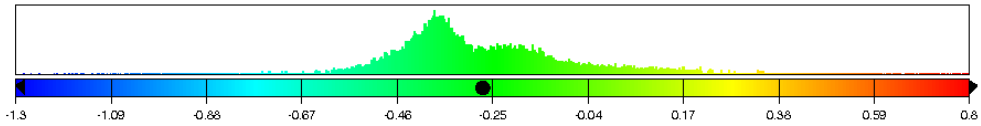

AMSU-A Channel 8

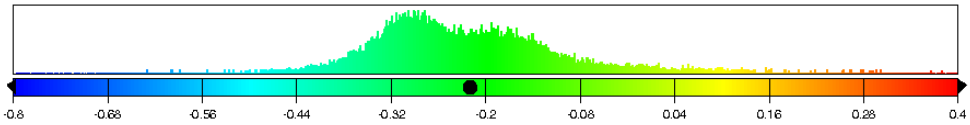

AMSU-A Channel 9

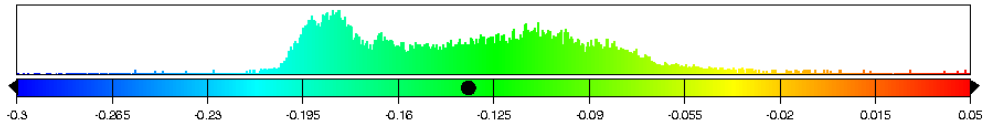

AMSU-A Channel 10

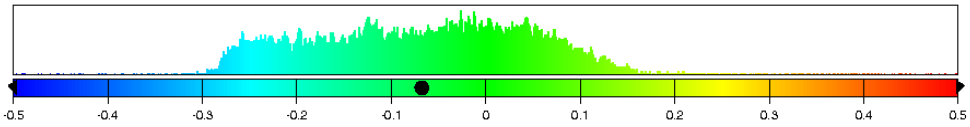

Figure 2.20: The same as for Fig 2.19 but assuming a fixed frequency drift of 20MHz.

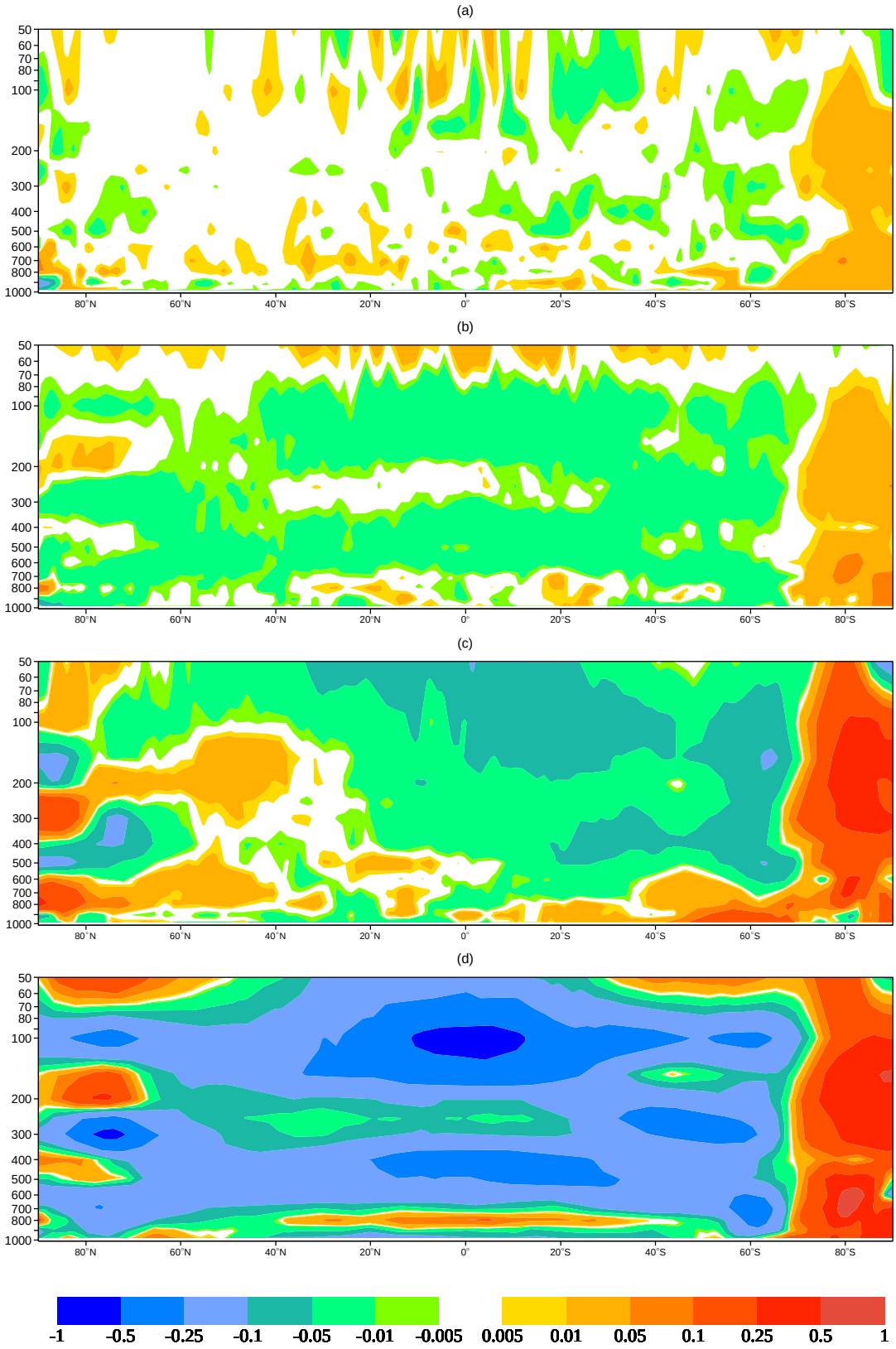

Figure 2.21: Zonal mean differences in K (perturbed AMSU-A experiments minus the reference experiment) in analysis temperature fields averaged over 30 days, for the 1.5 MHz shift experiments using VarBC (a) and using the static bias correction (b) and the 20 MHz shift experiments using VarBC (c) and using the static bias correction (d).

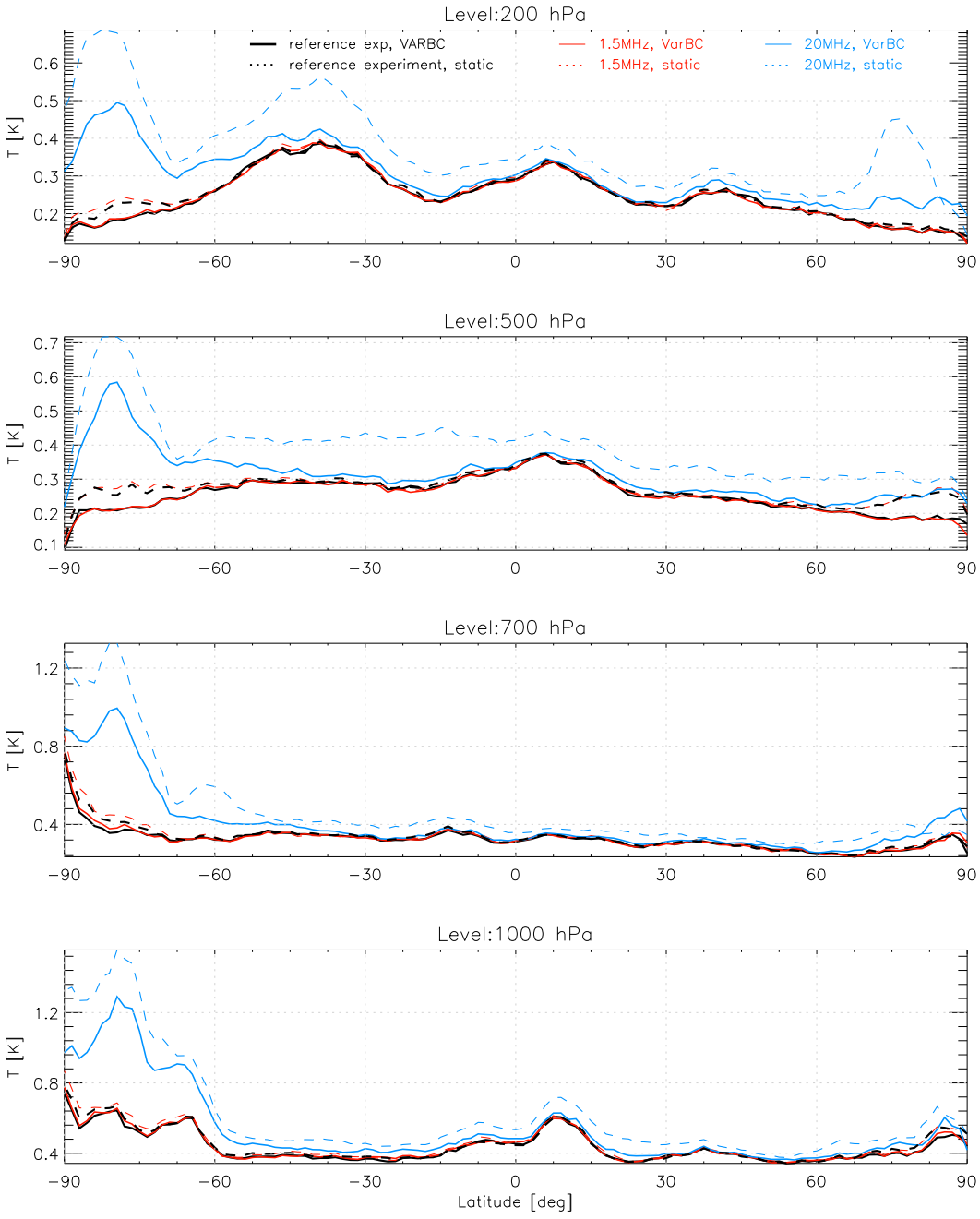

Figure 2.22: Zonal mean errors (latitude vs pressure) in temperature analysis over the 30-day period starting 12 September 2009, for experiments using VarBC (solid line) and using the static bias correction (dashed line) and for the frequency shift of 1.5 MHz (red) and 20 MHz (blue).

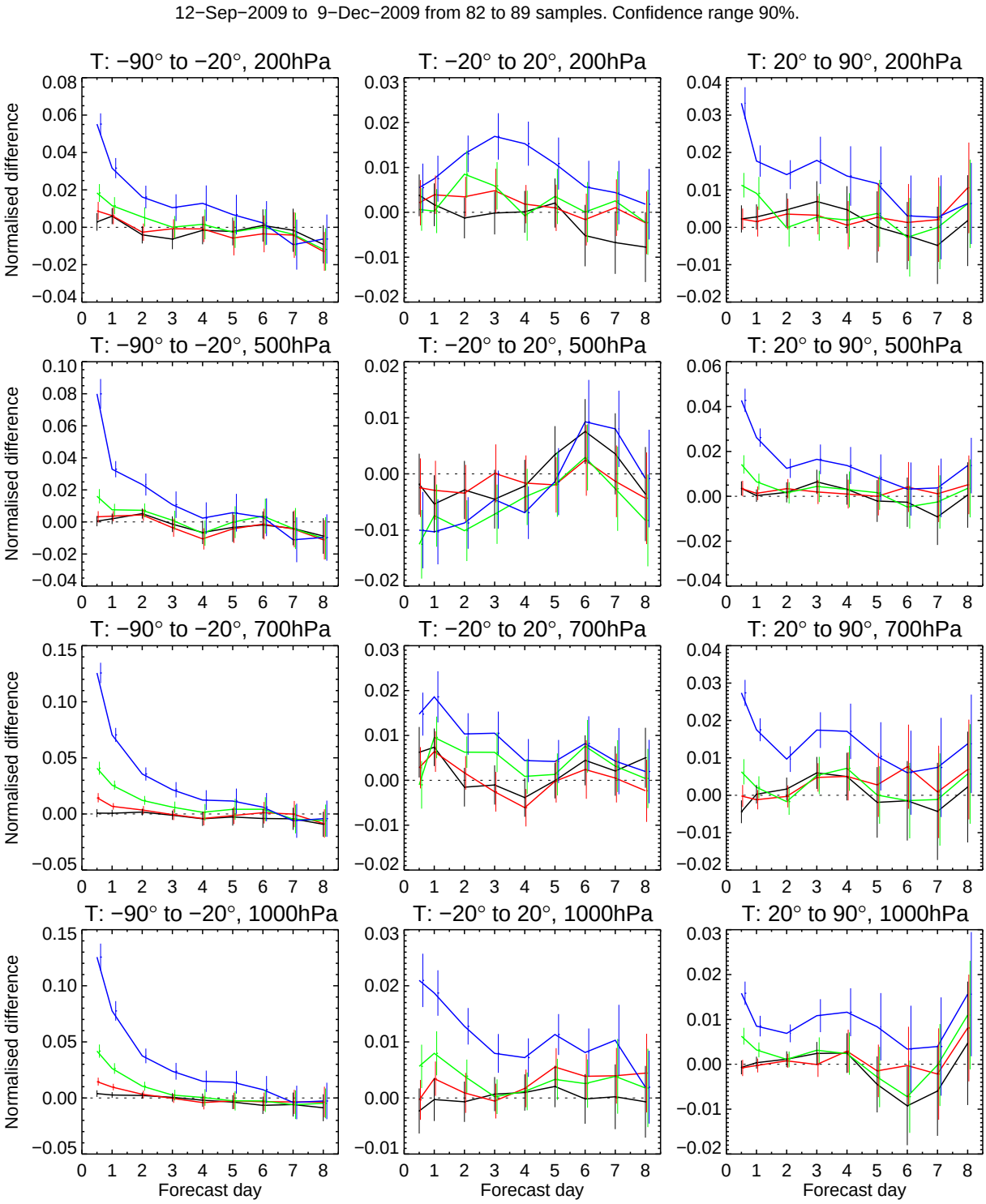

Figure 2.23: Normalized root-mean-square forecast error difference in temperature between experiments with perturbed AMSU-A observations and their reference experiment (see text) verified against the operational analyses for the set of experiments using VARBC. Different colours correspond to different frequency shifts: 1.5 MHz (black), 5 MHz (red), 10 MHz (green), 20 MHz (blue).

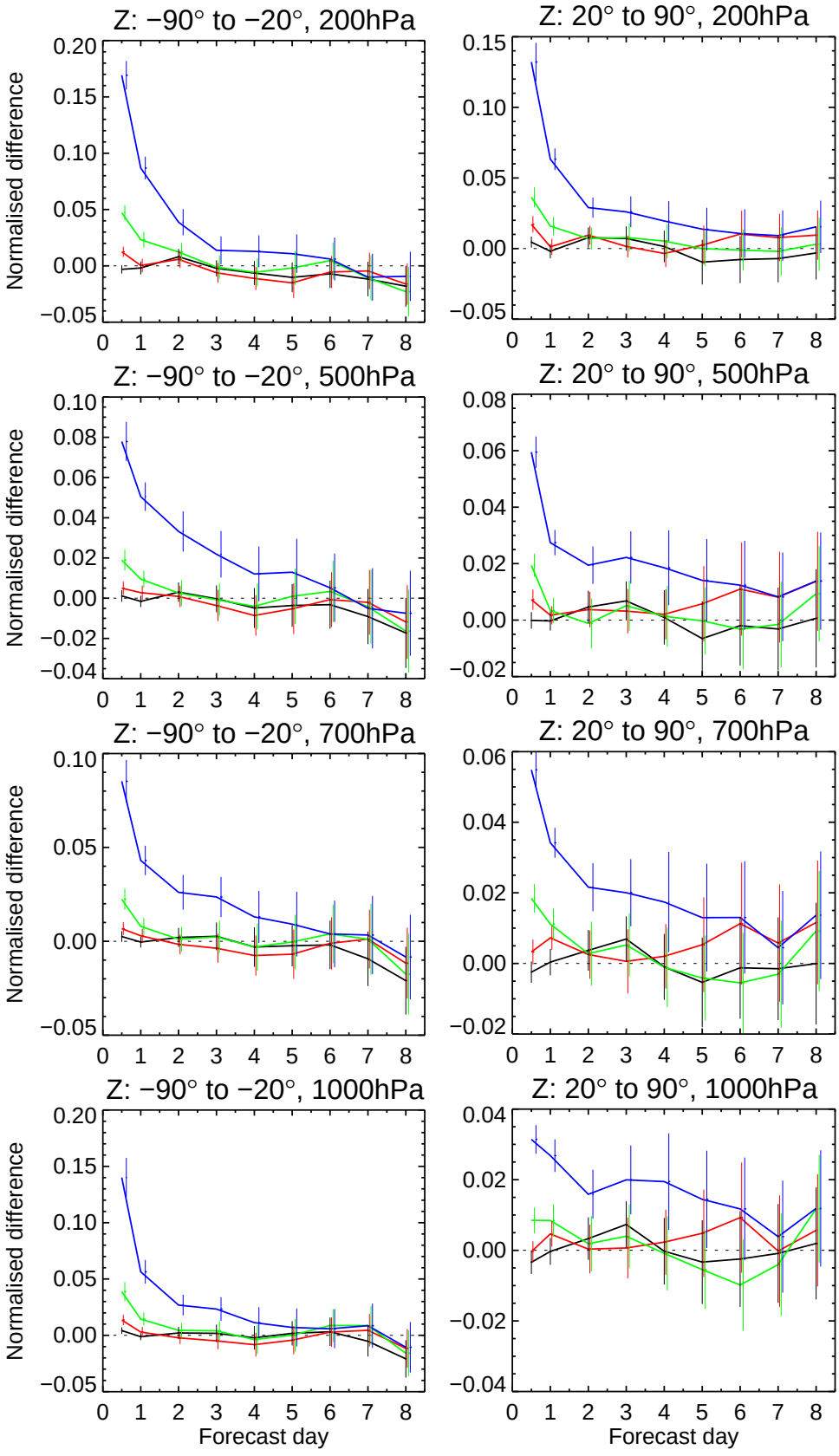

Figure 2.24: The same as Figure 2.23 but for the geopotential height.

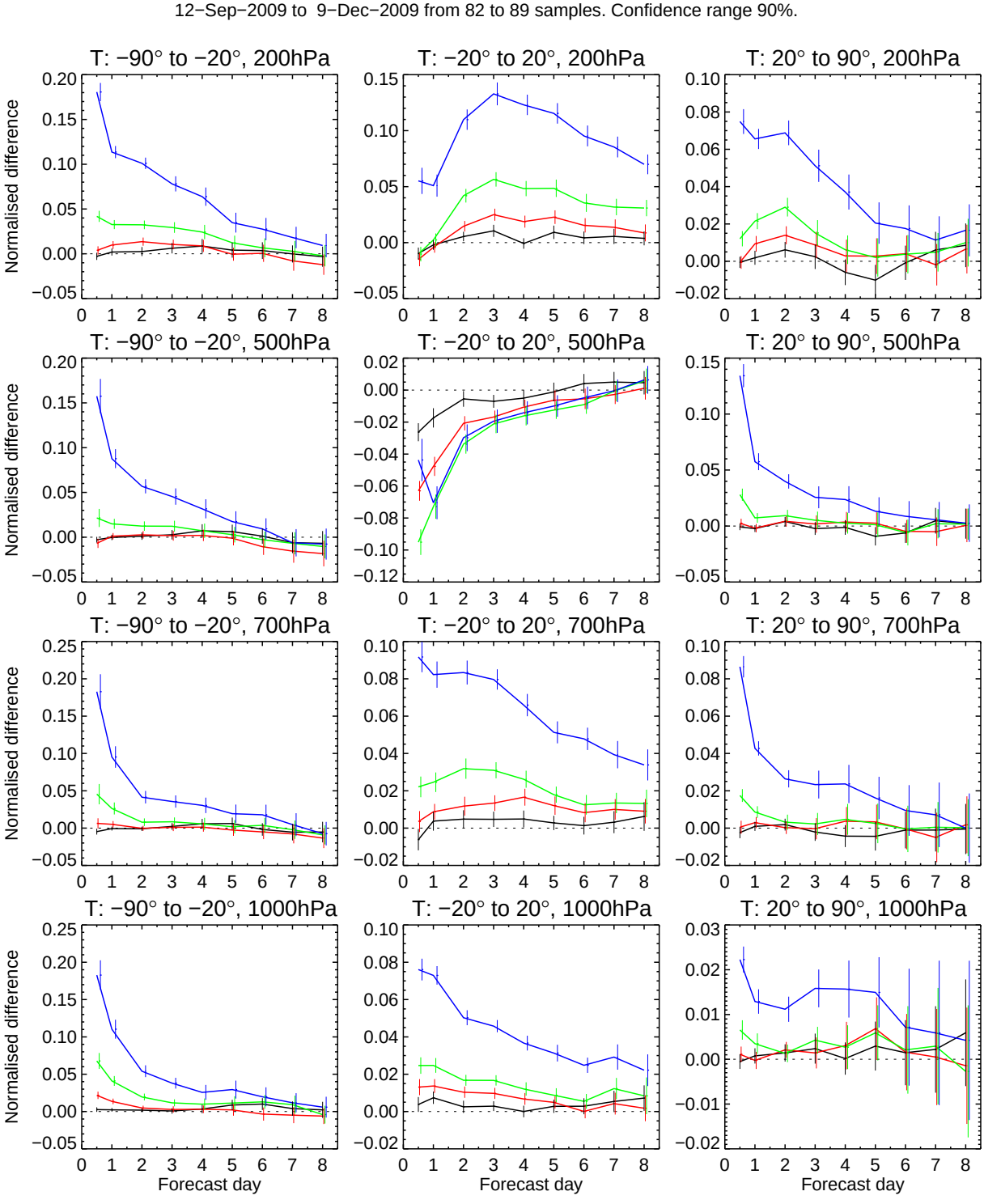

Figure 2.25: The same as Figure 2.23 but for the set of experiments using the static bias correction scheme.

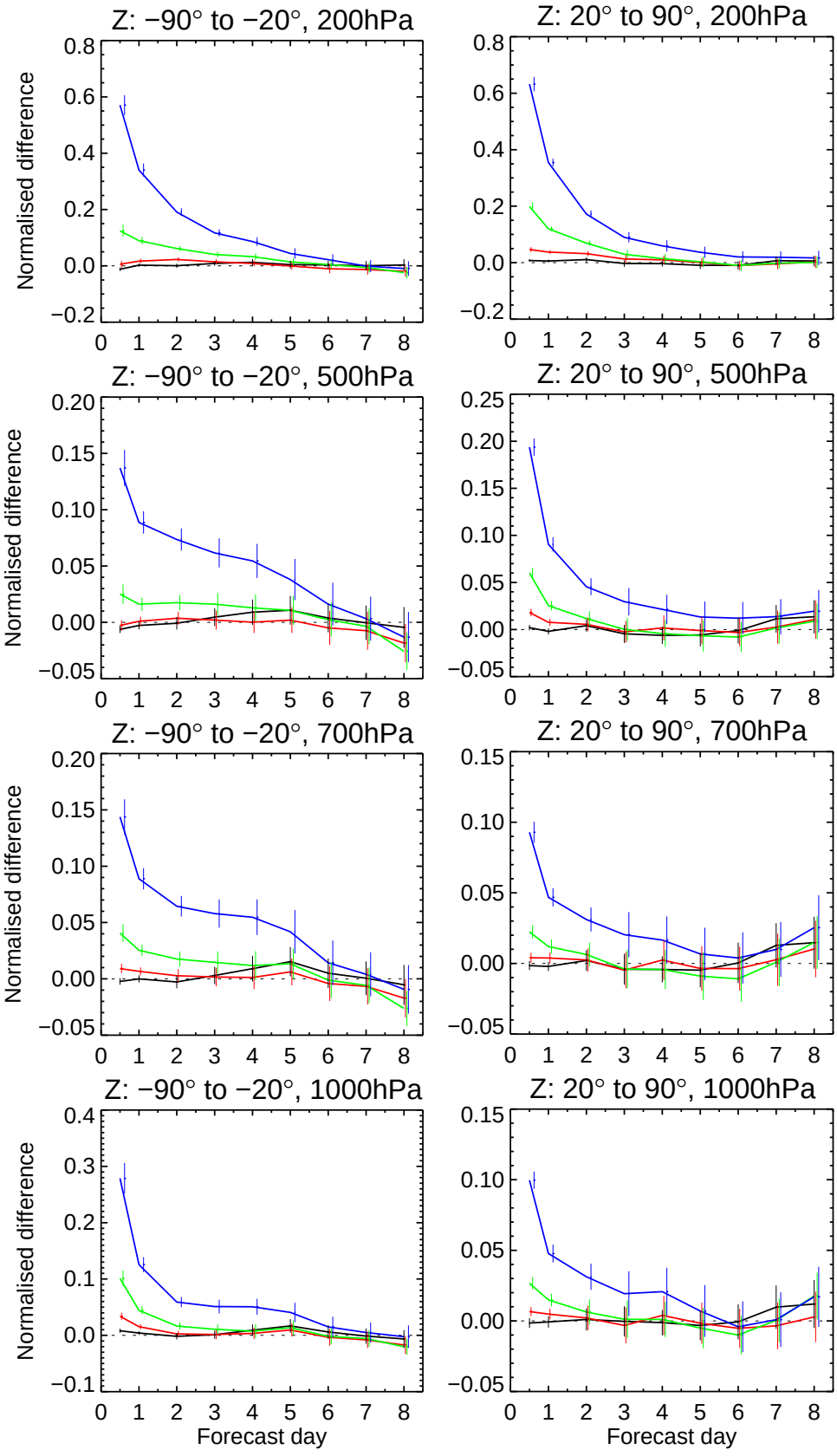

Figure 2.26: The same as Figure 2.25 but for the geopotential height.

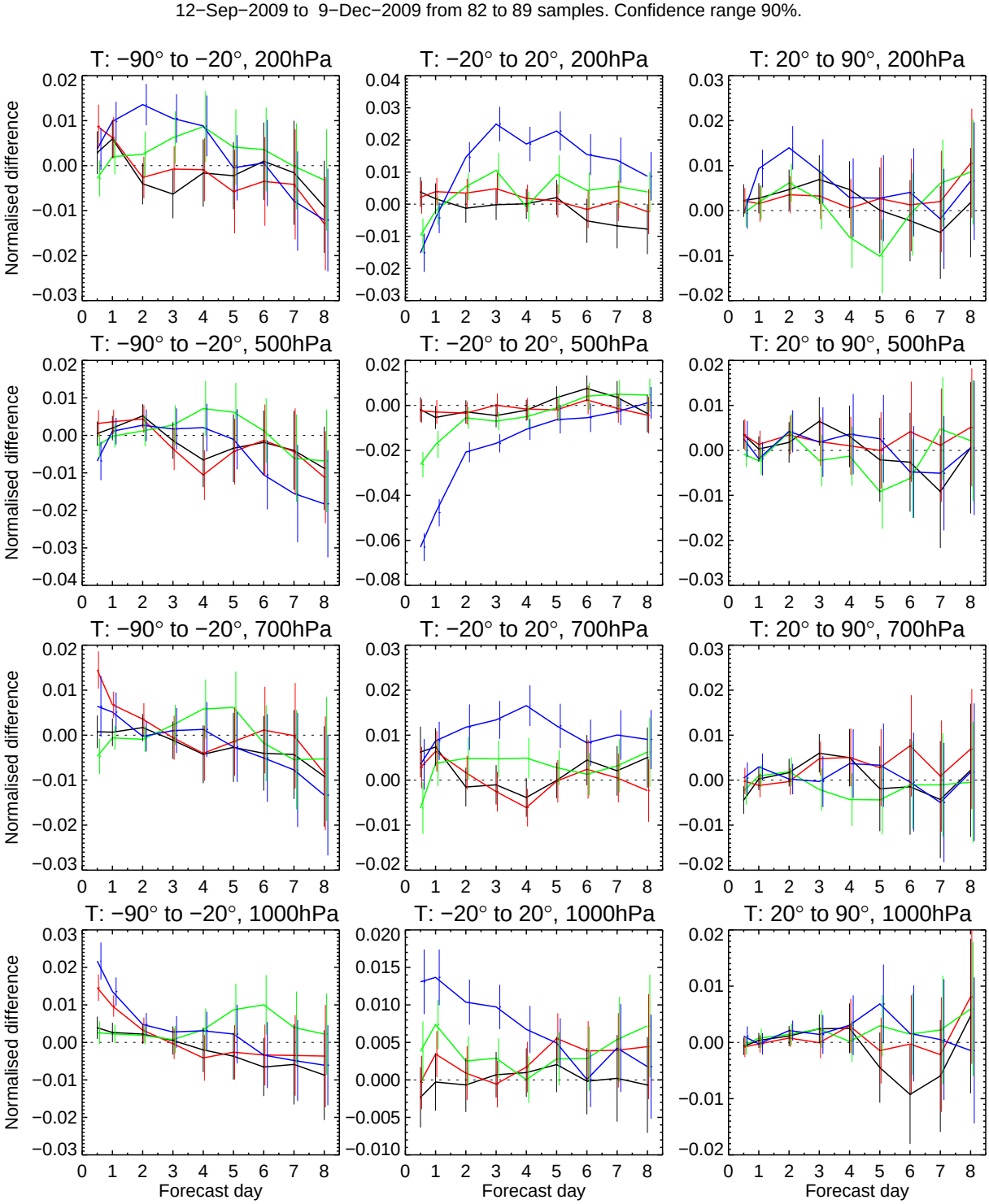

Figure 2.27: Normalized root-mean-square forecast error difference in temperature between experiments with perturbed AMSU-A observations and their reference experiment (see text) verified against the operational analyses. Two experiments are using VARBC with frequency shifts of 1.5 MHz (black) and 5 MHz (red). The two other experiments are using the static bias correction with frequency shift of 1.5 MHz (green) and 5 MHz (blue)

3 Cross-polarisation tolerance (WP3100 and WP3200)

This task comprises two work packages which have run concurrently. The first (**WP3100**) is concerned with a review of the specifications of existing and planned microwave imaging missions with respect to cross-polarisation errors. The second (**WP3200**) involves testing the impact of specified levels of cross-polarisation errors using 1D-Var experiments.

The MWI Mission Requirements Document (MRD, 2010) specifies several multi-polarisation channels. The maximum acceptable degree to which measurements of a given polarisation are contaminated by orthogonal scene polarisations defines the cross-polarisation tolerance. For typical cross-polarisation levels (established during pre-flight testing) it is normal, in the radiance pre-processing step, to correct for the cross-polarisation error. The issue is therefore: what is the impact of residual cross-polarisation errors on the analysis/retrieval problem? This issue has been tackled in **WP3200** by assessing retrieval errors using a 1D-Var scheme in which forward modelled dual-polarisation radiances are used to generate radiances with cross-polarisation errors, *i.e.* the measured radiances are generated as a linear combination of the truly orthogonally polarised radiances. The impact on ocean surface wind speed, total column water vapour and skin temperature was assessed for a range of cross-polarisation errors for the SSM/I-like window channels of the MWI instrument.

3.1 Review

Following discussions with the SSM/I and ATM teams it emerged that there are inevitable sources of cross-polarisation error for conical scanners. In particular, the configuration of the feed horn in the design of an antenna can lead to intrinsic cross-polarisation errors. The two papers reviewed below (Chu and Turrin (1973) and Rudge (1975)) concentrate on one type of cross-polarisation error which occurs in offset-fed antenna.

The advantage of offset-fed antennas (e.g. Cook et al. 1965) is that the feed does not block the field-of-view. However, the reduced symmetry of the system means that intrinsic cross-polarisation errors are introduced. Chu and Turrin (1973) demonstrated how the amplitude of cross-polarisation contaminations could be calculated as a function of the angle between the feed axis and the reflector axis, the half-angle subtended at the focus of the feed-horn by the reflector and the angle between the location at which the radiation is sampled and the axis of the beam.

They found that at the exact centre of the main beam, the cross-polarisation error was zero, but that the radiation sampled off the central axis of the beam had a non-zero cross-polarisation error that peaked just beyond the angle where the intensity fell to half its peak value (the 3-dB beamwidth). For a typical antenna configuration, the peak amplitude of the cross-polarisation error was found to be around 20 dB less than (*i.e.* 1% of) the peak intensity of the main beam. This error reduced to zero for a centrally-fed antenna. In our case, we are not interested in the distribution of cross-polarisation errors across the antenna field-of-view, only the integrated value across the field-of-view. The fact that most of the energy is within the 3-dB beamwidth suggests that the total cross-polarisation due to the offset-feed is less than 1%.

Chu and Turrin's analysis was extended by Rudge (1975). His mathematical analysis was not limited to a small angular range about the antenna boresight. Moreover, his model accommodated the possibility of small offsets in the location of the feed with respect to the focus of the parabolic reflector, enabling the performance of multiple-beam antennas to be studied. With these improvements of the method, the cross-polarisation errors still remains small and it can be concluded that these errors linked to the

offset-fed design of the antenna are less than 1%.

Following communications with Gene Poe (SSM/I team) and Bill Blackwell (ATMS team), a typical total cross-polarisation errors turned out to be around 2%. This value could be reduced to a residual error of 0.2% after correction during the preprocessing based on accurate pre-flight measurements. Moreover, it was agreed that a reasonable assumption to define one form of cross-polarisation errors is to assume that they are generated by a rotation of the polarisation plane.

3.2 1D-Var study

In the present study, the retrieval errors induced by cross-polarisation error have been assessed using the "1D-Var Pert" scheme. This method benefits from previous ESA studies carried out at ECMWF, which aimed to assess the importance of dual polarisation for near surface temperature and moisture sounding (see final report of ESA ESTEC Contract No.20711/07/NL/HE). It uses a wide range of atmospheric profiles drawn from the ECMWF global forecast model. The statistics derived from these analyses therefore represent a global picture of the impact of the aspect under test.

We focus on clear-sky scenes over ocean, as the aim is to see the impact of cross-polarisation errors on MWI surface channels 18.7, 23.8, 31.4 and 89 GHz, which are primarily dedicated to the retrieving of sea surface winds, sea-ice and total column water vapour over sea. An example of the brightness temperature spectrum in the considered frequency range is presented in Figures 3.1. Observations have been simulated for the closest equivalent SSM/I channels (summarized in Table 1) which all have weighting functions peaking at the surface (Figures 3.2). The errors in brightness temperature induced by cross polarisation errors have then been calculated and added to the simulated SSM/I observations before their assimilation in the 1D-Var system.

3.2.1 1D-Var Pert system

In the 1D-Var method, atmospheric variables are retrieved from the combination of a brightness temperature observation, a priori knowledge of the atmospheric variables (first-guess) and their respective error covariance matrices. One advantage of this technique is that non-linear problems can be handled through multiple iterations. In the ECMWF 1D-Var Pert system, the 1D-Var method can be configured so that all the inputs of the system are defined relatively to a known "true" state of the atmosphere. Knowing the "true" state allows the error statistics of the retrieved variables to be precisely evaluated, by repeating the 1D-Var Pert experiment for multiple values of the first-guess variables and over different atmospheric cases. The 1D-Var Pert method is summarized in Figure 3.3. Brief explanations on each component of the system are given below but for more details on the method, we refer to Bauer and Di Michele (2007):

- The "true" state of the atmosphere is defined by given temperature and humidity profiles, skin temperature and 10m u and v components of the wind, all extracted from the ECMWF forecast system.
- The "first-guess" states are created by adding noise (perturbations) to the true state with variances and covariances consistent with the background error distribution, as described by the background error covariance matrix. The error covariance matrix for temperature and humidity profiles is taken from the ECMWF forecast model, while prescribed values are used for the skin temperature and wind.

Centre frequency (GHz)	Polarisation	Model noise over ocean (K)	Instrumental noise (K)
18.7	V	2.52	0.51
	H	4.03	0.51
23.8	V	2.55	0.36
36.5	V	3.02	0.26
	H	6.00	0.26
89	V	2.20	0.36
	H	4.85	0.36

Table 1: The SSM/I-like channels simulated in the present study.

- The observations are simulated by running the forward model (RTTOV) with the "true" atmospheric variables in input and adding perturbations to the resulting brightness temperature which are consistent with the radiometric noise provided by in previous ESA studies carried out at ECMWF (final report of ESA ESTEC Contract No.20711/07/NL/HE, p.67). The observation error covariance matrix used in the minimization algorithm is diagonal and combines the radiometric noise and the forward model noise (taken from ESA-ESTEC (2008), pp 67). These values are given in Table 1.

For each "true" profile, the 1D-Var experiment is run for every perturbation added to the true state. The analysis error is equal to the difference between the analysed (retrieved) and "true" variables. An estimate of the bias and noise of the retrieval can then be calculated for each profile and are equal to, respectively, the mean and the standard deviation of the analysis error. These estimates of analysis bias and noise are then averaged over different atmospheric cases corresponding to different "true" atmospheric conditions. Error statistics can also be mapped into brightness temperature space, by running the forward model with the retrieved atmospheric variables in input.

To get an idea of the impact of each considered SSM/I channel on the retrieval noise, these have been individually assimilated in the 1D-Var system, and the resulting analysis error standard deviations are shown in Figure 3.4 for the wind speed, total water vapour column and skin temperature. The best impacts are those where the analysis error standard deviation is the most reduced relatively to that of the first-guess. The main impact is on the total column water vapour with a noise reduction greater than 40% for all channels and reaching a maximum of 80% for the 23.8 GHz channel with vertical polarisation. Impacts are very small for the skin temperature. For the wind speed, there is no measurable impact of the channels with vertical polarisation and a small positive impact of the channels with vertical polarisation.

3.2.2 Introduction of the cross-polarisation error

From the discussion with the ATMS and SSM/I teams summarised in 3.1, the cross-polarisation errors have been calculated on the basis that they are generated by a rotation of the polarisation plane. A range of cross-polarisation errors will be tested, each generated as the linear combination of the truly orthogonally polarised radiances $R_\perp$ and $R_\parallel$. The resulting perturbed radiances $R^*_\perp$ and $R^*_\parallel$ take the following form:

$$R^*_\perp = \cos^2(\theta)R_\perp + \sin^2(\theta)R_\parallel \quad (8)$$

$$R^*_\parallel = \sin^2(\theta)R_\perp + \cos^2(\theta)R_\parallel, \quad (9)$$

where θ is the polarisation "twist" angle. The polarisation error is defined as the fraction of the orthogonal signal introduced in the observation, which is equal to $\sin^2(\theta)$. Experiments have been run for polarisation errors equal to 0.2, 1, 2, 5 and 10%, which correspond to values for θ of respectively 2.6, 5.7, 8.1, 13.9 and 18.4°. Figures 3.5 and 3.6 (black line) show the corresponding bias and noise in simulated brightness temperature introduced by the cross-polarisation error. For a cross-polarisation error of 10%, the bias remains within roughly ± 2 K (negative for vertically polarised channels and positive for horizontally polarised channels). For this same value of polarisation error, the noise in brightness temperature is less than 0.1 K.

The cross-polarisation error is added to the simulated brightness temperature just before it is assimilated in the 1D-Var as shown in Figure 3.3. It has to be noted that the addition of this error has an impact on the convergence of the 1D-Var minimization algorithm. The larger the cross-polarisation error, the lower is the number of perturbed first-guess atmospheric profiles for which convergence is achieved. This also impacts the number of "true" profiles on which statistics are performed. In the present study, among the 80 "true" atmospheric profiles used in total, 51 of them pass the convergence criterion for all tested cross-polarisation errors except for the 10% error, for which 46 profiles pass the convergence criterion.

The perturbations added to a given "true" profile are symmetrical, but the rejection of some perturbed states due the lack of convergence introduces a small sampling effect in the error statistics. Thus, the "accepted" first-guess profiles can be slightly biased, depending on the size of the cross-polarisation error. Biases in the first-guess of wind speed and brightness temperature as seen in Figures 3.5 and 3.7 can also appear due to the non-linear relationships relating them to the variables to which the perturbations are added. Nevertheless, these effects do not prevent us from quantifying the impact of different levels of cross-polarisation error on the retrieved variables, by comparing the statistics of the analysis relatively to that of the first-guess.

3.2.3 Results

The 1D-Var system has been run with 80 profiles in input, each of them being perturbed 70 times. All the channels specified in Table 1 have been assimilated together. A first experiment has been performed without adding any cross-polarisation error. Other experiments have been performed for the different cross-polarisation errors defined in the previous section.

The overall performance of the assimilation can be seen in Figures 3.5 and 3.6, where all error statistics are mapped into brightness temperature space. The analysis appears to be closely tied to the observations for cross-polarisation errors below 5% and get closer to the first-guess for larger values of the cross-polarisation errors (Figure 3.5). The level of noise in the analysis is well below that in the first-guess and close to the instrument radiometric noise (Figure 3.6). Note that the observation error standard deviations used in the 1D-Var assimilation also includes those of the model.

The main impact of the cross-polarisation errors on the quality of the retrievals is in the analysis bias (Figure 3.7). The difference of first-guess error biases are explained in the last section. The bias in the analysis strongly increases with increasing errors in cross-polarisation. The analysis bias introduced by the cross-polarisation error can be seen in the right hand-side panels of Figure 3.7 by comparing the analysis-minus−first-guess biases for cases with and without cross-polarisation error. Such biases remain very small for the 0.2% cross-polarisation errors with values less than 0.1 m.s^{-1} for the wind speed, and insignificant for the WV column and skin temperature (given the error bars). The largest changes in analysis bias are found for the 10% cross-polarisation error with values around $+2$ m.s^{-1} for the wind speed, -1.5 kg.m^{-2} for the water vapour column and -0.3 K for the skin temperature. These values are

very large for the wind as it corresponds to an error in wind speed of 30%. However, a 10% error is a very large estimate of what the actual cross-polarisation might be. For a more reasonable estimate of the cross-polarisation error such as 2%, the change in analysis bias represents 10% of the wind speed, 3% of the WV column and 0.02% of the skin temperature signals. The bias changes in water-vapour column and skin temperature retrievals are comparatively smaller. In terms of WV profiles, the bias introduced by cross-polarisation errors affects a deeper layer of the atmosphere for error greater than 2% compared to the existing bias in the first-guess, with measurable impact up to 600 hPa for cross-polarisation error of 5 and 10% (Figure 3.9).

The impact of cross-polarisation error on analysis noise is shown in Figure 3.8. The wind speed error standard deviation of the analysis is roughly 12% smaller than that of the first-guess. This value is much larger than that shown in Figure 3.4 where channels were assimilated individually, which highlights the benefit of assimilating multiple channels with different polarisations.

The noise of the retrieved water vapour column, wind speed and skin temperature appear to be only weakly affected and in some cases not affected at all by cross-polarisation errors. The experiment has then be rerun with the standard deviation of the observation errors (radiometric and forward model errors) used in the 1D-Var system divided by 2, in order to give more weight to the observations. Figure 3.10 shows a degradation of the retrieval noise only for the 10% cross-polarisation errors, confirming the low dependence of the retrieval noise of the wind speed on the cross-polarisation error. On the contrary, the wind direction appears to be significantly affected by the the cross-polarisation error, as seen in Figure 3.11, which shows the error standard deviation in radial and tangential winds. The statistics associated with those two variables has been calculated by simply doing the following transformation:

$$dr = \frac{udu + vdv}{\sqrt{u^2 + v^2}} \tag{10}$$

$$dt = \frac{vdu - udv}{\sqrt{u^2 + v^2}}, \tag{11}$$

where du and dv are the departures from the truth of the u and v wind components and dr and dt are respectively the departures from the truth of the radial and the tangential winds. As seen in Figure 3.11, the noise in analysed radial wind depends less on cross-polarisation errors than the noise in analysed tangential wind, for which the noise degradation reaches 40% for the 10% cross-polarisation error. This is is presumably due to differences in the dependence of orthogonally polarised brightness temperatures on these two components of the wind.

3.3 Conclusions

The impact of the cross-polarisation errors on the quality of the ocean wind speed, water vapour column and skin temperature analysis was investigated running the ECMWF "1D-Var Pert" system to assimilate simulated observations from SSM/I like surface channels. Cross-polarisation errors were added to simulated observations just before their assimilation in the system. These additional observation errors introduce biases, noise and error correlations between channels which are not accounted for in the observation error covariance matrix used in the 1D-Var assimilation process, hence degrading the level of optimality of the method.

With the 1D-Var configuration used in the present study, it has been found that a cross-polarisation error of 2% generates biases in retrieved surface wind (10% of total wind speed), water vapour (-3% of total column water vapour) and skin temperature (around -0.06K). The noise of the retrievals does not appear

to be affected by the 2% cross-polarisation error but this latter has been found to have a significant impact on the noise in the wind direction (increase of 0.2 $m.s^{-1}$ in tangential wind noise).

From discussions with the ATMS and SSM/I teams, the value of 2% appeared to be a reasonable estimate of the cross-polarisation error. This value could, in principle, be reduced to a residual error of 0.2% after correction during the preprocessing, based on accurate pre-flight measurements. In this case the impact of the cross-polarisation error is very low for the wind speed bias (0.8%) to insignificant for other retrieved variables and in terms of increase of the noise level.

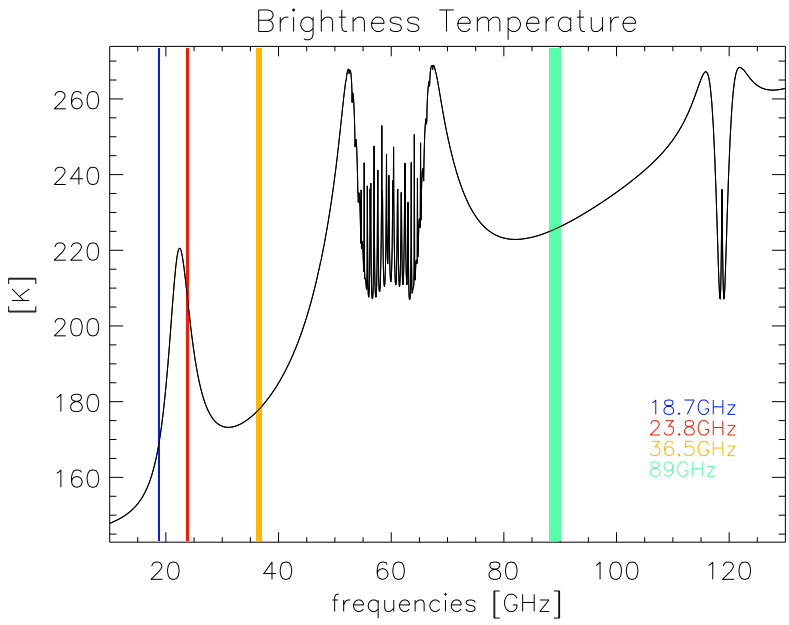

Figure 3.1: Simulated brightness temperature calculated with the off-line radiative transfer model from typical tropical temperature and water-vapour profiles. The SSM/I like channels shown are those used in the cross-polarisation study.

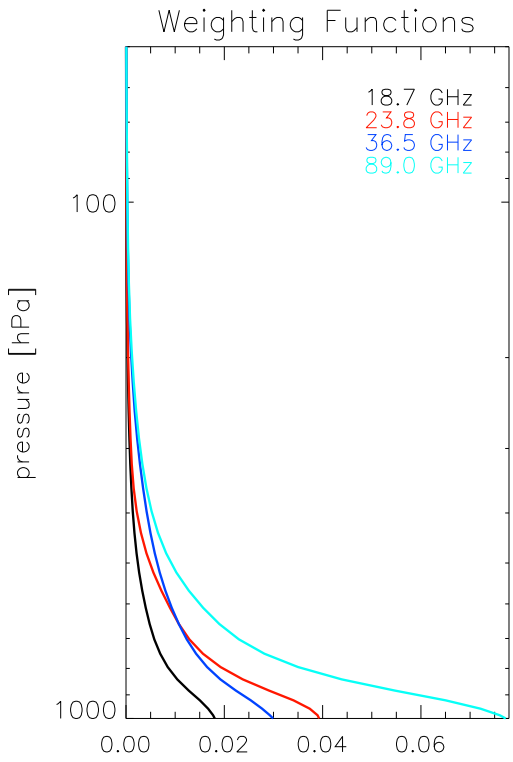

Figure 3.2: Weighting functions calculated from typical tropical profiles for the SSM/I like channels used in the cross-polarisation study..

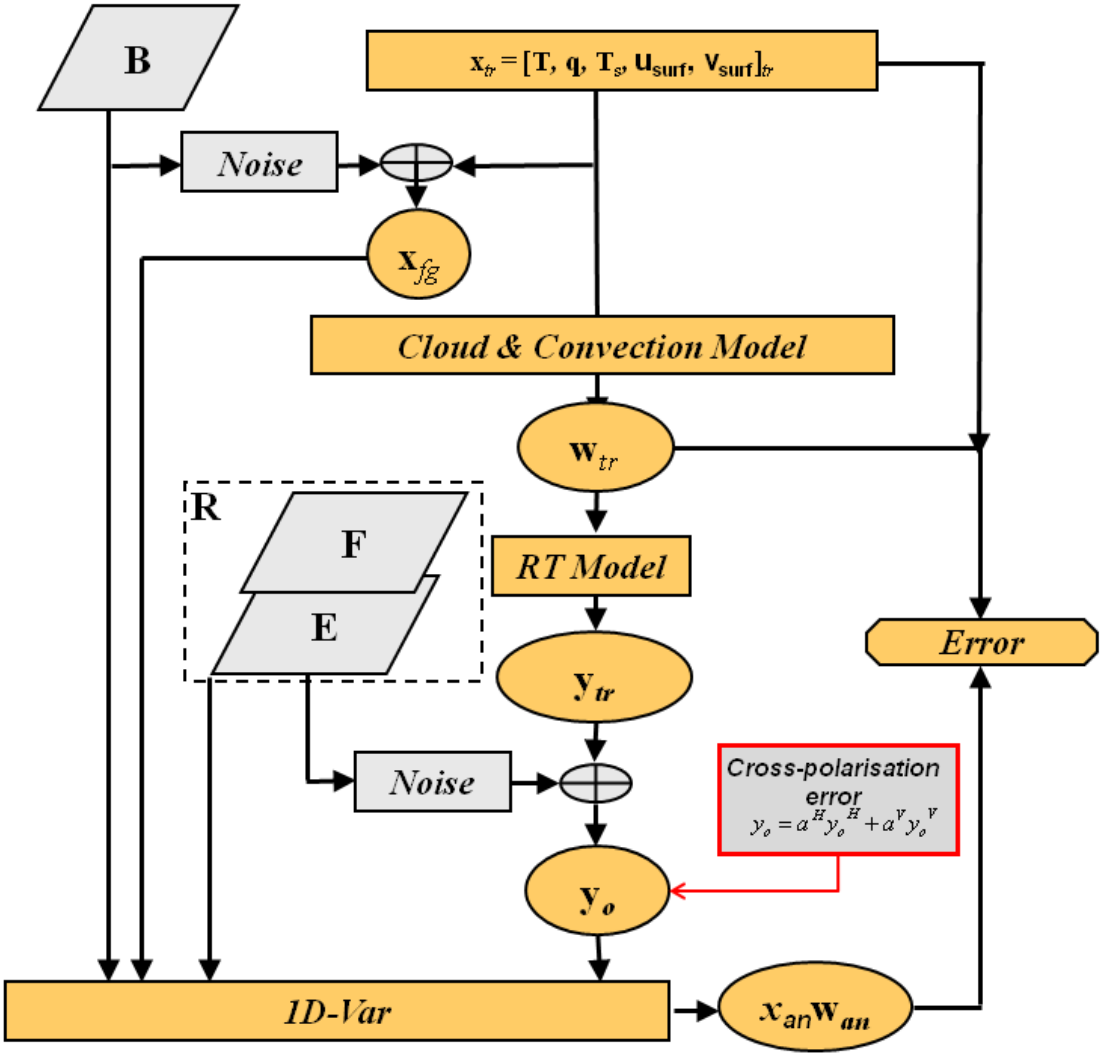

Figure 3.3: The 1D-Var Pert retrieval scheme (courtesy Sabatino Di Michele). **B**, **E** *and* **F** *are the error covariance matrices for respectivelly the first-guess, the instrument (radiometric noise) and the forward model.* **R** *is the observation error covariance matrix which is the addition of* **E** *and* **F**.

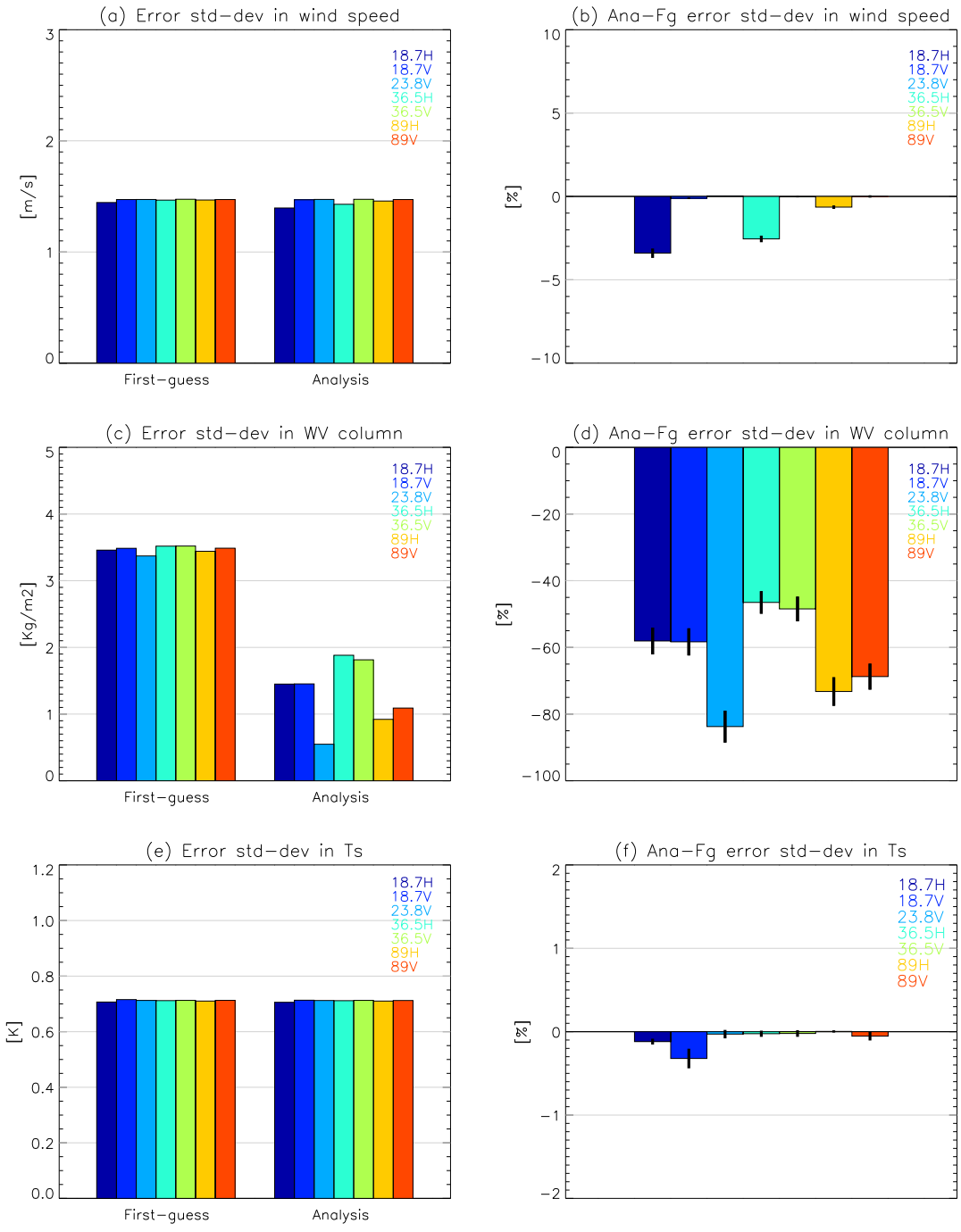

Figure 3.4: Error standard deviation of the first-guess and analysis (left panels) and their difference expressed as percentage of the standard deviation of the first-guess error (right panels) for (a) and (b) the wind speed, (c) and (d) the total water vapour column, and (e) and (f) the skin temperature. Each bar corresponds to a given channel as described in the legend. The error bars on the right panels represent the standard error calculated over the ensemble of atmospheric "true" profiles.

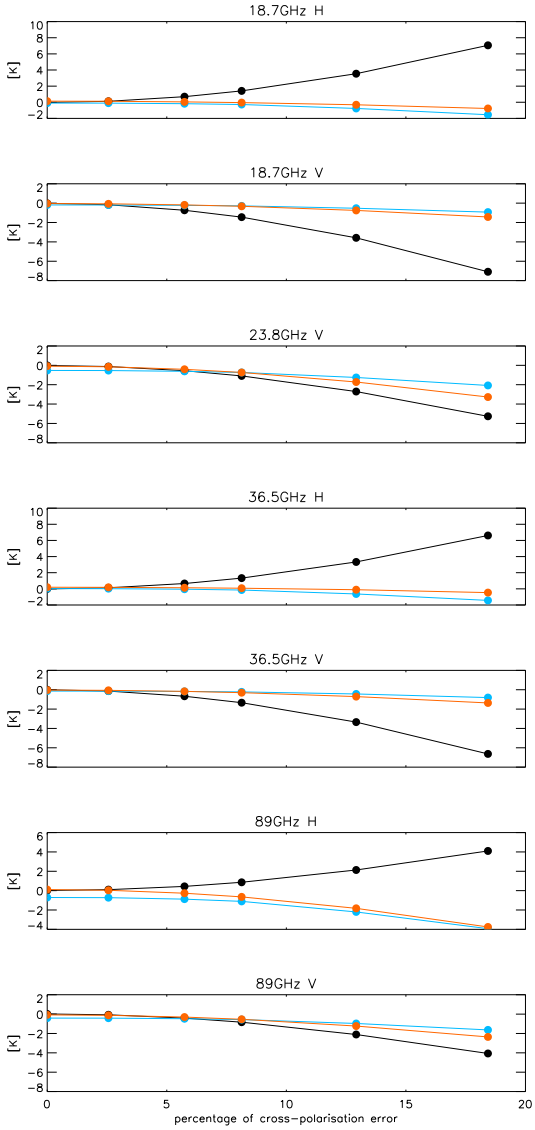

Figure 3.5: The bias introduced by cross-polarisation errors in the simulated observation (black), first-guess (blue) and analysis (red) brightness temperature.

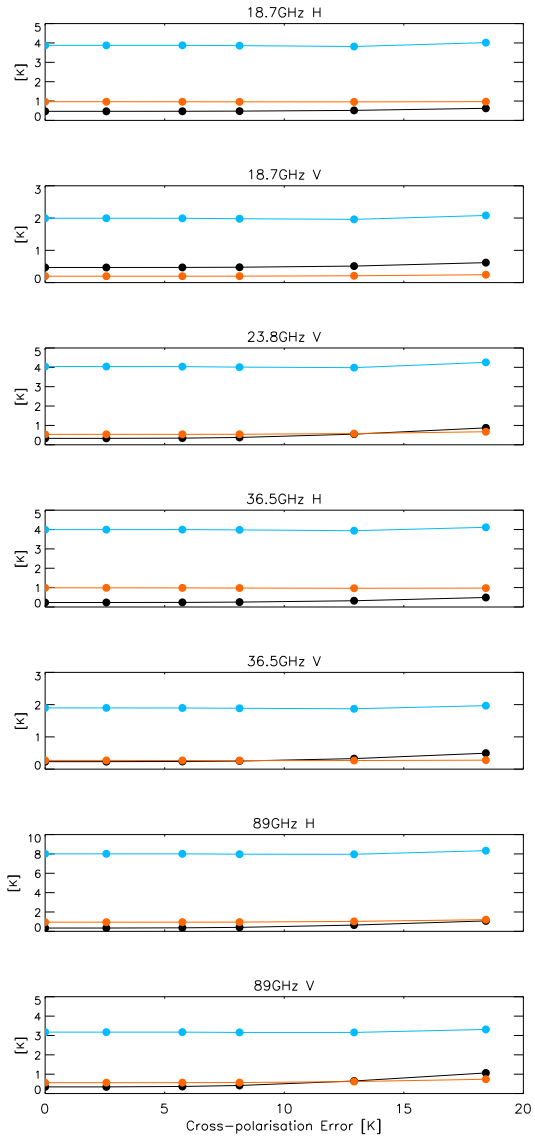

Figure 3.6: The noise introduced by cross-polarisation errors in the simulated observation (black), first-guess (blue) and analysis (red) brightness temperature.

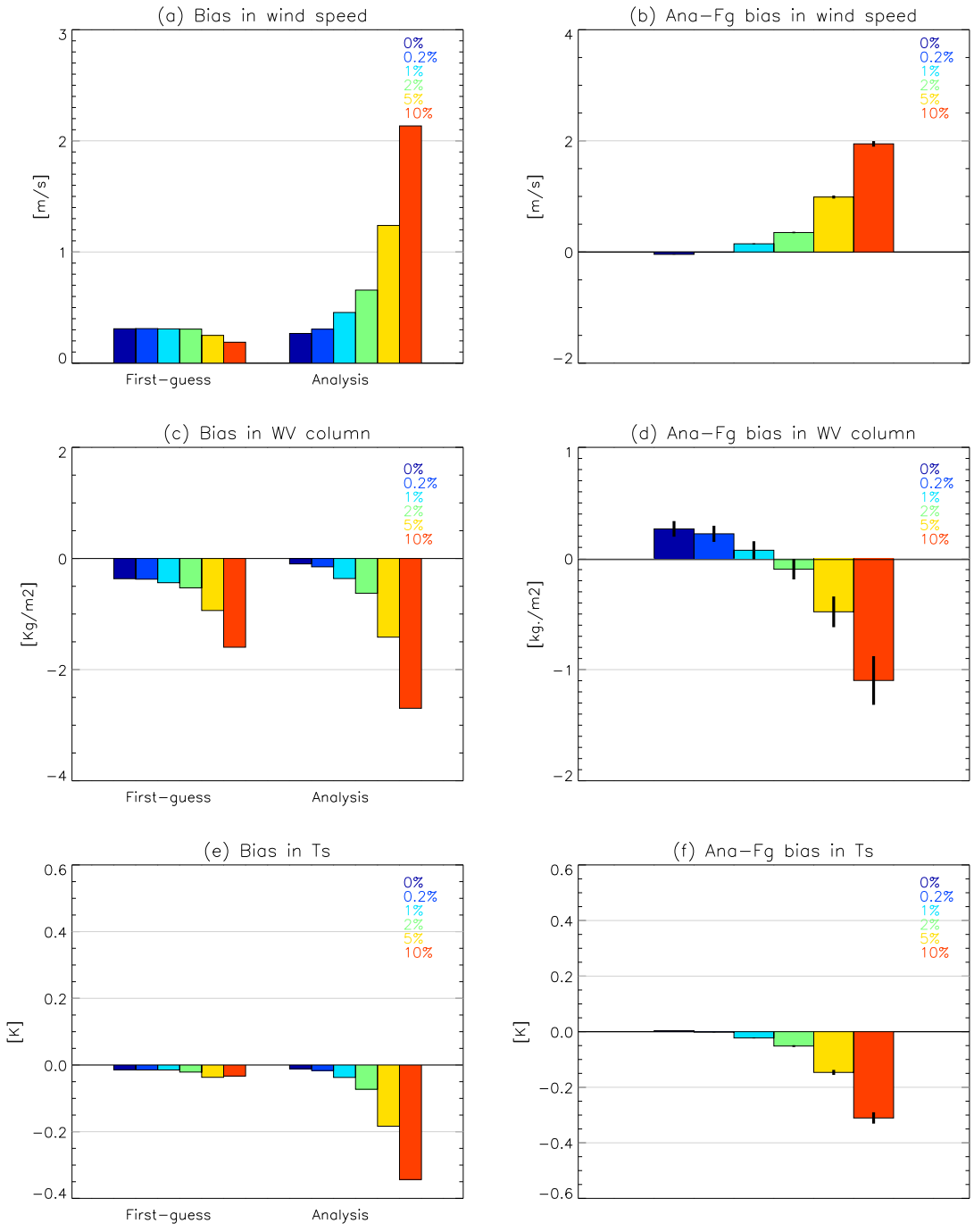

Figure 3.7: The first-guess and analysis error bias (left panels) and their difference expressed as percentage of the first-guess error bias (right panels) for (a,b) the wind speed, (c, d) the total water vapour column, and (e, f) the skin temperature. Each bar corresponds to a given cross-polarisation error the value of which is described in the legend. The error bars on the right panels represent the standard error calculated over the ensemble of atmospheric "true" profiles.

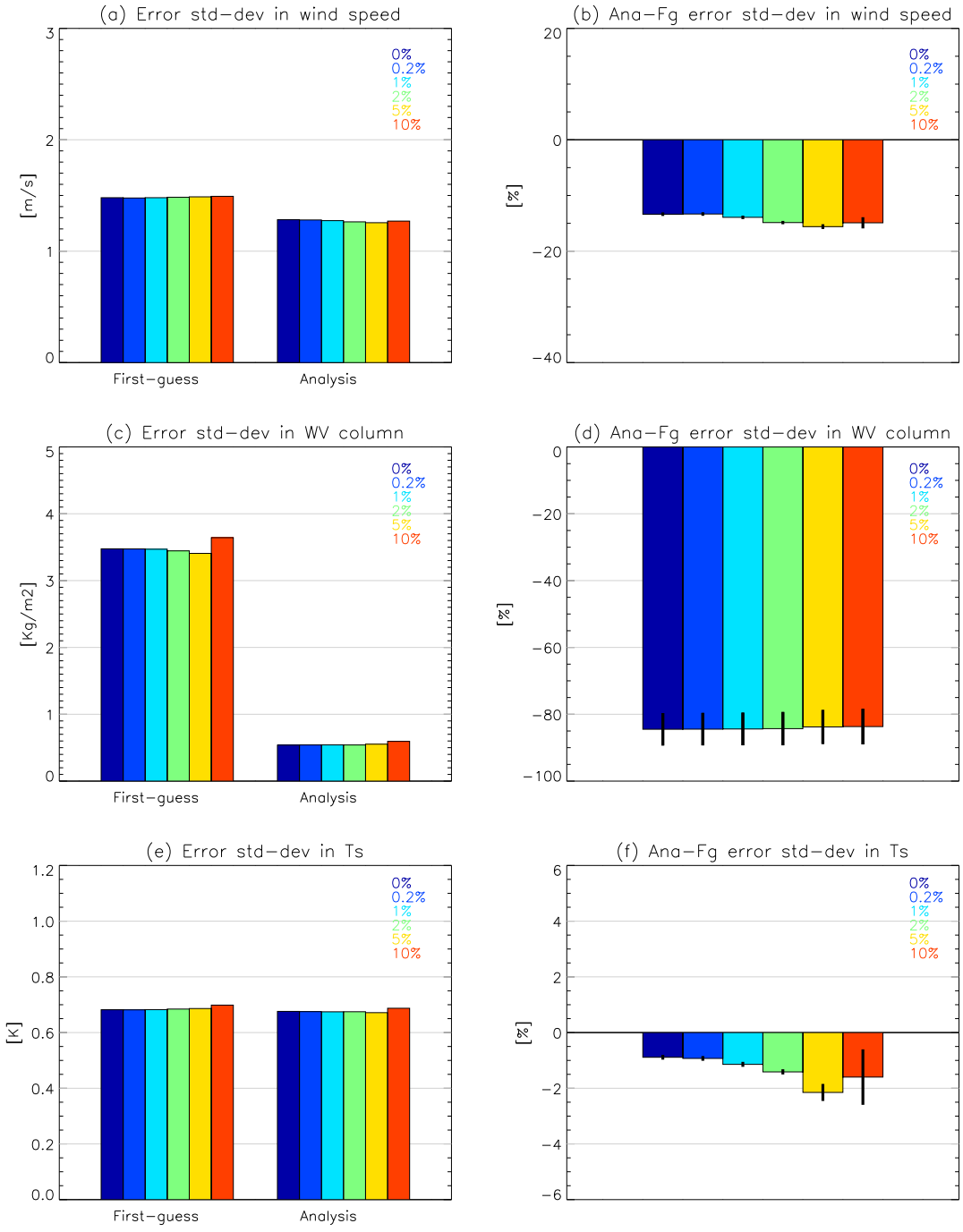

Figure 3.8: The same as Figure 3.7 but for the error standard deviation.

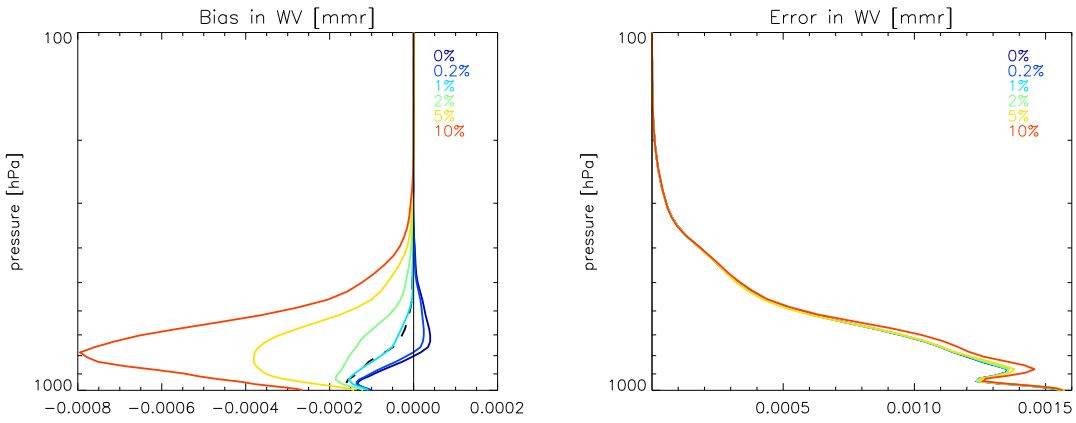

Figure 3.9: The error bias (left panels) and error standard deviation (right panel) of the first-guess (dashed line) and analysis (solid line) water vapour mixing ratio. Each color corresponds to a given cross-polarisation error the value of which is described in the legend.

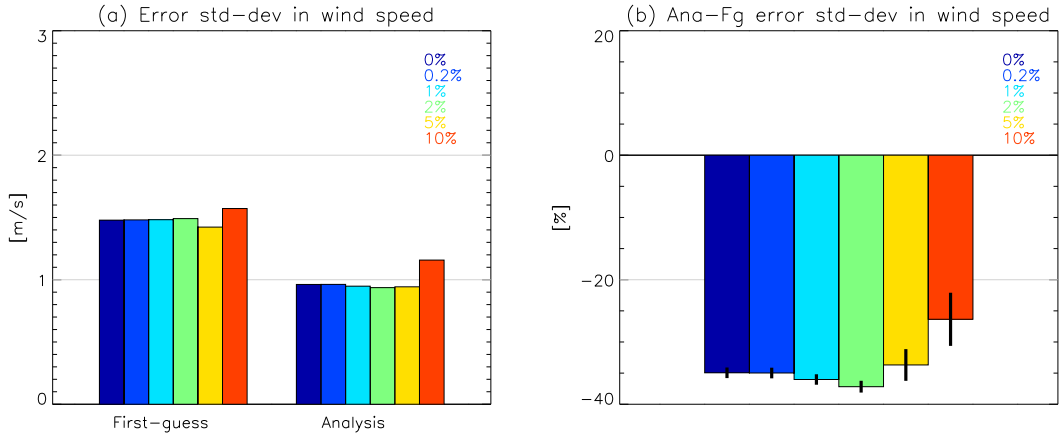

Figure 3.10: The first-guess and analysis error standard deviation (left panels) and their difference expressed as percentage of the first-guess error standard deviation (right panels) for the wind speed for an experiment where values of the observation error standard deviations used in for the 1Dvar assimilation have been divided by 2. Each bar corresponds to a given cross-polarisation error the value of which is described in the legend.

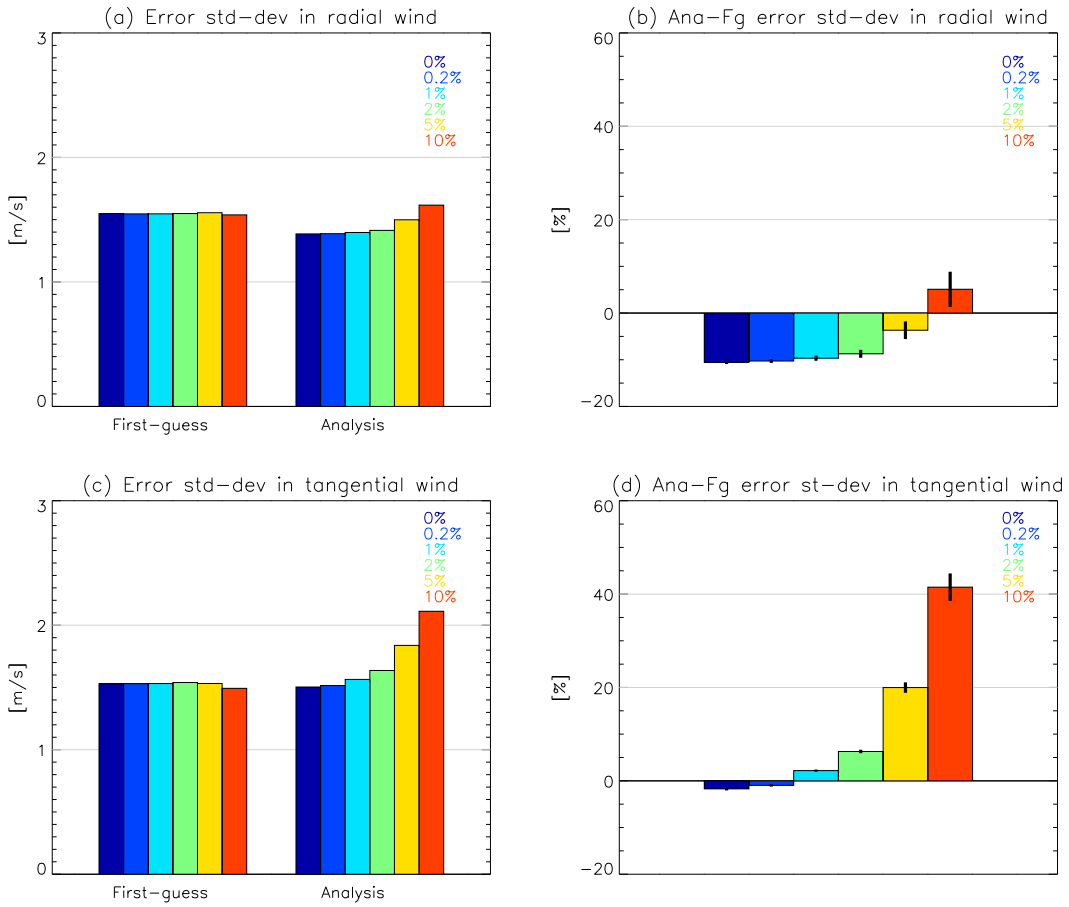

Figure 3.11: The first-guess and analysis error standard deviation (left panels) and their difference expressed as percentage of the first-guess error standard deviation (right panels) for (a,b) the radial wind and (c,d) the tangential wind. Each bar corresponds to a given cross-polarisation error the value of which is described in the legend.

4 Channel Selection (WP4100)

4.1 Background

Microwave imager channels are generally located in window channel regions of the microwave spectrum, for which the ground-to-space transmission is significantly non-zero. Measurements in certain parts of the microwave spectrum are potentially prone to radio frequency interference (RFI) effects. Such interference effects can result from emissions from active services emitting at the Earth's surface or, for example, through emissions from communications satellites being reflected from the Earth's surface (REFS). The allocation of spectral bands is coordinated and regulated through the International Telecommunications Union (ref). The allocation of bands, designated for use by passive microwave sensors, in the 15 - 95 GHz region is summarised in Table 1 below (see REF).

Frequency bands (/GHz)	Bandwidth (MHz)	Allocation
15.20 - 15.35	150	s
15.35 - 15.40	50	**P**
18.60 - 18.80	200	p
21.20 - 21.40	200	p
22.21 - 22.50	290	p
23.60 - 24.00	400	**P**
31.30 - 31.50	200	**P**
31.50 - 31.80	300	p
36.00 - 37.00	1000	p
50.20 - 50.40	200	**P**
52.60 - 54.25	1650	**P**
54.25 - 59.30	5050	p
86.00 - 92.00	6000	**P**

Table 1: Allocation of passive remote sensing bands for channels in the spectral region 15.20 - 92.00 GHz. **P** *indicates Primary Allocation - shared only with other passive services, p indicates primary allocation, shared with active services and s indicates secondary allocation.*

4.2 Aim of the studies

Workpackage (**WP4100**) concerns the specification of channels in the 31-37 GHz region, given the allocation of protected frequencies in this part of the microwave spectrum and with the potential benefit of including additional channels in the 15-20 GHz region for the improvement of humidity analyses. The specific investigations involved:

- Assessing the 36.5 GHz (MRD specification, shared allocation) *versus* 31.4 GHz (primary protection) bands with respect to the analysis of water vapour and cloud. Due to the availability of the RTTOV coefficients, the channel centred on 37 GHz has been used in place of the 36.5 GHz channel. We do not believe this significantly changes the results as the BT does not strongly depends on frequency in this part of the spectrum.
- Assessing the value of channels in the range 15-20 GHz for the retrieval/analysis of water vapour, relative to the channel centred on the water vapour absorption line at 22.235 GHz. If useful in-

formation is available in this spectral region there would be a case for exploiting the band at 15.35-15.40 GHz which has primary protection.

Previous EUMETSAT/ESA studies on channel selection (ESA ESTEC Contract No.20711/07/NL/HE) made use of the method of *information content analysis*. Here the approach is slightly different but is still based on the principle of optimal estimation. Background and analysis (or retrieval) errors of retrieved quantities are calculated for each channel, allowing us to determine the channel which has the strongest impact on the retrieval error.

4.3 Method

One way to assess the impact of assimilating a particular observation on a given atmospheric variable is to compare the error affecting the variables *prior to* and *after* the assimilation of the considered observation, *i.e.* to compare analysis and first guess (or background) errors. It can be shown than in the linear case (Rodgers, 2000) the analysis error covariance matrix **A**, given by optimal estimation theory, can be expressed as follows:

$$\mathbf{K} = \mathbf{B}\mathbf{H}^T(\mathbf{H}\mathbf{B}\mathbf{H}^T + \mathbf{R})^{-1} \quad (12)$$

$$\mathbf{A} = (\mathbf{I} - \mathbf{K}\mathbf{H})\mathbf{B}, \quad (13)$$

where **B** is the background error covariance matrix, **R** is the observation error covariance matrix, **H** is the Jacobians of the observation operator, which gives the gradients of the observed quantity with respect to the control variables.

In this study, **A** is calculated as follows: first **H** is obtained by running the RTTOV-K code (part of the RTTOV-9 software package (Eyre, 1991; Saunders, 2008) given a set of atmospheric profiles drawn from a database of profiles extracted from cycle 31R2 of the ECMWF forecasting system. These profiles correspond to clear or cloudy scenes depending on the case of interest. The control variables are temperature and humidity profiles, skin temperature and surface winds. Additional variables for the cloudy-sky cases are cloud liquid water content, cloud ice water content, rain and snow. Typical humidity and temperature profiles from the database and the corresponding Jacobians are shown on Figures 4.1 and 4.2.

For temperature and humidity, **B** is the operational analysis error fields corresponding to each sampled profile (Andersson et al. 2005). For the other variables, the values of **B** are calculated as in ESA ESTEC Contract No.20711/07/NL/HE (2008, section 4). As for WP3200, the observation error covariance matrix used in the minimization algorithm is diagonal and combines the radiometric noise and the forward model noise (taken from Bauer and Di Michele (2007)).

The benefit provided by assimilating each considered channel is measured by the difference between the standard deviation of the analysis and background errors, given by the square root of the diagonal elements of the **A** and **B** matrices.

4.4 Comparison of 31.4 GHz and 37 GHz bands

The impact of the 31.4 GHz channel on humidity and cloud analyses over oceans has been compared to that of a channel centred on 37.0 GHz of the same bandwidth (400 MHz). Both horizontal and vertical

polarized observations have been assimilated. The analysis and background errors have been calculated and averaged over all profiles.

Figure 4.3 shows the water vapour columns and liquid water paths associated with the cloudy profile database together with the computed error reduction, relative to the first-guess error, resulting from the assimilation of the 31.4 and 37.0 GHz channels. The results are binned by latitude, emphasising the strong latitudinal dependence of the water vapour column and liquid water paths. Also evident is a strong dependence of the error reduction on the water vapour columns and liquid water paths. This is to be expected as the isotropic brightness temperature error characteristics translate to a water vapour/liquid water path equivalent error which is proportionally smaller for higher water vapour columns / liquid water paths as shown in Figure 4.3 panels (c) and (d). Plotted this way there is no clear difference in the analyses from the 31.4 and 37.0 GHz channels. The error reduction for 31.4 and 37.0 GHz channels is shown in Figure 4.4 as a histogram plot to better delineate the tropical (high column water, large error reductions) *versus* extra-tropical (low column water, small error reductions) impacts. Again, the difference between the 31.4 and 37.0 GHz channels is not clear. Figure 4.5 shows the mean error reduction over all profiles in the tropics and extra-tropics for both channels for water vapour column and for cloud liquid water path. The 37.0 GHz channel shows marginally better performance than the 31.4 GHz channel. The impact on the retrieved profiles are shown in Figure 4.6 which demonstrates that these window channels mainly influence humidity profiles below 700 hPa. This figure shows again that the 37.0 GHz channel gives a slight improvement over the 31.4GHz channel, particularly below 800 hPa.

Figures 4.7-4.10 show analogous plots for the database of clear sky profiles. The conclusions are broadly similar: the error reductions are largest for the tropical profiles, and the 37.0 GHz channel shows performance very close to that from the channel at 31.4 GHz. The error reductions in water vapour, at 65%, in the topics are larger than those observed for the cloudy dataset where tropical water vapour column errors are reduced by 45-50%. Figure 4.10 shows that improved performance is obtained in the tropics for levels in the range 1000-900 hPa.

4.5 Comparison between 15-20 GHz and 22.235 GHz bands in clear-sky

The impact of the 22.235 GHz on humidity analyses over oceans has been compared to that of the following channels (shown in Figure 4.11) : 15.375 GHz-a , 15.375 GHz-b , 16.350 GHz, 17.350 GHz, 18.350 GHz, 19.350 GHz. As in the previous section, both horizontal and vertical polarized observations have been assimilated for each channel. All the channels have a bandwidth of 250 MHz, except the channel 15 GHz-a, which has a bandwidth of 50 MHz.

The instrumental noise in the 15.375 GHz-b channel has been set to 0.51 K (Di Michele and Bauer, 2007). These values have also been used for the channel 15.375 GHz-a, although the instrumental noise is expected to be greater for this channel due to its narrower bandwidth. However, this should not have a large impact on the result. Indeed, even if the difference in instrumental noise between the two channels is of a factor $\simeq$2 (from equation 1 in Di Michele and Bauer (2007)), the instrumental noise is still much less than the forward model error (set to 2.5 K for the vertical polarization and 4 K for the horizontal polarization (Di Michele and Bauer, 2007)) and would therefore have a limited impact on the observation error, which is the square root sum of the instrumental and forward model errors.

Figure 4.12 shows the error reductions for the channels at 15.375 GHz and 22.235 GHz. For the 22.235 GHz channel errors in water vapour column are reduced by 70-90% with larger error reductions in the tropics where water vapour columns are largest. For the 15.375 GHz channel the errors are reduced by 10-30%. The monotonic improvement in the analysis error reduction as channels are defined closer

to the water vapour absorption line centre at 22.235 GHz is illustrated in Figure 4.13. The mean error reductions are illustrated in Figure 4.14. In terms of the reduction in the error of the water vapour profile, Figure 4.15 shows that the peak of the error reduction, in the range 750 - 800 hPa is approximately four times larger for the 22GHz channel than for the 15.375 GHz channel.

4.6 Conclusions

The performance of the 31.4 GHz channel, with primary protection, and the 37.0 GHz channel (with shared allocation) is very similar if the same bandwidth is used.

Channels in the range 15 - 19 GHz do have information on water vapour and, when assimilated individually, reduce analysis errors. The benefit of additional channels drops off monotonically with distance of the band centre from the centre of the water vapour absorption line, such that a channel at 15 GHz reduced first guess errors by 25% of the error reduction achieved by the 22.235 GHz channel, *i.e.* in broad terms a channel at 15 GHz is four times less useful than the channel at 22.235 GHz.

The recommendation from this study, therefore, is that:

- A channel centred at 31.4 GHz, utilising the 200 MHz of fully protected bandwidth, be retained in preference to a channel using the 36.0-37.0 GHz region which has shared allocation with active services *if a single channel has to be specified in this region*.
- If a second channel can be added without cost implications, not withstanding the risk of RFI in the shared band, then useful improvements to the moisture analysis could be obtained by adding a second channel in the 36.0 - 37.0 GHz range, using 200 MHz or more of this region of spectrum.
- The limited additional information available in the protected band at 15.35 - 15.4 GHz, amounting to 25% of that available at 22.235 GHz, does not justify the inclusion of an additional band at 15 GHz. An additional consideration here is that the information at 15.375 GHz is also significantly lower than that available from the (fully protected) 31.4 GHz band.

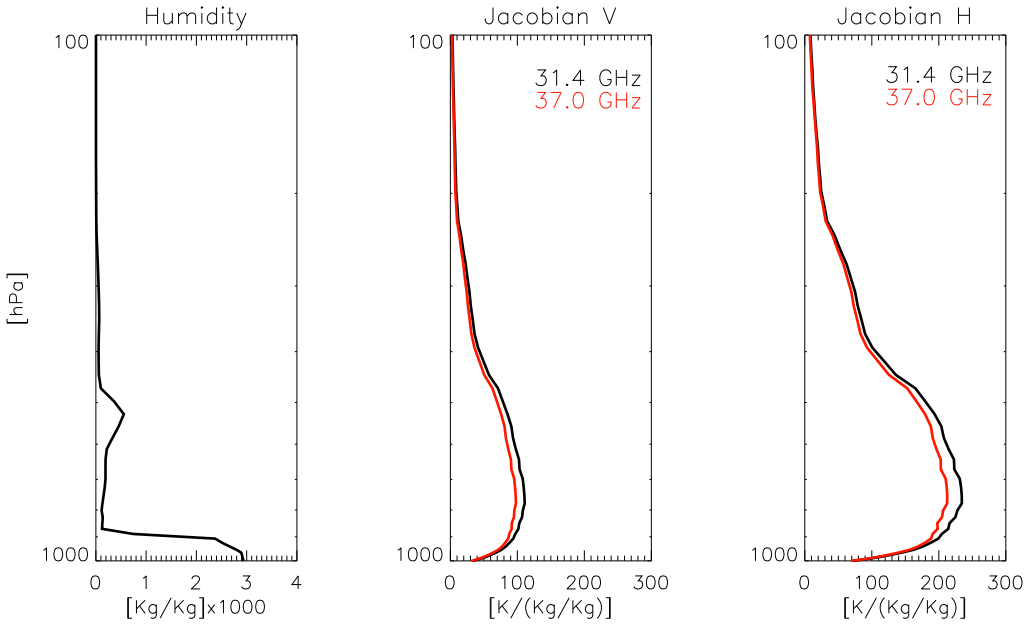

Figure 4.1: Typical dry atmosphere humidity profile (left) and the associated Jacobians for the vertical (middle) and horizontal (right) polarization of the 31.4 GHz (black) and 37.0 GHz (red) channels.

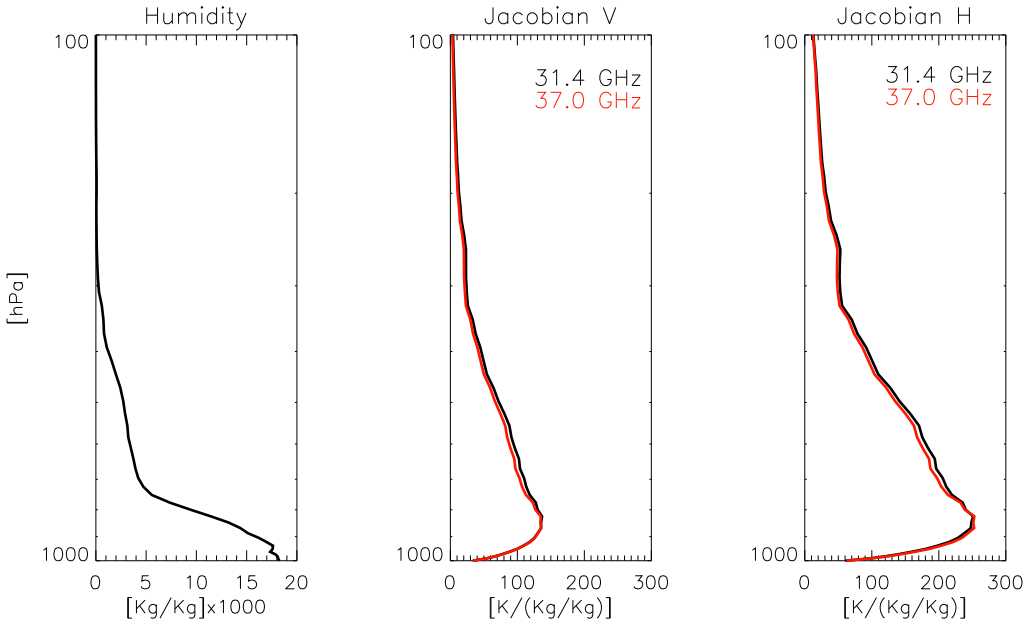

Figure 4.2: The same as Figure 4.1 but for a typical wet atmosphere humidity profile.

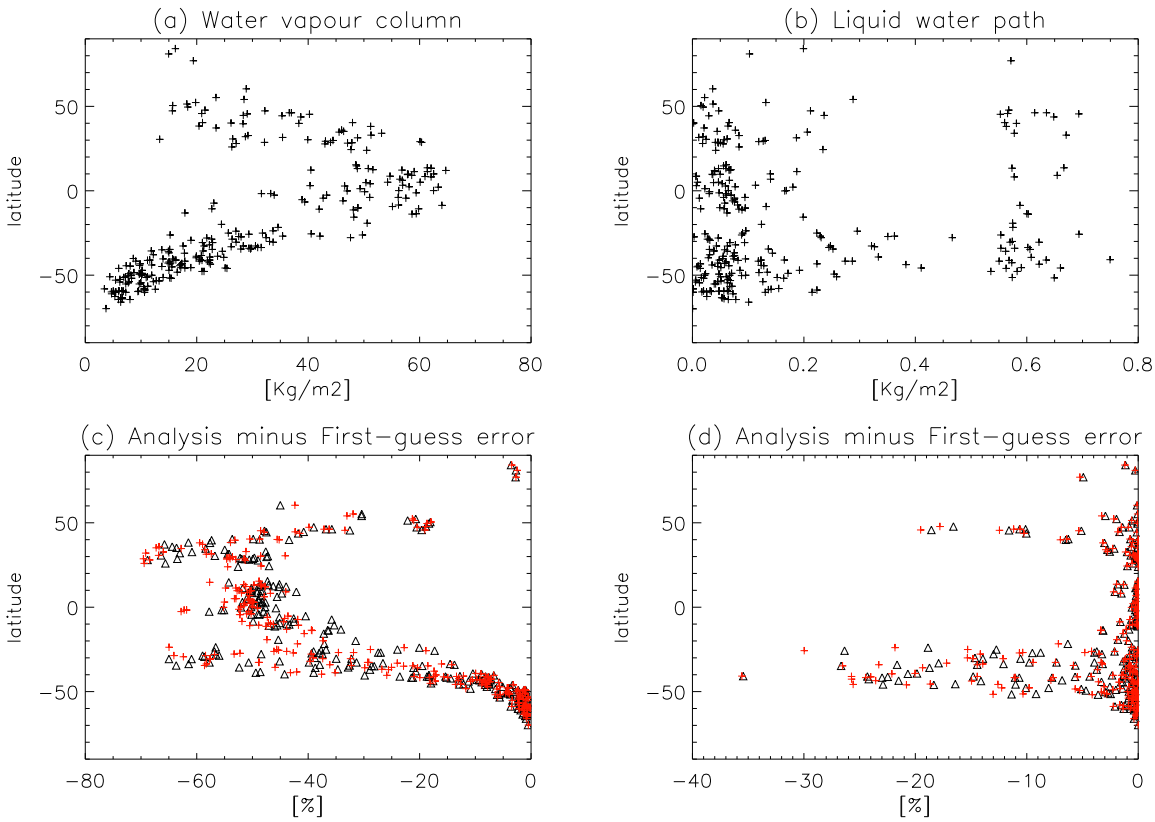

Figure 4.3: The water vapour columns (a) and liquid water path (b) associated with the profiles from the cloudy-sky database. The bottom panels are the corresponding analysis minus first-guess error for the water vapour column (c) and liquid water path (d), expressed as a percentage of the first-guess error and for the 31.4 GHz (black triangle) and 37.0 GHz (red crosses) channels.

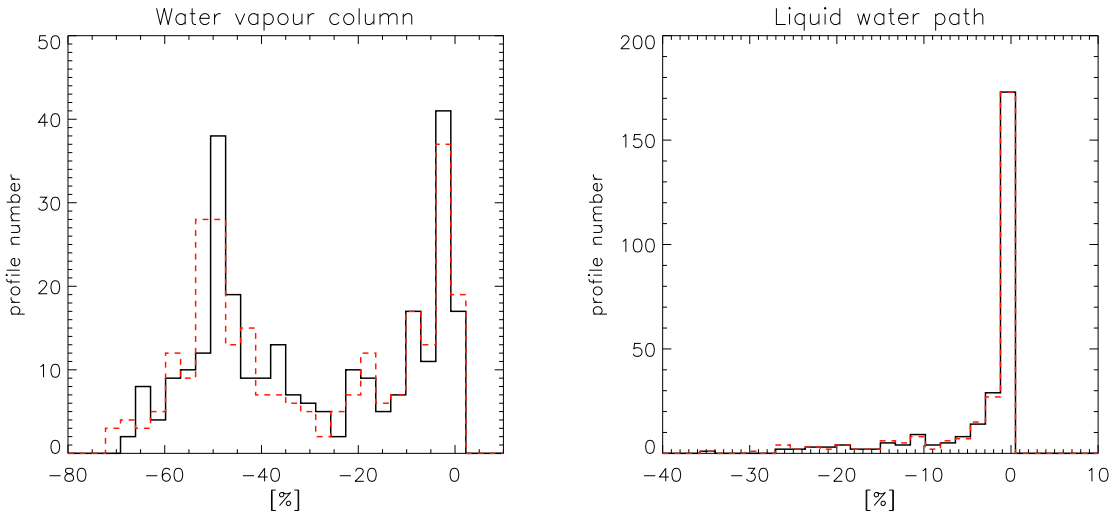

Figure 4.4: Histograms of the analysis minus first-guess error expressed as a percentage of the first-guess error for the cloudy-sky water vapour column (left) and liquid water path (right) and for the 31.4 GHz (black) and 37.0 GHz (red) channels.

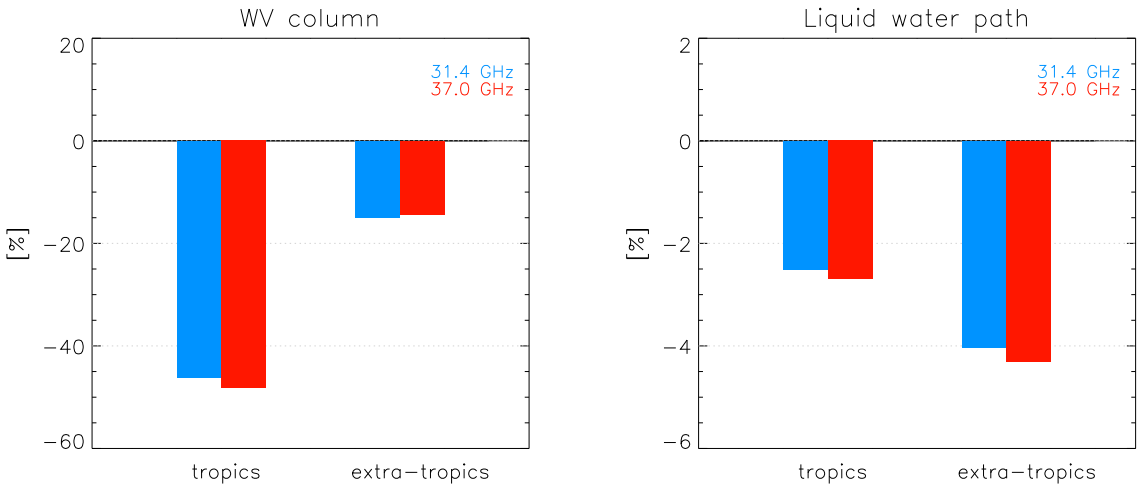

Figure 4.5: The mean analysis minus first-guess error expressed as a percentage of the first-guess error for the clear-sky water vapour column (left) and the liquid water path (right) in the 31.4 GHz (blue) and 37.0 GHz (red) channels.

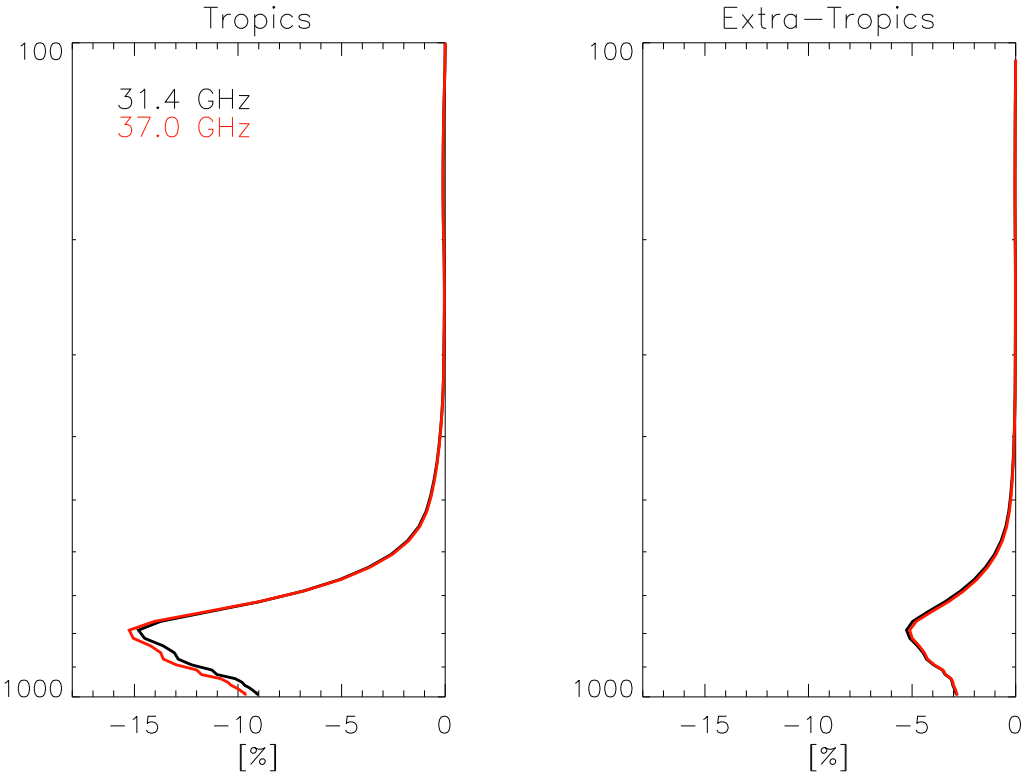

Figure 4.6: The mean analysis minus first-guess error expressed as a percentage of the first-guess error for the cloudy-sky water vapour profiles in the 31.4 GHz (blue) and 37.0 GHz (red) channels.

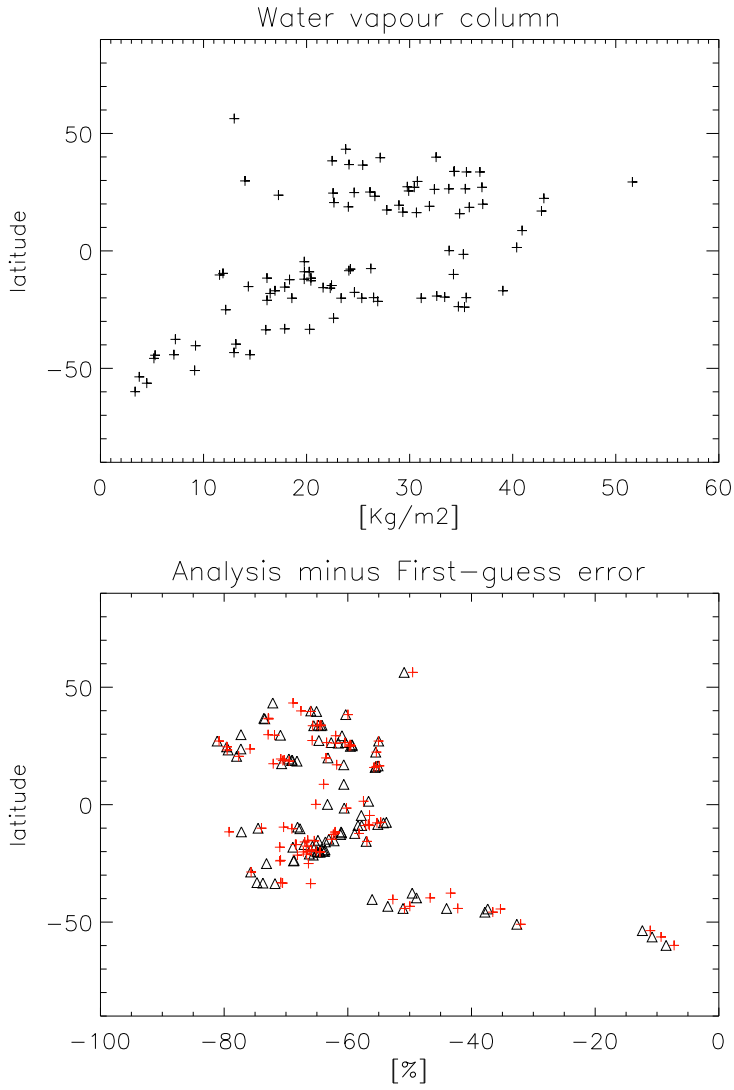

Figure 4.7: The water vapour columns associated with the profiles from the clear-sky database (top panel) and the corresponding analysis minus first-guess error for the water vapour column (bottom panel) expressed as a percentage of the first-guess error for the 31.4 GHz (black triangle) and 37.0 GHz (red crosses) channels.

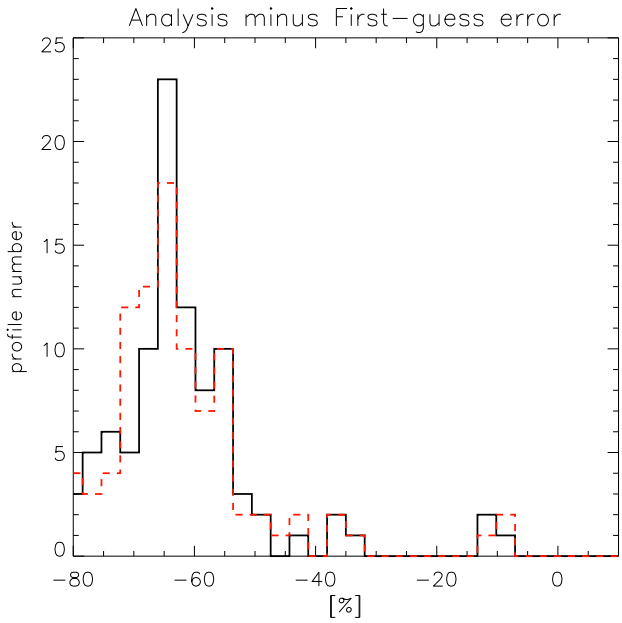

Figure 4.8: Histograms of the analysis minus first-guess error expressed as a percentage of the first-guess error for the clear-sky water vapour column for channels and for the 31.4 GHz (black) and 37.0 GHz (red) channels.

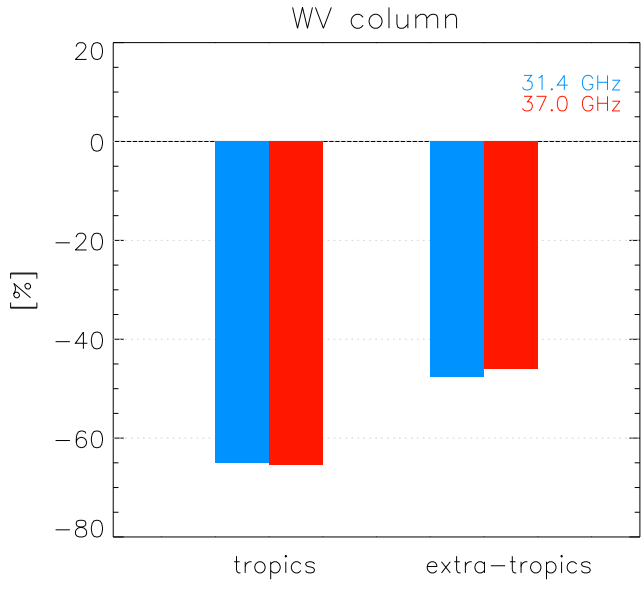

Figure 4.9: The mean analysis minus first-guess error expressed as a percentage of the first-guess error for the clear-sky water vapour column in the 31.4 GHz (blue) and 37.0 GHz (red) channels.

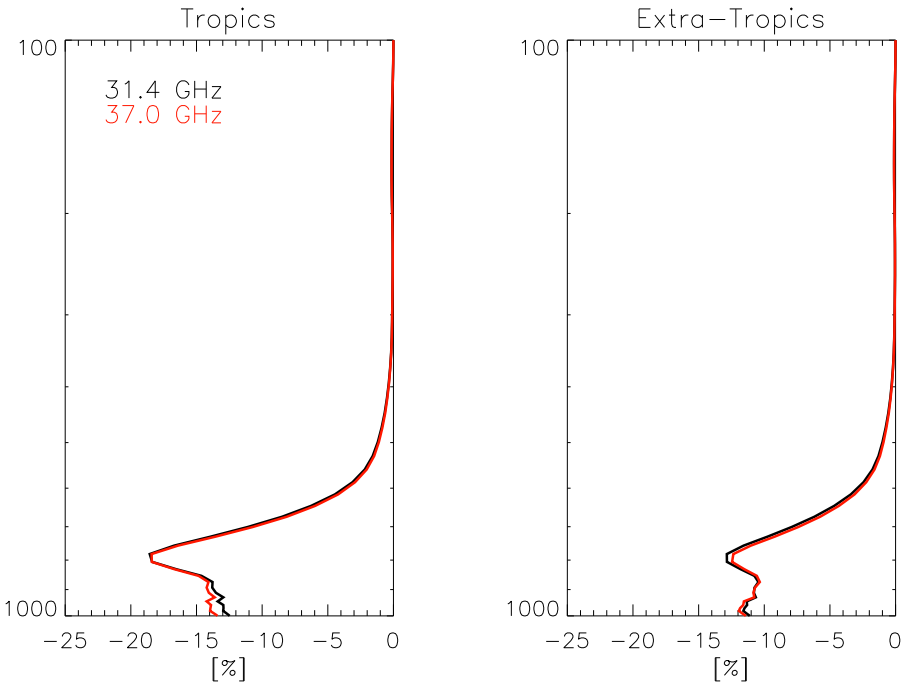

Figure 4.10: The mean analysis minus first-guess error expressed as a percentage of the first-guess error for the clear-sky water vapour profiles in the 31.4 GHz (blue) and 37.0 GHz (red) channels.

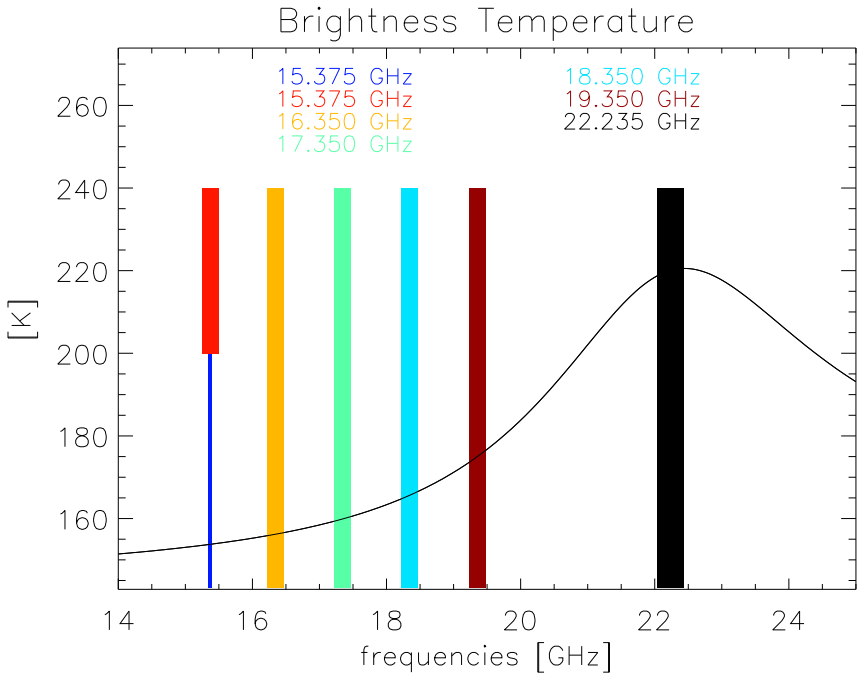

Figure 4.11: The brightness temperature spectrum in the 22 GHz water vapour band for a typical tropical humidity and temperature profile. The frequency bands are the ones under consideration in the present study.

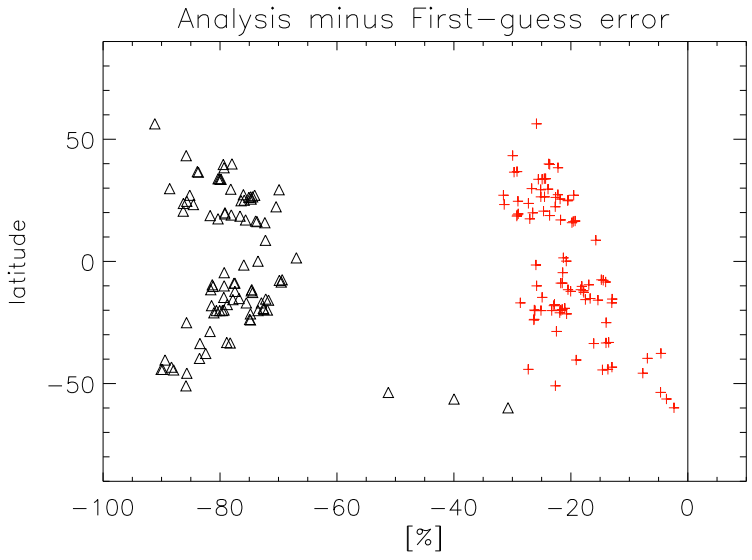

Figure 4.12: Analysis minus first-guess error for the water vapour column expressed as a percentage of the first-guess error for the 22.235 GHz (black triangle) and 15.375 GHz-a (red crosses) channels

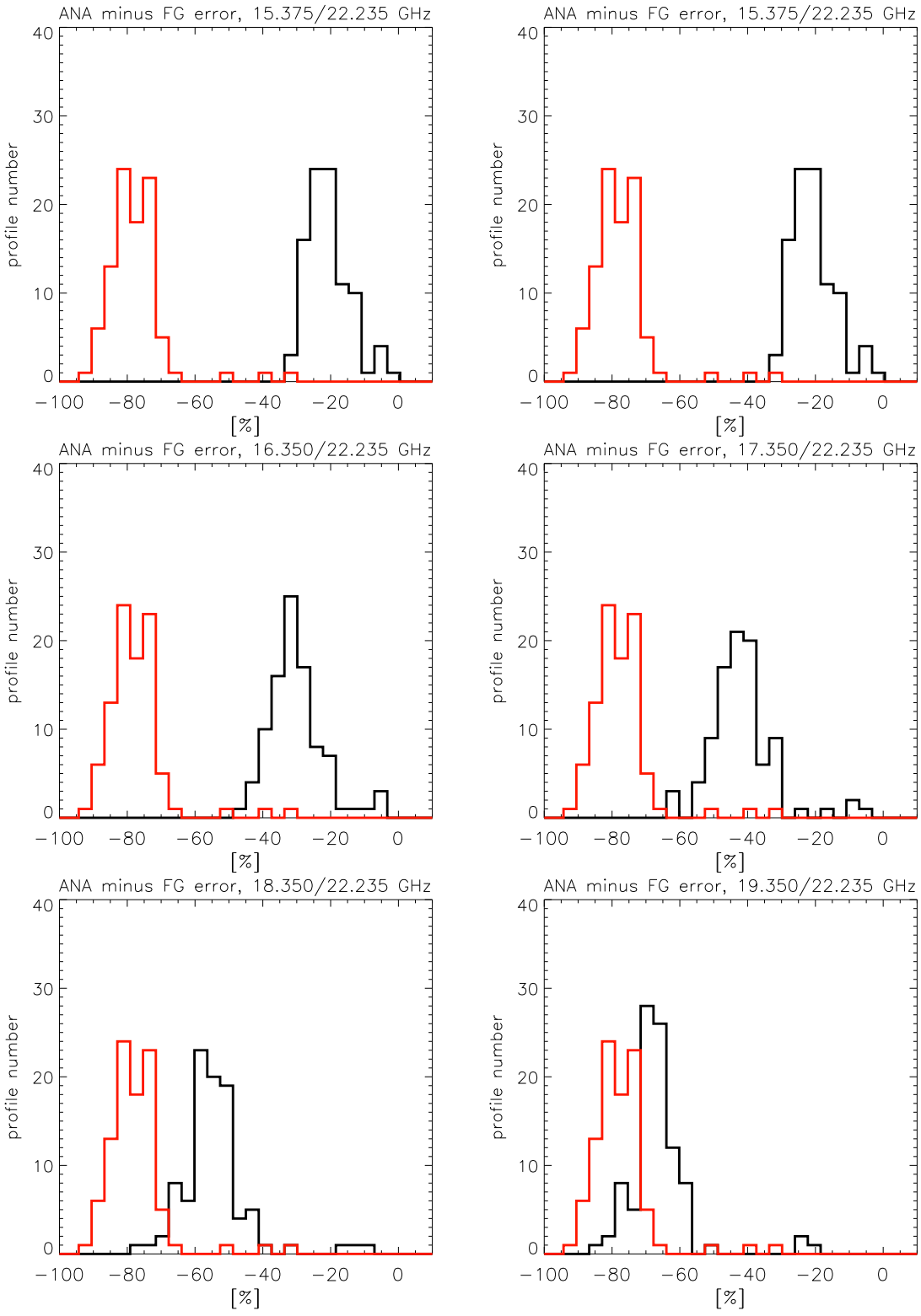

Figure 4.13: Histograms of the analysis minus first-guess error expressed as a percentage of the first-guess error for the clear-sky water vapour column for channels in the15-20 GHz band (see title of the panels) (red) and the 22.235 GHz channel (black).

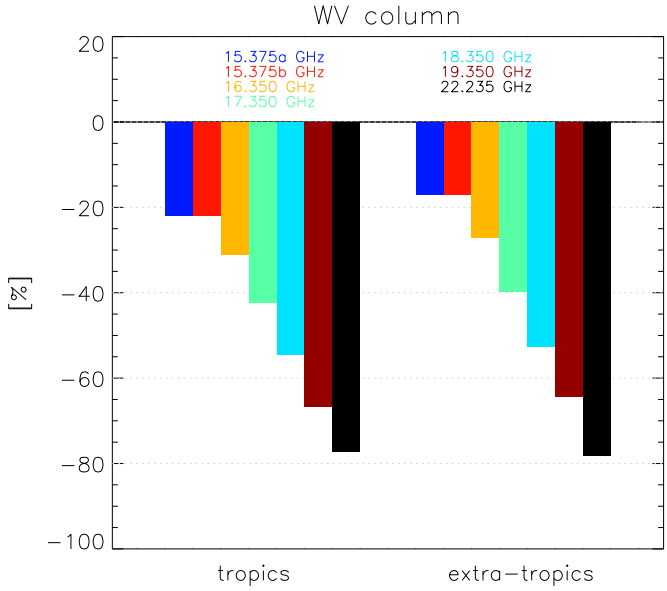

Figure 4.14: The mean analysis minus first-guess error of the the clear-sky water vapour column expressed as a percentage of the first-guess error 15.375a GHz (red) and the 22.235 GHz (black) channels.

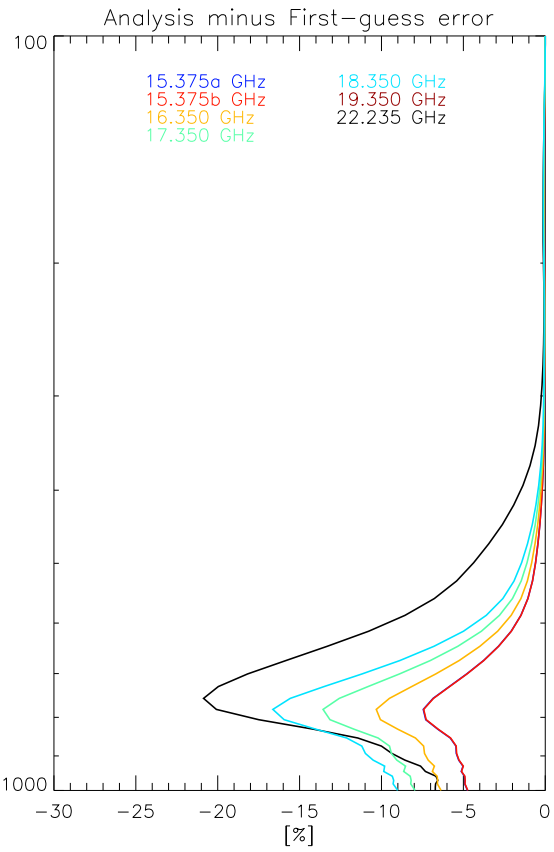

Figure 4.15: The mean analysis minus first-guess error expressed as a percentage of the first-guess error for the clear-sky water vapour profiles in the 15-20 GHz band (see the legend on the plot) and 22.235 GHz channel (black).

5 User requirements on the specification of digital sub-band shapes (WP4200)

5.1 Background and Introduction

The short study reported here forms part of **WP4200** included in the project to accommodate *ad-hoc* investigations required in support of post-EPS pre-Phase-A studies. The study is concerned with an assessment of NWP user requirements on *the shape of digital sub-bands in the 50-60 GHz spectral region* used for temperature sounding on both post-EPS MWS and MWI missions.

The use of digital detection systems has been proposed as an alternative to conventional analog RF filtering used in all heritage microwave sounding and imaging missions to date. In this approach the incoming microwave radiance is mixed with a local oscillator (LO) operating in the 50-60 GHz spectral region to produce a range of intermediate frequencies (IF), covering the frequency range 0-3 GHz (and beyond). In conventional analog detection systems analog filters, with passbands in the range 2-200 MHz, are used to measure the power integrated in a finite range of frequencies which is proportional to the integrated spectral radiance in the scene. In digital detection systems the IF signal, comprising a range of frequencies, is sampled at high frequency *in the time domain* and Fourier transformed to give a regular comb of digital sub-bands. The shape of each digital sub-band, *in the frequency domain*, is governed by the form of any weighting applied to the signal in the time domain.

The process is analogous to the apodisation of interferograms in infra-red interferometry in which weights are applied to the measured interferogram (eg smaller weights are applied to the measured intensities towards the maximum path difference end of the interferogram) in order to suppress side-lobe amplitudes in the frequency domain *instrument response function* (IRF).

The specific question addressed here is :

- Are there specific user requirements on the form (shape) of the digital sub-bands ?
  For example, do the sub-bands have to take a particular form, or is it sufficient to have accurate knowledge of the shape of the response function regardless of the particular form it takes ?

The approach followed is outlined below:

- Determine an optimal reconstruction of analog passbands using digital sub-bands. This entailed an evaluation of:
  1. The brightness temperature errors arising from this reconstruction. This was estimated by computing differences in brightness temperatures for analog bands and those from an optimal linear combination of simulated digital sub-bands using an ensemble of atmospheric states;
  2. The importance of uncertainties in the specification of the exact form of the digital passbands. This required the evaluation of the sensitivity of errors/differences determined in (1) to the form of the digital filter function (*eg.* Boxcar, Hamming *etc.*);
  3. The impact on effective weighting functions of using optimal linear combinations of digital sub-bands.

The working assumption here is that, if digital detection is implemented, then *as a minimum requirement* linear combinations of these sub-bands can be considered as equivalent to heritage analog channels for applications in NWP and climate research.

The construction of the digital sub-bands and the derivation of an optimal linear combination of these to simulate analog passbands is presented in **Section 5.2**. The forward modelling used to simulate measurements is described in **Section 5.3**. Conclusions are drawn in **Section 5.4**. Some suggestions for possible further work are listed in **Section 5.5**.

5.2 Generating digital sub-bands and synthesised analog bands

Several combs of digital sub-bands were generated to cover the spectral range spanned by the MWS temperature sounding channels (MWS3-14, see Table 1). The current MRD specification (MRD, 2010) for the temperature sounding channels of the MWS mission can be broadly divided into two groups: firstly, those having passbands in excess of 100 MHz (MWS 3-9); and secondly those with passbands less than 100 MHz (MWS 11-14). This necessitates different sampling strategies for the tropospheric and lower stratospheric channels *versus* those sounding the mid-stratosphere and above, *i.e.* the very narrow channels require a finer comb of digital sub-bands to reproduce the form of the analog bands.

Channel	Frequency (GHz)	Bandwidth per passband (MHz)
MWS-3	50.3	180
MWS-4	52.8	400
MWS-5	53.596±0.115	2 × 170
MWS-6	54.40±0.081	400
MWS-7	54.94±0.081	400
MWS-8	55.50±0.081	330
MWS-9	57.290344	330
MWS-10	57.290344±0.217	2 × 78
MWS-11	57.290344±0.322±0.048	4 × 36
MWS-12	57.290344±0.322±0.022	4 × 16
MWS-13	57.290344±0.322±0.010	4 × 8
MWS-14	57.290344±0.322±0.0045	4 × 3

Table 1: Channel centre frequencies and bandwidths for MWS channels 3-14 simulated in this study.

The sub-band comb interval ($\Delta\nu$) is governed by the *sampling clock frequency* (ν_{clock}) and the *number of correlator channels* (N_{corr}): 14:

$$\Delta\nu = \nu_{clock}/N_{corr} \tag{14}$$

The comb sampling parameters were provided by ESA and are summarised in Table 2. An additional local oscillator has been introduced at 48.30GHz[1], together with a 512 channel correlator, to cover the lowest frequency sounding channel (MWS3).

Code was developed (in MATLAB) to generate the digital filter functions and determine the optimal combination of these bands to reproduce the analog channels specified in the MRD (MRD, 2010). The main elements of this code are listed here :

- Generate time domain window function

[1]This is a small departure from the ESA guidelines, driven by the design of the MATLAB code, but should not change the results or conclusions significantly

	Band 1 (MWS3)	Band 2 (MWS4-MWS9)	Band 3 (MWS10-MWS14)
Clock Frequency (GHz)	2.89	3.67	1.13
Correlator channels	512	1024	1024
Local Oscillator (GHz)	48.30	52.275	56.70

Table 2: Sampling parameters for digital sub-bands.

- Fourier transform to generate digital sub-band response function
- Synthesise a comb of digital sub-bands, using the parameters specified in Table 2
- Set up a system of linear equations to derive the optimal combination of sub-bands to simulate analog bands
- Perform least squares retrieval of sub-band coefficients
- Generate synthesised analog bands and statistics of the fits to analog bands

Two types of window function were investigated: *boxcar* (giving rise to *sinc* function frequency response) and *Hamming*. The code is easily adapted to generate alternative window functions, but this initial investigation focussed on boxcar and Hamming only as the Hammming window gives rise to significant side-lobe suppression relative to the boxcar function. Additional investigations with other window functions could be carried out, but would not be expected to give rise to significantly different conclusions.

Examples of the synthesised analog bands are shown in Figures 5.1 to 5.6 for MWS channels 6, 10, and 14. For the relatively wide-band channels (MWS3-9) results are similar. Both sinc and Hamming filters give a reasonable representation of the analog band, but with reduced ringing within the passband for the sinc response function. The responses are generally localised within the passband, with greater out of band response for the sinc function response. As a metric of *closeness of fit* the RMS differences for all channels for both sinc and Hamming responses are shown in Figure 5.7. Note that the key issue here is the accuracy of the synthesised passband in *integrating* the scene spectral radiance in the same way as the analog band, and not the accuracy with which the analog passband response can be reproduced. For the narrowest channel (MWS14) the digital sub-bands are generated on a narrower grid with a spacing $\sim$1MHz. The analog bands are of width 3MHz and the *closeness of fit* is poorest for these channels.

5.3 Forward modelling of brightness temperatures and weighting functions

The digital filter synthesised analog bands were sampled on a 100kHz frequency grid and used to forward model brightness temperatures. Brightness temperatures and weighting functions were modelled using both the analog bands and synthetic equivalents for an ensemble of 52 diverse atmospheric profiles using a line-by-line radiative transfer model. Further details of the profile dataset and the radiative transfer modelling are given in section 3.

RMS differences between brightness temperatures computed for the analog and synthesised analog bands, for both boxcar and Hamming window functions are shown in Figure 5.8. For channels MWS4-MWS14 the boxcar window function gives RMS differences of 0.02K or larger. For the most critical channels (MWS5-MWS8) the boxcar window gives differences in the range 0.03K-0.10K. These are

significant differences relative to analog passbands, for both NWP and climate applications. These differences are reduced significantly for Hamming filtering. For all channels the *reduction* in RMS differences is larger than a factor of two. For the most critical channels the difference is an order of magnitude.

Example calculations are shown for MWS6 for boxcar and Hamming windows in Figures 5.9 and 5.10. Calculations for channels 10 and 14 (Hamming window only) are shown in Figures 5.11 and 5.12. Figures 5.11 and 5.12 also show the weighting functions corresponding to the synthesised bands and the analog bands. The differences in weighting functions (analog *versus* synthetic) are generally negligible for all channels for the Hamming window. For the boxcar windowing, the differences are negligible up to channel 11, and gradually become more significant for the higher peaking channels. The weighting function for the boxcar window for channel MWS14 are shown in Figure 5.13.

5.4 Conclusions

Calculations have been performed to synthesise analog passbands from a comb of finely spaced digital sub-bands using digital sampling parameters provided by ESA. These calculations show that both boxcar and Hamming window functions generate sub-bands that can be combined to simulate analog passbands (MWS3-14) with moderate accuracy. The choice of a Hamming window function, giving significant side-lobe attenuation, greatly reduces the *ringing* evident in the passbands simulated with the boxcar window sub-bands. For example, errors in replicating the analog sub-band shape are reduced by a factor of four for the most critical sounding channels (MWS5-MWS8).

For the forward modelling calculations a line-by-line model was used to generate monochromatic brightness temperatures across the spectral region spanned by MWS3-14. Brightness temperatures were integrated over analog bands and their synthetic digital equivalents. RMS differences between the two sets of calculations were 0.02K or above, and as large as 1K for channel MWS14, for the boxcar window function. These differences were greatly reduced, by at least a factor of two and for the most critical channels by an order of magnitude, when Hamming windowing was used. For the Hamming window simulations, the differences (analog *versus* synthetic analog) are less than 0.1K for all channels and for the most critical channels (MWS5-8) in the range 0.002K - 0.01K.

Changes in the weighting functions are negligible for all channels when Hamming windowing is used. For boxcar windowing, small differences appear for channel MWS11 and get progressively larger for higher peaking channels.

In summary, there is clear benefit in using Hamming windowing to improve the localisation of the synthesised passband through side-lobe suppression. This benefit is evident in both the fit of the synthesised passband to the analog band and, more importantly, in the accuracy in reproducing the (integrated) measured brightness temperatures for analog bands.

5.5 Future Work

Possible areas for further work include:

- Optimising the form of the window function to minimise the differences relative to the analog passband simulations.
- Taking account of noise in the analog sub-bands in assessing the differences relative to analog bands.

- Investigate the benefit of using the digital sub-bands in the region of the high peaking channels (MWS13 and MWS14) as independent new channels.

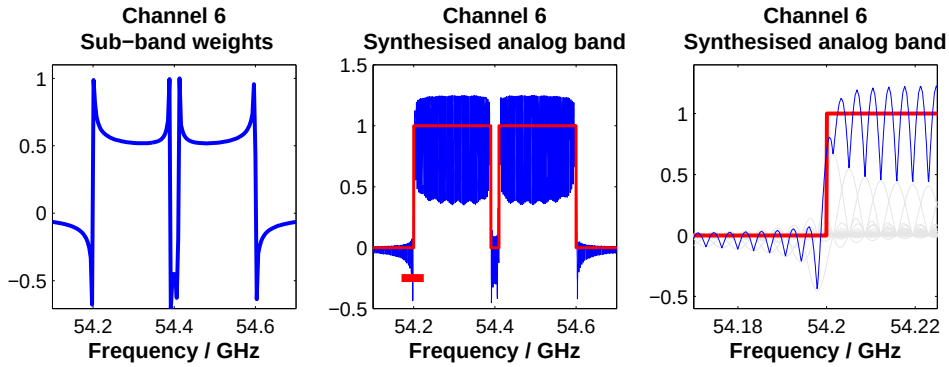

*Figure 5.1: Sub-band weights (***left***) in an optimal linear combination, synthesised digital band in blue with analog passband in red (***centre***) and a zoom of digital sub-bands for MWS-6 over the region highlighted by the red bar in the centre plot (***right***). The light grey lines show the digital sub-bands weighted according to the weights plotted in the left-hand panel.* Boxcar weighting *was used to generate these digital sub-bands, resulting in a* sinc *function frequency response.*

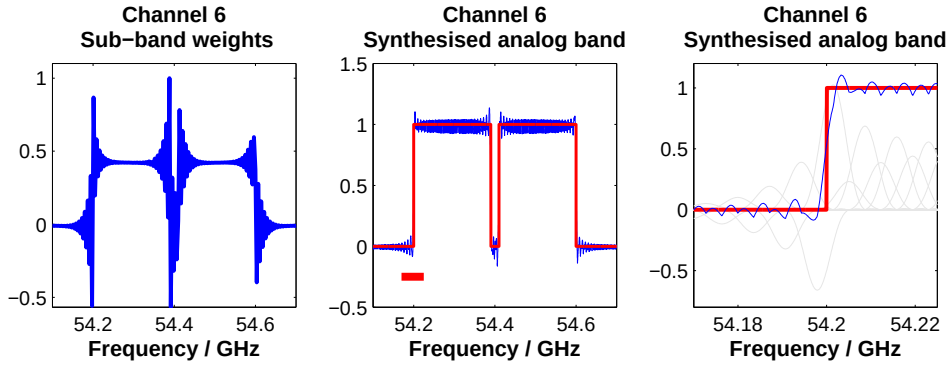

*Figure 5.2: Sub-band weights (***left***) in an optimal linear combination, synthesised digital band in blue with analog passband in red (***centre***) and a zoom of digital sub-bands for MWS-6 over the region highlighted by the red bar in the centre plot (***right***). The light grey lines show the digital sub-bands weighted according to the weights plotted in the left-hand panel.* Hamming weighting *was used to generate these digital sub-bands, resulting in greater side-lob suppression compared to the* sinc *function frequency response shown above in Figure 5.1.*

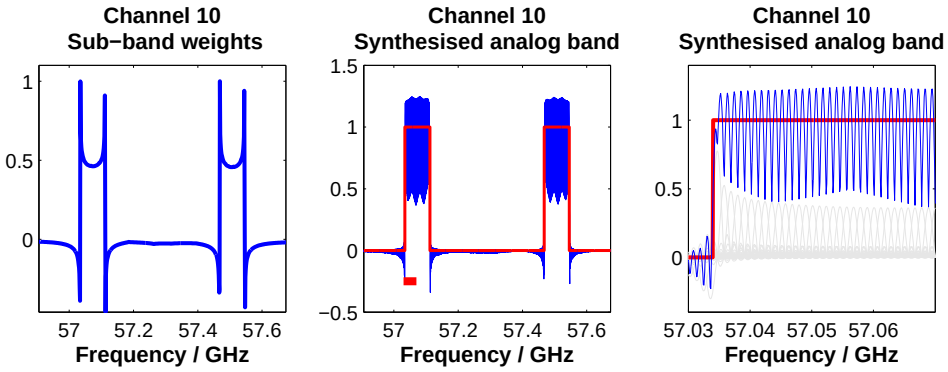

Figure 5.3: As for Figure 5.1 for MWS-10. Boxcar weighting.

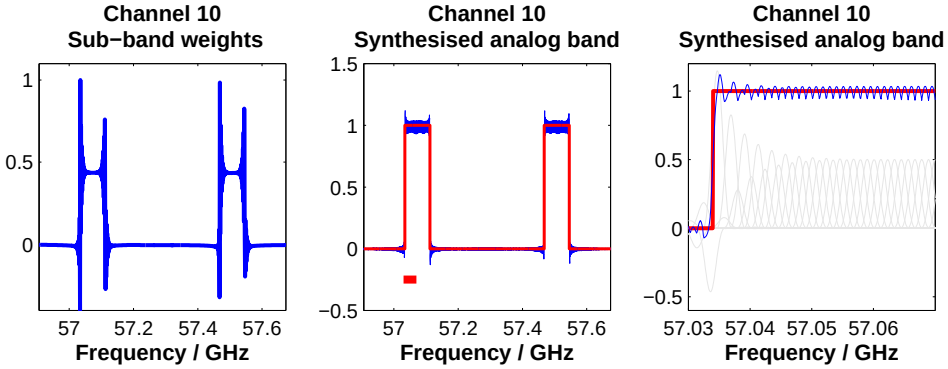

Figure 5.4: As for Figure 5.1 for MWS-10. Hamming weighting.

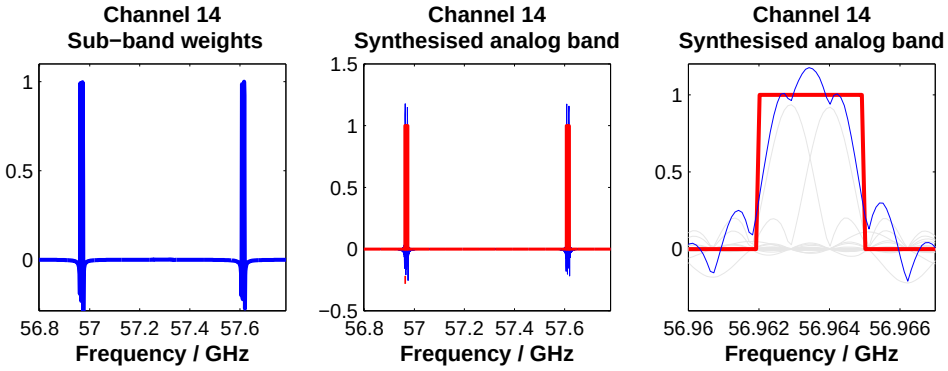

Figure 5.5: As for Figure 5.1 for MWS-14. Boxcar weighting.

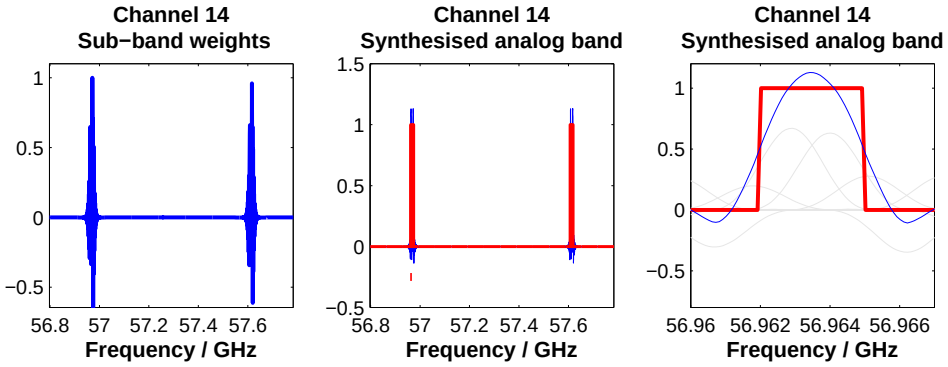

Figure 5.6: As for Figure 5.1 for MWS-14. Hamming weighting.

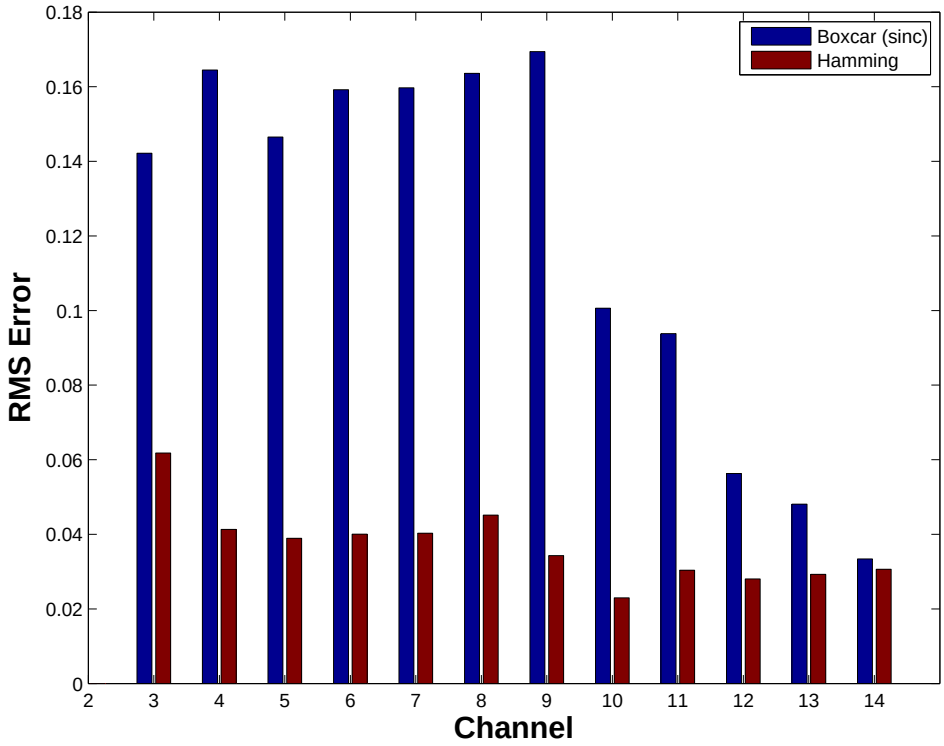

Figure 5.7: RMS difference over passbands. This is calculated as the RMS difference between the normalised analog band and normalised synthesised sub-band over the specified range (passband ± bandwidth). The plot gives an indication of the relative closeness of fit for boxcar versus hamming window functions. Quantitative comparisons between channels are more difficult because of the choice of spectral interval.

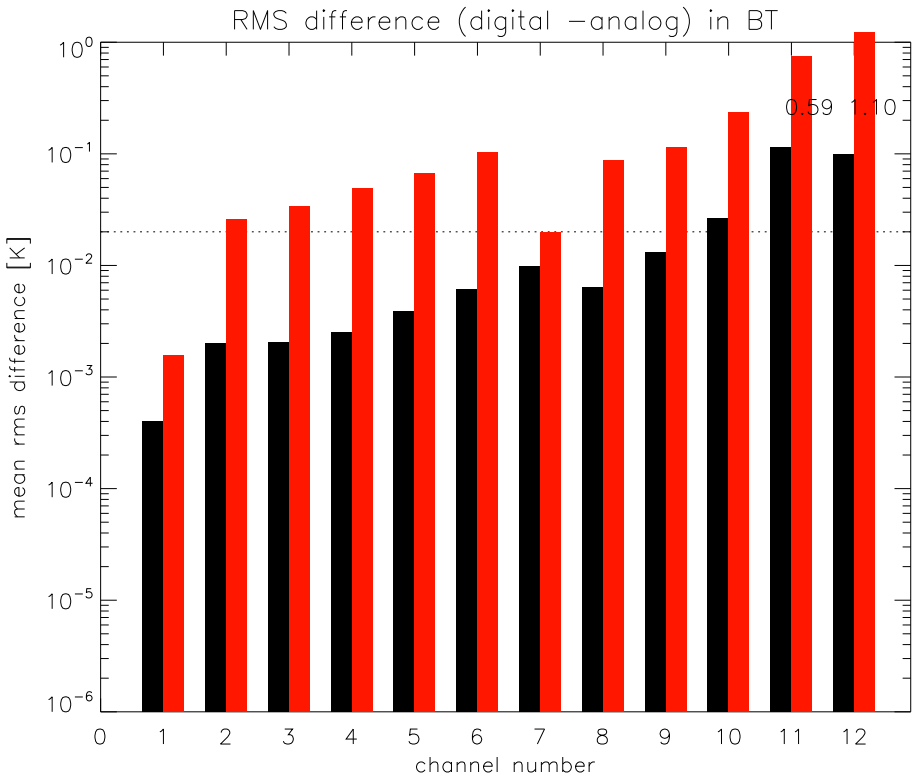

Figure 5.8: RMS Differences in brightness temperatures (analog passband T_B - digital passband T_B) computed for both boxcar (red) and Hamming (black) window functions. The channels are indexed 1(MWS3) to 12 (MWS14).

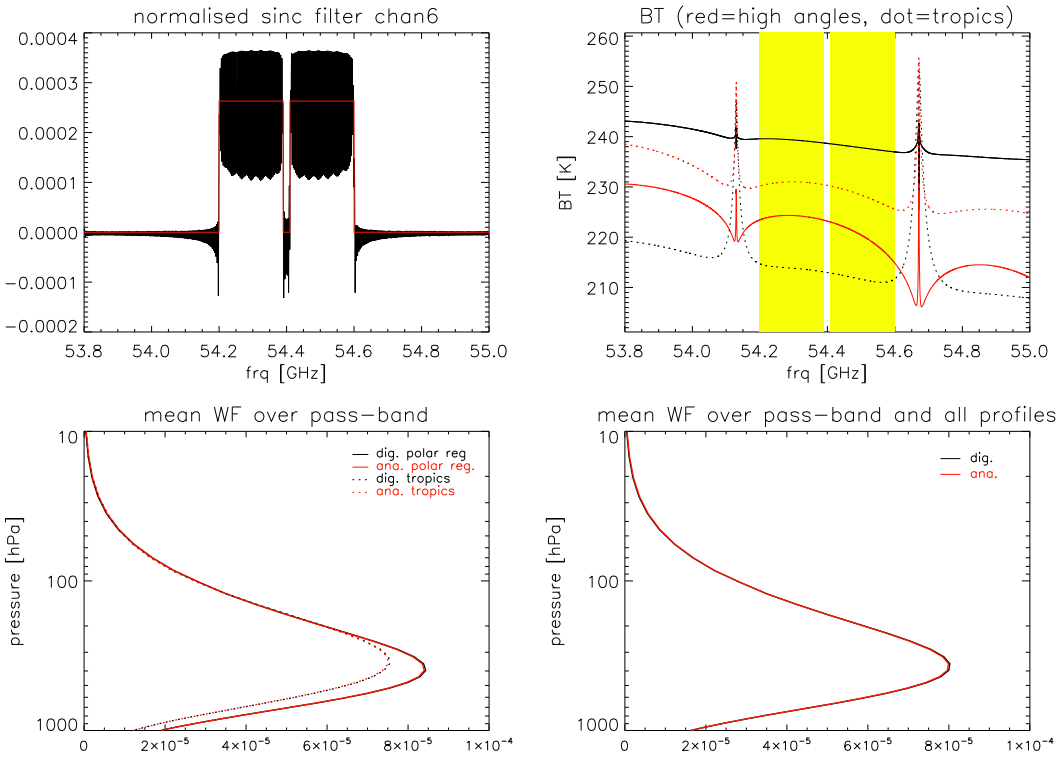

Figure 5.9: **Top left** *shows the analog and synthesised analog passbands for a boxcar (sinc) window function.* **Top right** *shows the position of the passband (***MWS 6***) in relation to the oxygen absorption lines in the range 53.8 - 55.0 GHz. The top-of-atmosphere brightness temperature spectrum is shown.* **Bottom left** *shows the weighting function obtained by averaging monochromatic weighting functions over the analog (red) and synthetic (black) passbands for both tropical and polar atmospheric profiles.* **Bottom right** *shows the mean weighting function obtained by averaging monochromatic weighting functions over all frequencies and profiles in the 52 member diverse profile dataset.*

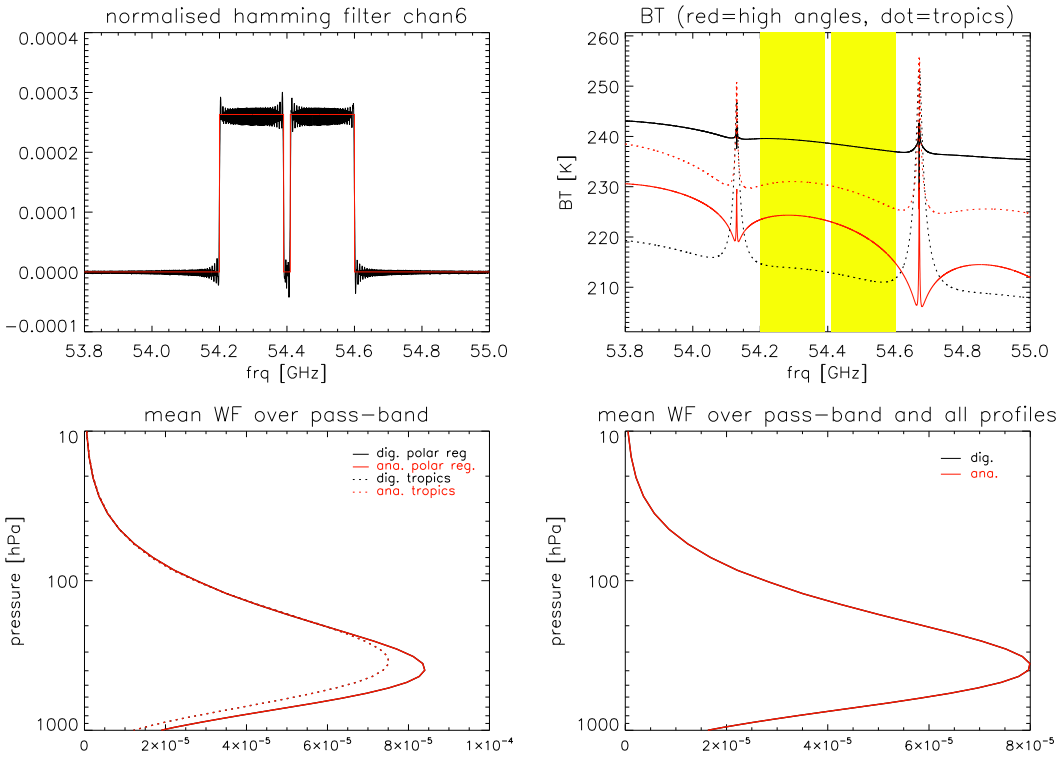

Figure 5.10: As for Figure 5.9 but with Hamming windowing.

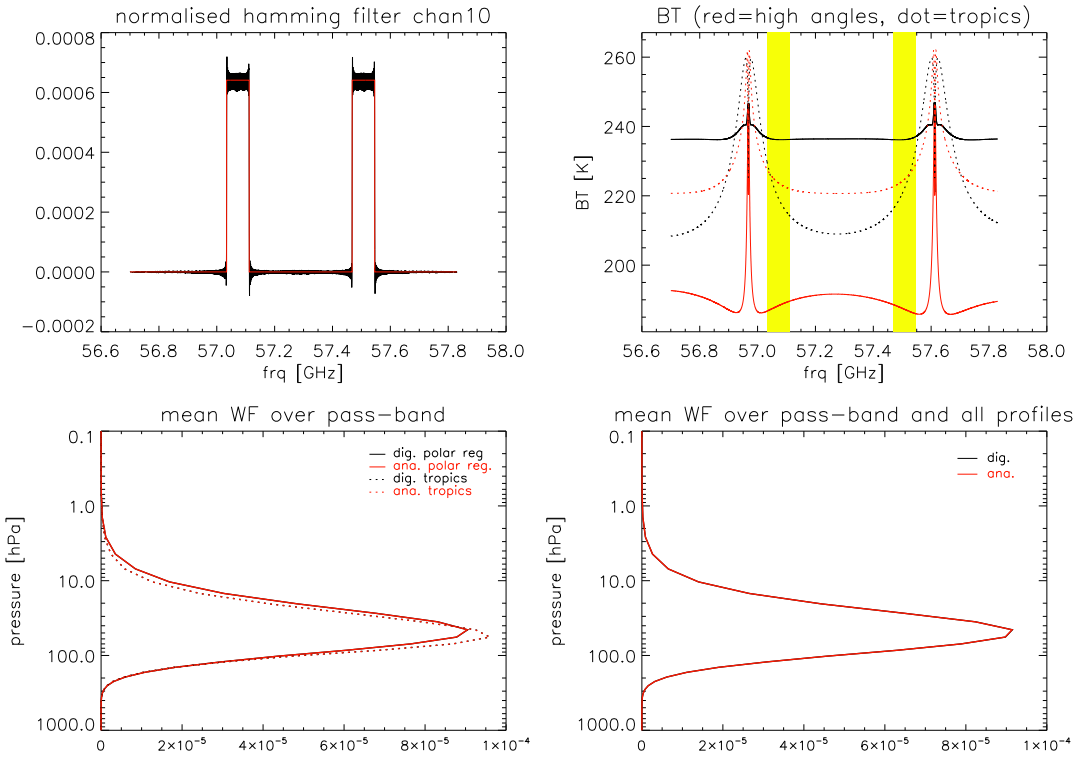

Figure 5.11: As for Figure 5.9 but for channel MWS-10. Hamming windowing.

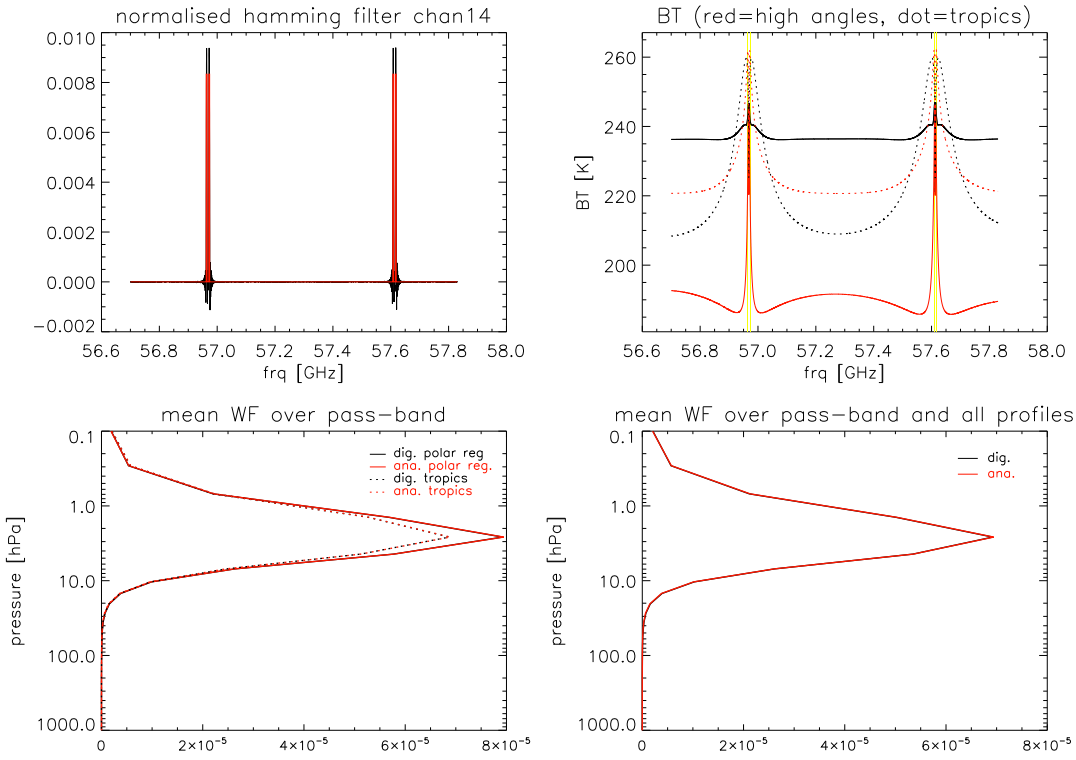

Figure 5.12: As for Figure 5.9 but for channel MWS-14. Hamming windowing.

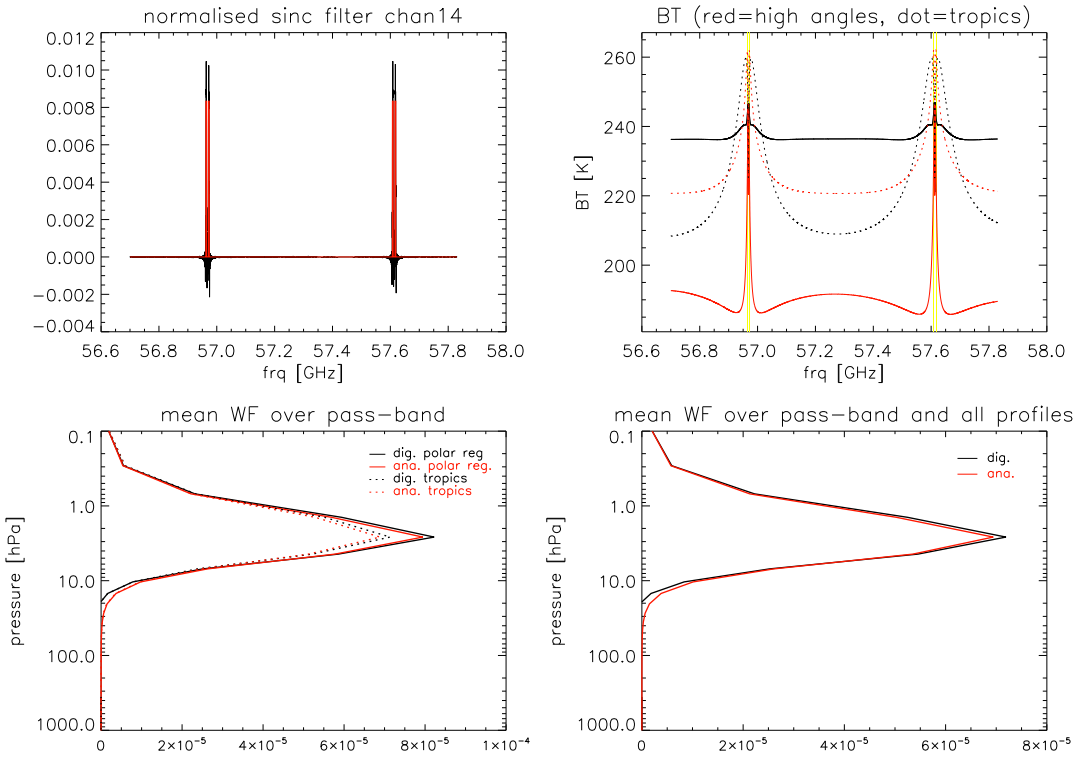

Figure 5.13: As for Figure 5.9 but for channel MWS-14. Boxcar (sinc) windowing.

6 Information content study of optimal resolution and sampling (WP5000)

6.1 Introduction

The following part summarizes the development and testing of a one-dimensional model for the simulation of microwave radiometer imaging for the purpose of optimizing spatial sampling and spatial resolution. The model and optimization strategy is based on linear estimation theory and uses information content in terms of entropy reduction to quantify the information contribution of a sampling/resolution scenario to the observation of geophysical state. The paper describes the set-up of geophysical state and observational modelling and their respective error covariance statistics. Several tests are performed to understand the sensitivity of model performance to the model's linearity, spatial variability and spatial error correlation.

The need for this optimization study stems from the trade-off between spatial sampling / resolution requirements for geophysical parameter observation and technical limitations or cost. Observation requirements can vary strongly, for example, when the observation of spatially smooth structures (temperature, moisture) is compared to that of strongly varying parameters (clouds, precipitation). Technical issues may be the achievable antenna size, rotation rate and integration time. The model developed here can produce one-dimensional geophysical fields with realistic spatial structures and can apply various idealised imaging scenarios to the geophysical fields. The optimization evaluation is based on the information content provided by each scenario.

6.2 Model

6.2.1 Linear estimation theory

The background of the employed models/operators and the calculation of the so-called 'information content' is linear estimation theory (Rodgers 2000, pp238). Here, it is used in the context of the retrieval of geophysical quantities from radiance observations obtained from microwave radiometers. The most important quantities to be derived are temperature and moisture but, with increasing skill of geophysical modeling, also clouds and precipitation. Linear estimation theory is widely used in most operational numerical weather prediction models as part of the data assimilation schemes (Rabier 2005).

The problem of the inversion of observational data from space for deriving information on the atmosphere is not fully constrained, in particular in the presence of clouds and precipitation. The application of statistical principles is therefore fundamental for solving the inverse problem. In the following, the state of the atmosphere (to be retrieved) is denoted as a vector $\mathbf{x}$ and the observations from a microwave radiometer are contained in a vector $\mathbf{y}$. The elements of $\mathbf{y}$ are usually radiance observations at different spectral wavelengths but since we are aiming at solving a spatial problem the elements of $\mathbf{y}$ are single-frequency observations along a radiometer scan.

The statistical link between $\mathbf{x}$ and $\mathbf{y}$ is expressed as conditional pdf's, through the application of Bayes' theorem:

$$P(\mathbf{x}|\mathbf{y}) = \frac{P(\mathbf{y}|\mathbf{x})P(\mathbf{x})}{P(\mathbf{y})} \tag{15}$$

$P(\mathbf{x}|\mathbf{y})$ is the posteriori probability of $\mathbf{x}$ when $\mathbf{y}$ is observed. $P(\mathbf{y}|\mathbf{x})$ is the probability of making observation $\mathbf{y}$ when $\mathbf{x}$ is present, while $P(\mathbf{x})$ and $P(\mathbf{y})$ are the a priori probabilities of $\mathbf{x}$ and $\mathbf{y}$, respectively. $P(\mathbf{x})$ is assumed to fully describe the a priori distribution of $\mathbf{x}$.

The physical link between $\mathbf{x}$ and $\mathbf{y}$ is described by the observation operator, H, that may be non-linear but should not deviate from non-linearity too strongly to not violate the chosen linear estimation framework. In our case, the observation operator only consists of an imaging function that integrates a high-resolution geophysical field over the finite instantaneous field of view of a radiometer. This mapping is always linear. Later, an additional mapping function will be added to account for non-linearities as they would be introduced by a radiative transfer model that relates the original geophysical field to radiances observed at the top of the atmosphere.

The modelled observation, $\mathbf{y}$, is then:

$$\mathbf{y} = H(\mathbf{x}) + \varepsilon \tag{16}$$

and ε summarizes observation errors (e.g. radiometer noise) and forward modeling errors (e.g. radiative transfer model uncertainties).

The estimation of $P(\mathbf{x}|\mathbf{y})$ is determined by the observations and an a priori estimate of the state, $\mathbf{x}_b$, as well as the error covariance matrices of that a priori state, $\mathbf{B}$, and the errors originating from observation and modelling, $\mathbf{R} = \mathbf{E} + \mathbf{F}$:

$$P(\mathbf{x}|\mathbf{y}) = exp\{-\frac{1}{2}[\mathbf{y} - H(\mathbf{x})]^T \mathbf{R}^{-1}[\mathbf{y} - H(\mathbf{x})] - \frac{1}{2}[\mathbf{x} - \mathbf{x}_b]^T \mathbf{B}^{-1}[\mathbf{x} - \mathbf{x}_b]\} \tag{17}$$

Superscripts '-1' and 'T' denote inverse and transpose matrices, respectively. Eq. 17 only holds if the distributions $\mathbf{y} - H(\mathbf{x})$ and $\mathbf{x} - \mathbf{x}_b$ are uncorrelated as well as $\mathbf{B}$ and $\mathbf{R}$ have Gaussian characteristics and zero means.

In the linear case the optimal analysis state $\mathbf{x}_a$ has the following expression:

$$\mathbf{x}_a = \mathbf{x}_b + \mathbf{A}\mathbf{H}^\mathbf{T}\mathbf{R}^{-\mathbf{1}}[\mathbf{y} - H(\mathbf{x_b})] \tag{18}$$

with $\mathbf{H}$ and $\mathbf{H}^T$ being the tangent-linear and adjoint of the observation operator, and $\mathbf{A}$ the analysis error covariance matrix:

$$\mathbf{A} = \mathbf{B} - \mathbf{B}\mathbf{H}^\mathbf{T}(\mathbf{H}\mathbf{B}\mathbf{H}^\mathbf{T} + \mathbf{R})^{-\mathbf{1}}\mathbf{H}\mathbf{B} \tag{19}$$

6.2.2 Information content

The information content estimation relies on the estimation of the additional contribution to retrieval accuracy provided by the observation given the a priori information. It is therefore a quantitative measure of the reduction of the estimation error when the observation is available. The improvement of estimation error depends on the sensitivity of the observation to the state and on the accuracy of the measurement and modelling, *i.e.*, on $\mathbf{H}$ and $\mathbf{R}$, and finally on the accuracy of the a priori information (through $\mathbf{B}$). This makes the information content quantity similar to the signal-to-noise ratio. The same methodology has been used for the selection of radiometer channels in the infrared (Rabier et al. 2002) and microwave (Lipton 2003, Di Michele and Bauer 2006).

Historically, there have been several formulations of information content (Rodgers 2000 and references therein), namely the 'degrees of freedom for signal', DFS, and the 'entropy reduction', ER. The former estimates the number of independent pieces of information in a measurement vector that are related to the signal vs. those that are related to the noise. The latter calculates the probability of solutions in terms of entropy that has a maximum when all states have equal probability and that has a minimum if all states except one have zero probabilities. DFS is defined as the expectation value of the normalized difference between analysis state, $\mathbf{x}_a$, and a priori state:

$$DFS = \varepsilon\{(\mathbf{x}_a - \mathbf{x}_b)^T \mathbf{B}^{-1}(\mathbf{x}_a - \mathbf{x}_b)\} = tr[\mathbf{I} - \mathbf{A}\mathbf{B}^{-1}] \tag{20}$$

The entropy reduction is defined as the difference between the entropy of $P(\mathbf{x})$ and the one of the posteriori probability $P(\mathbf{x}|\mathbf{y})$:

$$ER = S[P(\mathbf{x})] - S[P(\mathbf{x}|\mathbf{y})] = \frac{1}{2} log_2 \left(\frac{|\mathbf{B}|}{|\mathbf{A}|} \right) \tag{21}$$

where $|\ |$ indicates the determinant operator. The *log* with basis '2' is usually chosen for expressing ER in units of bits.

The actual procedure entails the normalization of the Jacobian matrix by the observation plus modeling error covariance matrix:

$$\mathbf{H}' = \mathbf{R}^{-1/2}\mathbf{H} \tag{22}$$

This unifies geophysical units and quantifies how different the operator's sensitivity is from its assumed errors. The contribution of a single observation (along the scan) to a change in the error covariance is:

$$\mathbf{A}^{-1} = \mathbf{B}^{-1} + \mathbf{h}'\mathbf{h}'^{T} \tag{23}$$

where $\mathbf{h}'$ is a vector of $\mathbf{H}'$ that contains the sensitivity of the observation in one field of view to changes of the state vector along the entire scan. Following the algebra as described by Rabier et al. (2002), Eq. 21 becomes:

$$ER = \frac{1}{2} log_2 (1 + \mathbf{h}'^{T}\mathbf{B}\mathbf{h}') \tag{24}$$

Here, Eq. 24 is applied to each scan position and averaged over the scan. This can be repeated for as many scan sample as are necessary to create robust statistics.

6.2.3 Definition of model terms

The model comprises different components that relate to the geophysical state and the observation modeling. It is obvious that shortcomings in their definition may greatly affect the results. Whenever possible, different choices were trialled and potential for misinterpretation discussed. The highest resolution, *i.e.* the resolution at which the 'true' variability is modelled, is 1 km and a scan-width of 600 km is assumed. for the case studies in Section 6.3.1 and 900 km for the calculation of mean results in Section 6.3.2. The latter is in the range of low-Earth orbiting instruments such as SSM/I (1500 km), AMSR-E (1450 km) and TMI (720 km). The former has been chosen to simplify visualisation.

The toy-model is one-dimensional and does not represent cross-track vs. along-track imaging. Further, the geophysical field to be observed is not simulated based on a physical but a simple statistical model. All observations across the one-dimensional field are assumed to have the same properties in terms of spatial sampling/resolution as well as response to geophysical variations (as a single radiometric channel).

In the case studies. the geophysical model is applied at the full resolution while for the case studies the observation operator is applied at 30 positions along the scan that are separated by a sampling distance of 20 km. For the global statistics the sampling distance has been varied along with the beam-width and thus the number of samples varies as well. The observation operator integrates over the geophysical parameter distribution using the antenna gain function as a spatial weighting function, in addition to a mapping function that could be a radiative transfer model, for example. In the following, the toy-model and its components are described:

Geophysical state x: The optimization of sampling/resolution is mainly an issue for geophysical fields with high spatial variability and much less of an issue for smooth structures that are associated with the spatial distribution of, e.g., temperature and moisture. In current global NWP systems, the latter are sampled rather generously at 100 km, which is well above the sampling distance provided by the employed radiometers. For clouds and precipitation, and in particular in convective cases, the situation changes.

It is estimated that typical decorrelation lengths of convective precipitation are below 10 km (Moreau et al. 2009) so that spatial sampling should be at least a factor of two higher to properly sample convective rainfall variability. Our 'geophysical model' assumes a number of 10 randomly distributed precipitation events (N) across the scan (with locations, z_i, along x-axis) whose intensities, A_j, are also randomly varied between 0 and 10:

$$x(z_i) = \sum_{k=1}^{N} A_j exp(-|z_i - z_k|/z_s), A_j \in [0,10] \tag{25}$$

At location z_i, $x(z_i)$ is the sum of the contributions from all events given their respective intensities, A_k, at their specific locations, z_k, accounting for the spatial decorrelation of event z_k. The spatial correlation of precipitation is accounted for by an exponential reduction of the peak intensity away from the peak's location $(z_i - z_k)$ with a scaling width of z_s. This width can be varied to represent more variable or smoother structures. While this model does not include any physical parameterization, it nonetheless produces spatial statistics that are similar to those of convective precipitation. Figure 6.1a shows an example of **x** with 10 events along the x-axis (=scan) of varying intensity and the overlap between neighbouring events assuming z_s = 2 km.

Error covariance matrix of geophysical state B: Since the information content evaluates the information gain introduced by an observation to improve on the a priori knowledge expressed by the background error statistics (see Eq. 21), the definition of **B** is very important. In NWP, the formulation of **B** for clouds and precipitation is very difficult and has not yet been generalized for operational applications. Therefore, we make the assumption that background errors are larger where precipitation occurs and that the spatial correlation represented in **B** follows the spatial correlation of precipitation (*i.e.* $x(z_i)$) itself:

$$B(z_i, z_j) = 1/4 \sum_{k=1}^{N} x(z_i)x(z_j)exp(-|z_i - z_k|/z_s)exp(-|z_j - z_k|/z_s) \tag{26}$$

The error standard deviation equals therefore half the precipitation intensity.

Observation operator H and sensitivity H: The observation operator consists of two parts, namely the spatial weighting prescribed by the antenna gain function and, if desired, a mapping function that translates between the model's geophysical state and the observable **y**, for example a radiative transfer model. The latter would be important if the link between the geophysical state and the observable is non-linear. Non-linearity also means that the transfer from **x** to **y** becomes state dependent. Note that in our case the observation **y** is obtained from simulations, *i.e.* $\mathbf{y} = H(\mathbf{x})$.

The first element of H is the antenna gain function, g, that is assumed to be of Gaussian shape *i.e.*:

$$g(z) = \frac{1}{\sqrt{2\pi\sigma}} exp(-z^2/2\sigma^2) \tag{27}$$

where σ is the half-width of the Gaussian distribution. The term 'half-width' relates to the half-power beamwidth, i.e. where $g(z)/g(z=0) = 0.5$ and therefore $10log_{10}(g(z)/g(z=0)) = -3dB$.

Note that if the integration of $g(z)$ is performed over the 3dB beamwidth (=1.2 σ), only 75% of the total energy is represented. If the integration limits are 1, 2 or 3σ the total energy is 70, 95 and 100%, respectively. The choice of integration limits is therefore important and affects the sensitivity of a single beam to changes in the geophysical state vector in the wings of the beam and it also affects the magnitude of the correlation between neighbouring beams that is obviously smaller if the integration is performed with narrower limits. Due to the assumption of ideal Gaussian gain function shapes, side-lobe effects are not included.

In the case studies presented in Section 6.3.1, g is applied to $\mathbf{x}$ over an interval of $\pm 3\sigma$ to represent the entire energy inside the beam. Both 3 $\pm 1.2\sigma$ (3 dB) and $\pm 3\sigma$ limits have been tested and a significant sensitivity of the results to integration limits was found (not shown here). In all cases, the integral is normalized to unity to ensure that different options of σ produce the same total spatial integration. Location and shape of radiometer fields of view (g) are illustrated in Figure 6.1b for three different gain function half widths, namely 10, 20 and 50 km (black, dark blue, light blue). Since the area under each curve is normalized to unity, the amplitudes vary with half width size.

For obtaining $\mathbf{y}$ two further options were defined: (1) no mapping function is applied, *i.e.* the observation operator is linear, *i.e.*, $\mathbf{y} = g\mathbf{x}$ and $\mathbf{H} = d\mathbf{y}/d\mathbf{x} = g$; (2) a mapping function that equals the state is applied with $\mathbf{y} = g\mathbf{x}^2$ and $\mathbf{H} = 2g\mathbf{x}$ and that thus introduces weak non-linearity. The linear case is shown in Figure 6.1c for the three beam-width options. Clearly, the effect of footprint location and gain function width is demonstrated yielding the largest dynamic range for the narrowest fields of view. The Jacobians for the linear case are shown in Figure 6.1d. As stated, they reproduce the gain functions and are, in fact, independent of state. $\mathbf{H}$ is calculated from finite differences with a 1% perturbation of state $\mathbf{x}$.

Error covariance matrix of observation operator R: As for $\mathbf{B}$, the definition of $\mathbf{R}$ is difficult but does not have to involve a great deal of physical modeling. It is assumed that all observations (fields of view) have the same instrument noise (0.5 K in brightness temperature) and that inter-observation correlation is simply a function of spatial overlap between neighbouring fields of view:

$$R(z_m, z_n) = 0.25K^2 \sum_{i=1}^{N} g'(z_i - z_m) g'(z_i - z_n) \tag{28}$$

The gain function g' is as g but normalized to unity at the maximum of the distribution function to ensure unity auto-correlation. The indices 'm' and 'n' denote the fields of view. It is important to note that this correlation will greatly affect the trade-off between sampling and resolution and the options of correlated and uncorrelated observation errors have been tested.

6.3 Results

6.3.1 Case studies

The following cases illustrate the model performance as a function of three different gain function half widths, namely 10, 20 and 50 km. The domain size is 600 km over which 600 values for $\mathbf{x}$ are generated and, for 10 fields of view and a fixed spatial sampling of 20 km, the dimension of $\mathbf{y}$ is therefore 10. $\mathbf{B}$ is a 600x600, $\mathbf{R}$ is a 10x10 and $\mathbf{H}$ is a 10x600 matrix, respectively. The inversion of $\mathbf{R}$ is carried out by a singular value decomposition. Both variable and smooth fields have been generated with z_s = 2 and 20 km. the following figures only show one realisation for demonstration purposes while Table 1 shows the mean ER for each option and 3 realisations. Later, statistics for larger case samples are produced (see Section 6.3.2).

Table 1: 3 examples of mean ER for various combinations of antenna gain function half width and a sampling distance of 20 km for cases of spatially variable geophysical fields with $z_s = 2km$ and $z_s = 20km$.

	Variable field, z_s = 2 km 3dB beam-width (km):			Smooth field, z_s = 20 km 3dB beam-width (km):		
	10.0	20.0	50.0	10.0	20.0	50.0
Linear, **R** *diagonal*						
Case 1:	0.32	0.53	0.54	2.89	2.92	3.00
Case 2:	0.41	0.49	0.57	2.91	2.93	3.04
Case 3:	0.35	0.42	0.44	2.35	2.36	2.41
Non-linear, **R** *diagonal*						
Case 1:	0.65	1.35	1.72	5.11	5.19	5.51
Case 2:	0.87	1.21	1.86	5.13	5.21	5.62
Case 3:	0.65	1.00	1.36	4.14	4.19	4.43
Linear, **R** *non-diagonal*						
Case 1:	0.54	1.43	1.02	3.82	3.27	3.05
Case 2:	0.60	2.16	1.23	3.86	3.29	3.17
Case 3:	0.55	2.13	0.67	3.11	3.50	2.48
Non-linear, **R** *non-diagonal*						
Case 1:	0.90	4.41	3.54	6.02	7.43	7.13
Case 2:	1.06	5.75	3.96	6.09	7.82	7.70
Case 3:	0.86	5.05	3.13	4.88	7.76	6.45

Linear vs. non-linear y: The first test demonstrates the sensitivity of the information content calculation to the linearity of **y**. The left and right panels in Figure 6.2 show the application of $\mathbf{y} = g\mathbf{x}$ or $\mathbf{y} = g\mathbf{x}^2$ keeping all other parameters the same. The non-linear operator produces a similar mapping of **x** into **y** in relative terms but with different absolute magnitudes of **y** between beam-width options (Fig. 6.2c left vs. right). The most obvious difference is exhibited by **H** (Fig. 6.2d left vs. right). The state dependence in the non-linear case is rather obvious and mainly affects the lower spatial resolution versions of *ER*.

Mean *ER* becomes larger for non-linear relationships between **x** and **y** (see Table 1) since sensitivity of changes in **y** to changes in **x** increases. In both cases and for z_s = 2 km the 20 km beam-width option is clearly the best as it matches the sampling distance of 20 km.

Variable vs. smooth x: With smoother structures (Figure 6.3) the difference between the individual choices of gain function half widths becomes smaller, as expected. The three realisations of **y** are very similar (Figure 6.3c, right panel) and thus the dynamic range of *ER* along the scan is greatly reduced. Mean values of *ER* are within a 10-20% range. In the linear case, the 20 km beam-width produces the highest mean *ER* for z_s = 2 km while for z_s = 20 km the 10 km beam-width is best. The latter is explained by the fact that with smoother fields the beam-width differences affect *ER* generally less but the narrowest beams pick the largest *ER*s near the peaks of **x** thus producing the largest mean *ER*. This demonstrates what has been stated in the Introduction, namely the less critical choice of sampling when smooth temperature and moisture structures are observed, as is in practice for temperature and moisture in NWP.

Diagonal vs. non-diagonal R: In case of a diagonal **R**, the individual fields of view will become statistically independent in terms of their errors which should enhance the information content for the wider spatial gain functions relative to the more narrow ones. This is confirmed by the test shown in Figure 6.4 where **x**, **y** and **H** are identical between both panel columns but for the diagonal **R** the *ER* patterns are much more similar to the **y** patterns. The difference between the mean *ER* for the different gain function width options in Table 1 reduces, and due to the spatial independence of the samples for a diagonal **R** the widest field of view option produces the highest information.

6.3.2 Large samples

The above model has been run for 100 realizations of **x** in the configuration of high (z_s = 5 km) and low (z_s = 50 km) spatial variability. These z_s-choices are different from those presented in Section 6.3.1, which were defined for demonstration purposes only. Estimates of true rainfall variability and spatial (and temporal) decorrelation vary substantially, also due to the choice of observational data, for example, gauges, ground-based radar or satellite observations. Since radar data produces the most consistent estimate of spatial rainfall distribution at high resolution it was decided to follow the study of Moreau et al. (2005) and assume a spatial decorrelation scale of about 5-8 km for convective precipitation. On the opposite side of the scale, 50 km was chosen that resembles large-scale precipitation events generally associated with smaller intensities.

100 cases for sampling distance options of 5, 10, 15, 20, 25, 30, 50 km and half-beam widths of 5, 10, 15, 20, 25, 30, 35, 40, 45, 50 km were calculated, again for all combinations of linear and non-linear models, diagonal and non-diagonal **R** and z_s of 5 and 50 km. Figure 6.5 shows the linear model / diagonal **R** results for variable and smooth fields.

In case of variable fields (Figure 6.5a) the areas of maximum information content align rather well with the 1:1 line suggesting that in case of heterogeneous fields the best approach is a contiguous sampling where sampling distance and beam-widths match to obtain the best trade off between sampling density and resolution. For smoother fields (Figure 6.5b) this symmetry disappears and the highest information content is obtained with narrow beams across the entire range of sampling options. Note, however, that the dynamic range of information content is much smaller here because all configurations sample smooth fields rather well.

If the non-linear model is chosen (Figure 6.6a) higher information content is obtained when the sampling distance is equal or smaller than the beam-width, *i.e.* for configurations where the field is oversampled. Since z_s is 5 km this effect is stronger for smaller distances and beam-widths (less than 25 km). This is the consequence of the non-linear model producing spatially sharper sensitivity structures than the linear model where, given a certain beam-width, oversampling the footprints has a higher chance to capture the location of small-scale events. Lastly, Figure 6.6b confirms the observation made from Figure 6.3b, namely that for spatially uncorrelated observation errors wider beams are of advantage with little dependence on sampling distance.

6.4 Conclusions

A simple model for the evaluation of the best configuration of spatial sampling and spatial resolution of microwave radiometers for the sounding of spatially varying geophysical fields has been developed. The method is based on a one-dimensional, parametric geophysical model that produces precipitation-like patterns of adjustable spatial variability and that is sampled by a radiometer with idealized Gaussian-

shaped gain functions. The evaluation is based on linear estimation theory and uses information content (entropy reduction) to quantify the optimal sampling / resolution configuration. The model requires assumptions on error characteristics related to the geophysical state before and after the radiometric 'observation' is available. The analysis of sampling / resolution options depends crucially on spatial correlation that is contained in the geophysical state through an a priori state covariance matrix as well as the observation error covariance matrix. These correlations were defined as a function of the geophysical state and its spatial correlation and as a function of the spatial overlap of neighbouring observations, respectively.

The model has been tested with a linear and non-linear observation operator, for geophysical fields with little and large spatial variability, and with or without spatial correlation in the observation error covariance matrix. The results confirm common thinking in that non-linear models and increased spatial variability enhance the sensitivity of the results to spatial sampling / resolution and that spatially correlated observation errors, *i.e.* through overlapping neighbouring observations (oversampling), is very important for the trade-off between resolution and sampling. For highly variable geophysical fields such as convective rainfall, uncorrelated errors favour large beam-widths regardless of sampling distance while for smooth fields small beam-widths are favoured with little dependence on sampling. Highly non-linear sensitivity of the observation to changes in the geophysical field produces higher information content when moderate oversampling is achieved.

The presented combinations were not optimized any further since the employed modeling framework is not estimated to be accurate enough to justify a more detailed analysis. It nonetheless provides a simple and robust method for characterizing the first order requirements of sampling and resolution. The evaluation could only be enhanced by true geophysical parameter fields; however, the definition of geophysical state and observation spatial error covariances is very difficult and would most likely be based on similar assumptions as employed here.

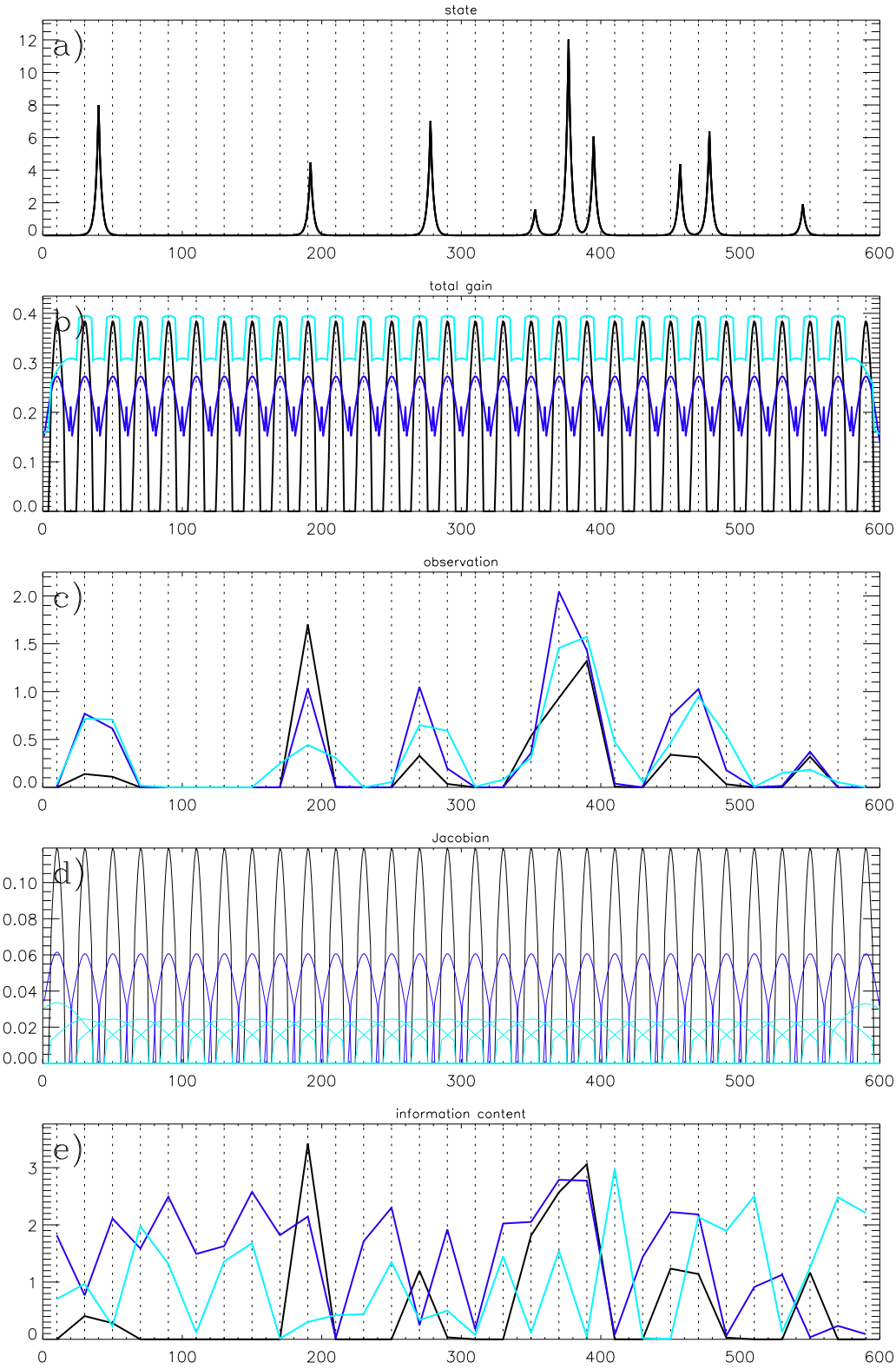

Figure 6.1: Example of model calculations for state vector **x** *(a), antenna gain g (b), observation vector* **y** *(c), Jacobian matrix* **H** *(d), and information content ER (e) for linear model case and non-diagonal* **R** *with $z_s = 2$km; antenna beam-widths of 10 (black), 20 (dark blue) and 50 km (light blue).*

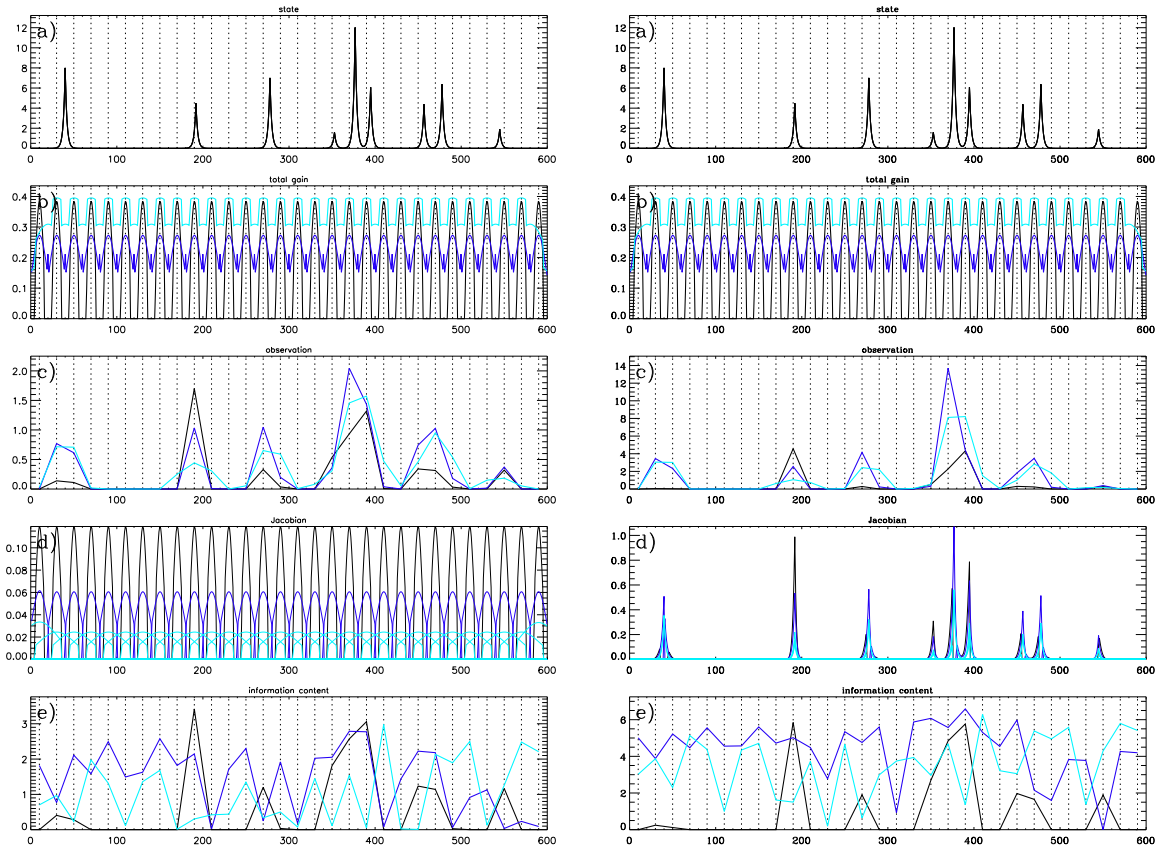

Figure 6.2: As Fig. 6.1 for non-diagonal **R** *and linear (left panels) vs non-linear model (right panels) model.*

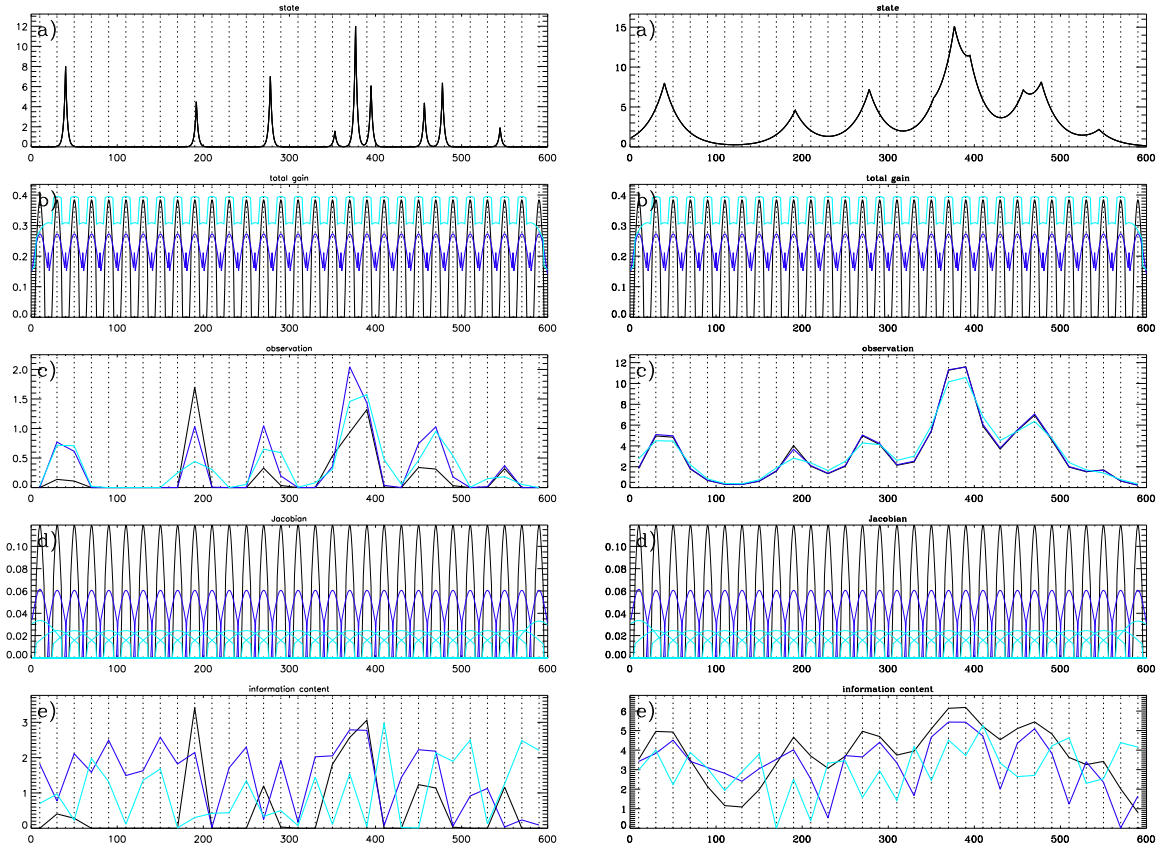

Figure 6.3: As Fig. 6.1 for non-diagonal **R**, *linear model and* z_s *= 2 km (left panels) vs* z_s *= 20 km (right panels) model.*

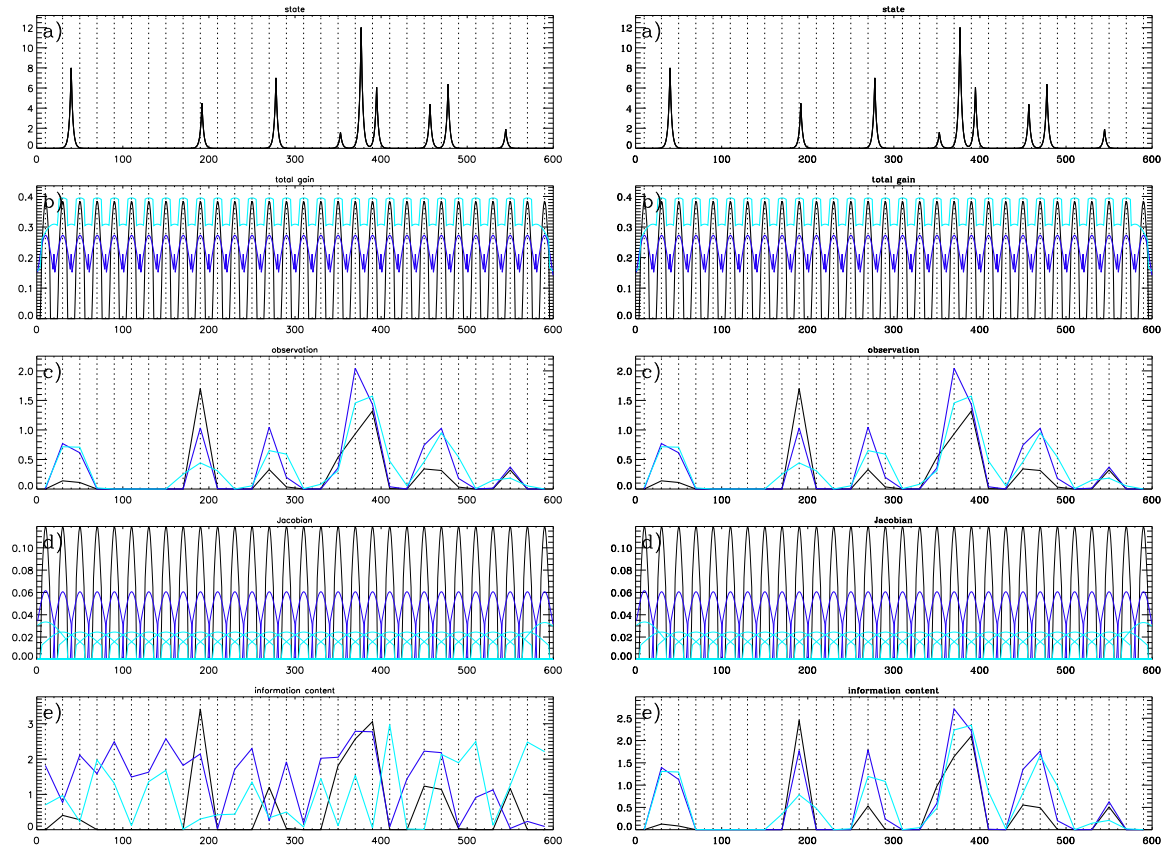

Figure 6.4: As Figure 6.1 for linear model, z_s = 2 km and non-diagonal (left panels) vs. diagonal (right panels) **R**.

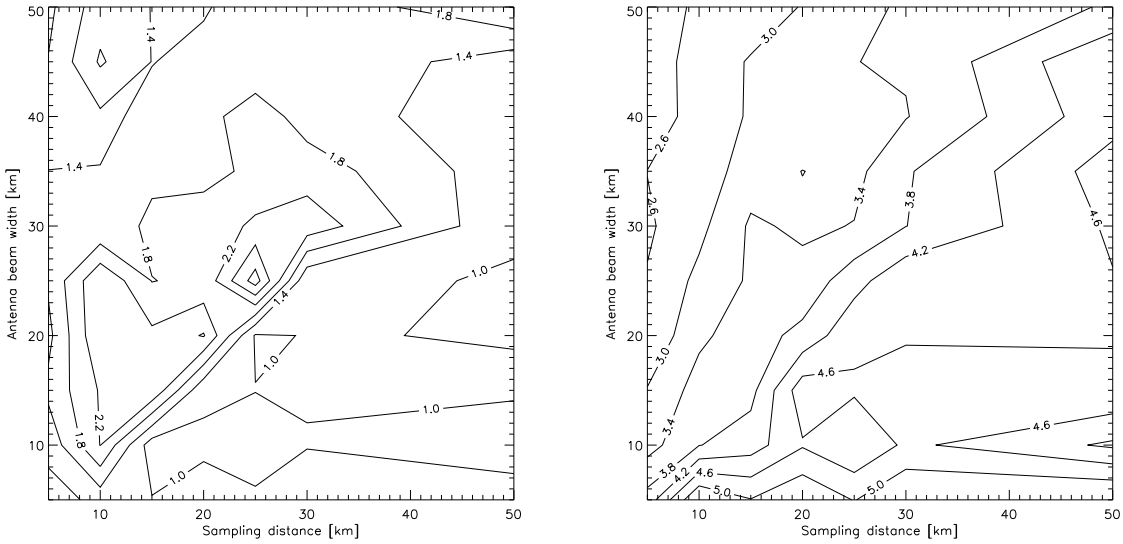

Figure 6.5: Mean along-scan ER for sampling distance options of 5, 10, 15, 20, 25, 30, 50 km and half-beam widths of 5, 10, 15, 20, 25, 30, 35, 40, 45, 50 km (100 cases). The linear model was used with non-diagonal **R** *and z_s of 5 km (a) and 50 km (b).*

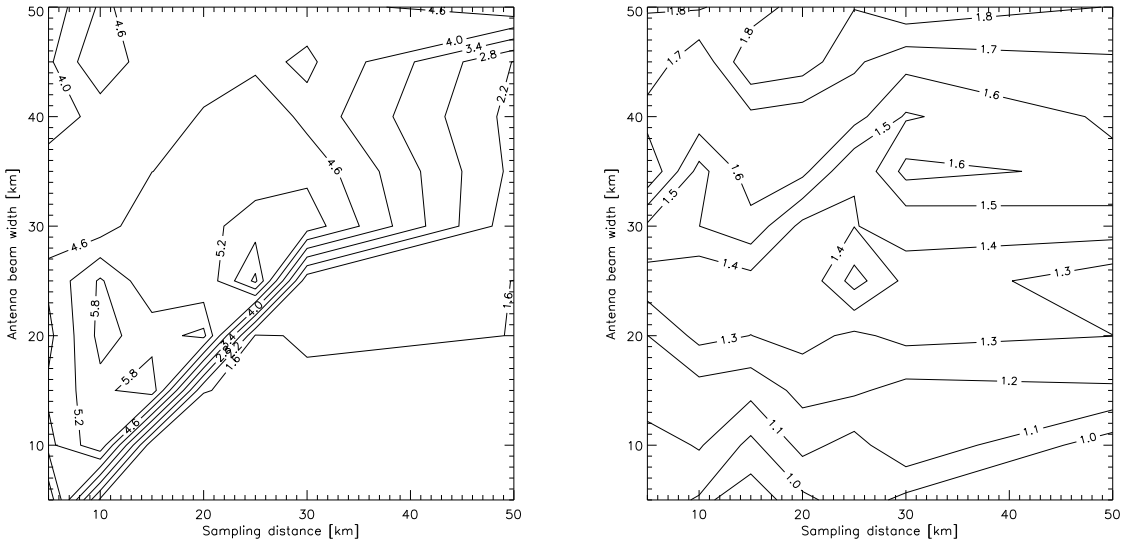

Figure 6.6: As Figure 6.5 for z_s of 5 km and non-linear model / non-diagonal **R** *(a) and non-linear model / diagonal* **R** *(b).*

7 Evaluation of F-18 SSMIS (WP6100 and WP6200)

7.1 Introduction

The Special Sensor Microwave Imager/Sounder (SSMIS) is the primary platform of the US Defense Meteorological Satellite Program (DMSP) and succeeds the Special Sensor Microwave Imager (SSMI) instruments flown on DMSP platforms F-08 - F-15 launched in the period 1987 - 1995. SSMIS combines a set of traditional imager channels (19 - 91 GHz, as well as a channel at 150 GHz) with thirteen temperature sounding channels and three water vapour sounding channels centred on the 183 GHz water vapour absorption line. The complementarity of these channel groups offers the possibility of extending the benefits realised from the assimilation of microwave radiances in clear skies to regions affected by cloud and precipitation.

The first satellite in the SSMIS series, F-16, was launched in October 2003. Post-launch analysis of the F-16 observations, using NWP fields and radiative transfer modelling, revealed that the F-16 observations were affected by two significant systematic errors. Firstly, the main reflector of the instrument was found to be emissive, with a frequency dependent emissivity ranging from 1.5% at 54 GHz to 4% at 183 GHz. The orbitally dependent heating of the main reflector coupled with the non-zero emissivity resulted in complex biases of amplitude 1.0-1.5K in the temperature sounding channels, where the orbital radiometric stability requirements are around 0.05K. The placement of the thermistor (coupled to the support arm of the radiometer) precluded the use of measured temperatures to correct for the emissivity effects and thermal modeling was required to provide an estimate of the face temperature of the instrument in order to correct the observed radiances. A second serious systematic bias affecting the F-16 observations was related to solar intrusions into the warm calibration target. This effect caused transient anomalies in the radiometer gain estimation which affected 40% of each orbit, and showed complex seasonal dependency. A fourier filtering technique was used to provide improved estimates of the gain during the anomalies and thereby improve to coverage provided by useful data. Averaging of the data provided significant reductions in the effective radiometric noise levels and F-16 temperature sounding data has been assimilated at several NWP centres (UK Met Office, JMA and NRL) until recently.

F-17 SSMIS was launched in November 2007 and has several modifications to partly reduce the effect of the biases evident in the F-16 data: the thermistor was placed at the centre of the shell of the main reflector to improve estimates of the reflector face temperature. In addition, a fence was placed around the top deck of the instrument to prevent direct solar intrusions into the warm load. These modifications partially helped correct the data but the emissive reflector problem remained. The imager channels of F-17 (channels 12-18), less severely affected by the reflector emission, have been assimilated operationally at ECMWF since the CY36R4 model upgrade of 9th November 2010.

In the meantime, during the period 2007-2008, significant advances were made in the pre-launch measurement of reflector characteristics and it was confirmed from samples of the SSMIS reflectors that the roughening process applied to the graphite shell of the reflector resulted in a significant reduction in the effective conductivity of the Aluminium coating applied to the roughened graphite surface (S. Brown, *pers. comm.*). The same measurement technology was also used to identify a spare reflector which had significantly lower emssivity than that planned for use with F-18 and hence the F-18 reflector was replaced by this spare, which was anticipated to result in near ideal performance.

It was therefore expected that F-18 would provide significantly higher quality data than its predecessors and some of the potential benefits of colocated imager and sounder data could be realised. Section 7.2 describes the aims of this workpackage, Section 7.3 describes the evaluation of the F-18 data, focussing

on the lower atmospheric temperature sounding channels and the imager channels. Section 7.4 describes the results of a series of seven observing system experiments aimed at assessing the performance of the F-18 data relative to that from MetOp-A AMSU-A. Conclusions are drawn in Section 7.5.

7.2 Aim of the study

The first part of this workpackage (**WP6100**) aimed to assess the quality of the F-18 data through a comparison with NWP short range forecast (*first guess*) fields, focussing on the quality of the lower atmospheric temperature sounding channels and the imager channels that are subsequently used in the OSEs described in Section 7.4. This formed the basis of the first component of this workpackage (**WP6100**).

Following this, in **WP6200**, a series of OSEs were designed and run to address the following questions:

- Can a well calibrated conical sounder deliver the same impact in an NWP system as the well established cross track instruments ?
- Can a conical sounder provide useful enhancements in the analysis of lower tropospheric temperatures ?
- Can the addition of imager channels to a suite of temperature sounding channels enhance analysis and forecast accuracy ?

7.3 Evaluation of F-18 Data

F-18 data has been received at ECMWF in late June 2010 and has been archived since 12 July 2010. As the most critical test of the effectiveness of the new (low emissivity) reflector first guess departures for the lower atmospheric temperature sounding channels were examined in detail. Figure 7.1 shows the first guess departures for channel 4 (54.4GHz). The first guess departures were generated using the *all-sky* assimilation system recently developed at ECMWF. For historical reasons related to errors in the calculation of surface emission and the limited value of imager data at high latitudes the coverage of the data for which departures have been computed is limited to the latitude range 60°S to 60°N. Figure 7.1 shows that the descending node of F-18 SSMIS for this channel is biased negatively relative to the ascending node. The amplitude of this bias is approximately 0.7K. As first guess departures for tropospheric and lower stratospheric temperature sounding channels on the AMSU-A instrument are around 0.15-0.20K, consistent with model background errors (in observation space) of approximately 50mK, an uncorrected bias of 0.7K is a very significant problem.

Figures 7.2 shows a 2D histogram of first guess departures for channel 4 (54.4 GHz) plotted as a function of scanline. This figure was generated from six consecutive assimilation cycles over the period 20 - 22 August 2010, which therefore include around 45 successive orbits of SSMIS data. These figures show that the bias is reproducible from orbit to orbit. The effect is evident for all temperature sounding channels examined (1-7) and can be detected in analogous plots for the imager channels, although geophysical variability makes it more difficult to discern the effect. Indications from the SSMIS Cal/Val team (S. Swadley, *pers. comm.*) are that the bias is caused by thermal gradients in the warm calibration target caused by thermal forcing from tape on the otherwise reflective top deck of the instrument. This tape was put in place to reduce the impact of indirect solar intrusions into the warm load. It appears the emissive tape undergoes significant orbital thermal cycling and this varies the radiative forcing on the warm calibration target surface. The resulting temperature cycling of the target surface is not accurately

monitored by thermistors in the load substrate, and this causes erroneous gain estimates. Mitigation is made difficult because the solar heating of the tape is modulated by obscurations on the platform. For example, the partial recovery of the bias around scanline 1500 is evident before the bias increases again.

As shown in Figure 7.2, the existing variational bias correction (VarBC) scheme at ECMWF, which permits a correction based on a solar hour predictor, partially compensates for the ascending - descending bias, at the cost of introducing some errors in the (otherwise good) ascending data. The bottom panels of Figure 7.2 show that if the ascending node, for which the errors are small, is selected and VarBC is applied to this data, then the resulting departures are unbiased for all scanline bins. This finding was used in the design of the OSEs described below in Section 7.4.

Figure 7.4 shows the mean and standard deviation of the bias corrected first guess departures for the F18 temperature sounding channels for both the global dataset (light grey bars) and the ascending node only (black bars). For channels 3-7 the standard deviations of the departures are in the range 0.13 - 0.19 K, close to or below those for AMSU-A. The residual biases are below 70mK (channel 7). Figure 7.4 also shows the mean and standard deviation of the first guess departures for the imager channels (12-18).

7.4 Observing System Experiments

7.4.1 Set up

In order to address the questions outlined in Section 7.1 OSEs described below in Table 1 were set-up and run:

EXPERIMENT	Description	ECMWF expt id
BASE	1 AMSU-A only (N-19), no AIRS/IASI	fftj
METOPA	BASE + MetOp-A AMSU-A	fftk
F18-3to7	BASE + F18 channels 3-7 ascending only	fge4
METOP-ASC	BASE + MetOp-A AMSU-A ascending only	fge7
F18-1to7	BASE + F18 channels 1-7 ascending only	fgf6
F18-imager	F18-1to7 plus (12-18)	fgf7
FULL	Full system	ffth

Table 1: Observing System Experiment set-up to assess the performance of F18 SSMIS.

The baseline experiment (**BASE**) excluded data from all AMSU-A instruments, with the exception of NOAA-19 AMSU-A which was retained in order to provide some level of constraint on the evolution of the large scale flow. NOAA-19 is in an afternoon orbit which ensured the data provided by MetOp-A AMSU-A and F-18 SSMIS was complementary to the NOAA-19 data. In these experiments, designed to compare the performance of F-18 with MetOp-A, the exclusion of most microwave sounding data as well as the data from the advanced IR sounders should ensure the positive impact of the data under evaluation was measureable. The full system experiment (**FULL**) was designed to provide a *calibration* and a context for the results obtained.

The experiments **METOPA** and **METOP-ASC** were designed to provide two *fair* tests of the relative performance of SSMIS and MetOp-A. **METOPA** provided full global coverage using the channel set currently active in the operational use of the data. This provided the first fair comparison of AMSU-

A and F18 lower atmospheric temperature sounding channels: a fully operational AMSU-A *versus* a limited coverage SSMIS. **METOP-ASC** used data only from the ascending node of MetOp-A as shown in Figure 7.3. Only data within the latitude range 60°S to 60°N was used to best match the SSMIS data coverage obtained in **F18-3to7**. This experiment offered a second *fair* comparison of MetOp-A and AMSU-A data.

F18-1to7 additionally included SSMIS channels 1 (50.3 GHz) and channel 2 (52.8 GHz) to test the second of the questions raised in Section 7.2. **F18-imager** used the imager channels (12-18) from SSMIS in addition to channels 1-7. A comparsion of **F18-1to7** with **F18-imager** tests the benefit of the addition of imager channels to a suite of temperature sounding channels.

7.4.2 Results

A very sensitive indication of the impact of the data on short range forecast accuracy is provided by the fit of short range forecast (first guess) fields to other observation types, particularly radiance observations which provide a very large data sample. Figure 7.5 shows the fit of the first guess to AMSU-A radiances from NOAA-19, a sensor which was common to all of the experiments analysed here. Over the 3 month period analysed, the NOAA-19 observation count ranges from 2.5 million for channel 5 to 4.2 million for the highest peaking channels (12-14). To provide context Figure 7.5 shows the **FULL** experiment reduces the standard deviation of first guess departures by 3% - 8% relative to that obtained in the **BASE** experiment. The next most significant improvement is provided by the **METOPA** experiment which provides approximately 50-70% of the reduction provided by the **FULL** experiment. The impact of the remaining experiments is relatively small for channels 9-14, with **METOP-ASC** being the most significant of this group.

For NOAA-19 channels 5 and 6 the SSMIS experiments are more competitive with the MetOp experiments. For channels 5 and 6 in particular, the lowest peaking chanels used over ocean in the ECMWF operational system, the F-18 SSMIS experiments outperform the **METOP-ASC** experiment. The magnitude of the reduction is 0.25-0.5% relative to the baseline experiment. This is an encouraging sign, with small benefits as expected in the lower troposhere.

Figure 7.6 shows the change in RMS errors in geopotential for the 1000hPa, 700 Pa, 500 hPa and 200 hPa levels. The largest impacts are, as expected for the **METOPA** experiment, amounting to error reductions of 3-8% for short range forecasts to day 3 in the SH. For the NH impacts are less at 1-4% but the **METOPA** experiment outperforms all of the F18 experiments. **METOP-ASC** shows the next most significant benefit in the SH, albeit 4-5 times lower than the benefit from **METOPA**. In the NH **METOP-ASC** shows slight negative impact of up to 1% for the levels 1000-500 hPa at T+12 hours. In the NH the F18 experiments are more competitive with the **METOP-ASC** experiment. Some significant positive impacts of 1-2% for forecast days 2-5 are observed in the F18 experiments with **F18-3to7** usually outperforming the **F18-1to7** and **F18-imager** experiments.

7.5 Conclusions

Despite the improvements in F-18 SSMIS data through improved pre-launch characterisation of the reflector emissivity a new type of bias has hampered efforts to perform a *like-for-like* comparison of the performance of the SSMIS conical instrument with the established AMSU-A cross track instruments, and to assess fully the benefits to be realised from the complementarity of colocated imaging and sounding channels. The new bias is believed to result from radiative forcing of the warm calibration target

from tape put in place on the top deck of the instrument to mitigate the effects of indirect (reflected) solar intrusions into the warm load. The effect of this radiative forcing is to introduce errors in the gain estimation which introduce a bias into most of the descending node of the F-18 data, for the channels examined here (1-7, 12-18). The maximum amplitude of this bias is around 0.7K.

The variational bias corection scheme partly compensates for this effect, but the residual localised biases prevent the data from being used meaningfully in the subsequent observing system experiments. If the descending node observations are eliminated prior to bias correction then the resulting data is of good quality and this subset of the F-18 data was used in the subsequent OSEs.

For the OSEs, two ”fair” comparisons were made against MetOp-A AMSU-A: in the first full coverage AMSU-A data was compared againt the limited coverage (ascending node only, latitude range limited to 60°S to 60°N) F-18 data. Results for the MetOp-A experiments were very significantly more positive than for F-18. In the second experiment, the MetOp-A data coverage was restricted to match the F-18 data. The impacts from the MetOp-A experiment in the southern hemisphere, especially at short range, are better than that from F-18, although the F-18 impacts are neutral to slightly positive. First guess departure fits indicate that although MetOp-A outperforms F-18 SSMIS from the mid-troposphere upwards F-18 outperforms MetOp-A in the lowermost parts of the atmosphere, in these experiments.

In future, an extension of the *all-sky* scheme to higher latitudes would partially offset the relative mismatch in coverage and make a fairer comparison possible. In addition, the exploitation of some of the higher peaking SSMIS channels (19-24) would improve the match between the vertival coverage between SSMIS and AMSU-A and permit a fairer comparison.

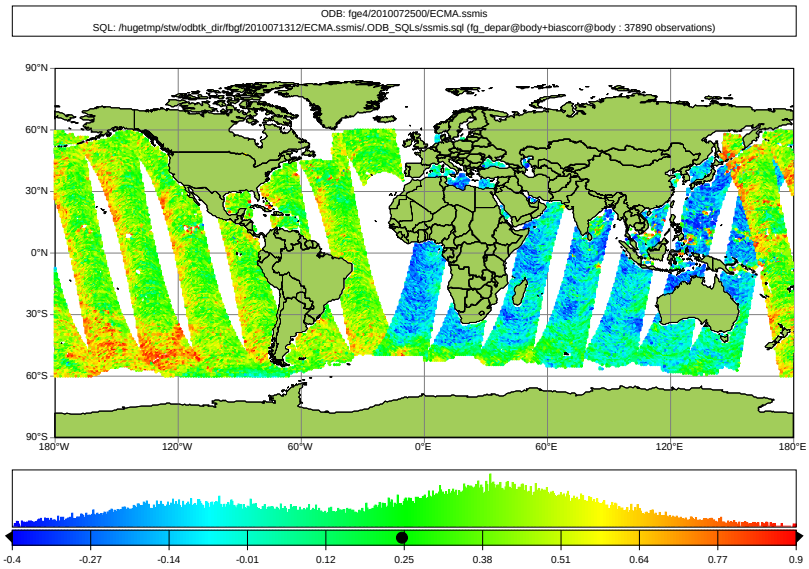

Figure 7.1: First guess departures (in K) for F-18 SSMIS Channel 4 (54.4 GHz) before variational bias correction for both ascending and descending nodes.

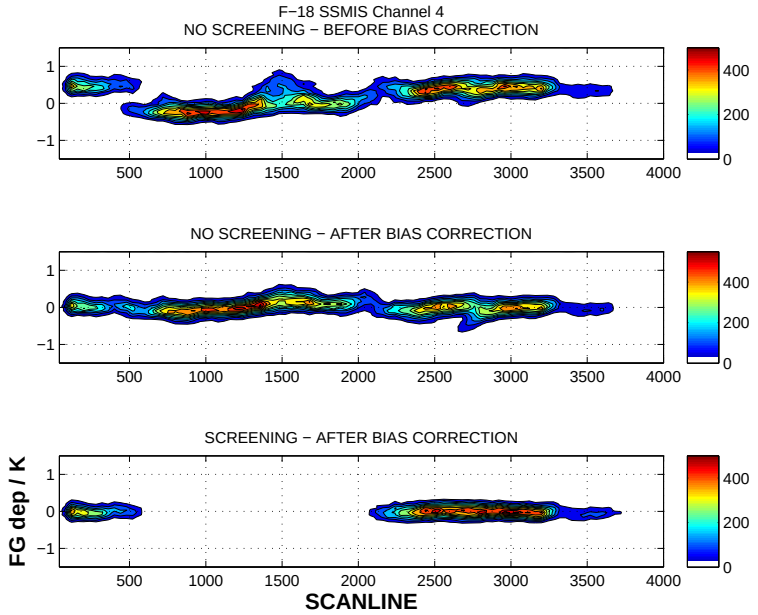

Figure 7.2: 2D historgams of first guess departures versus scanline for 3 days (20-22 August 2010) for channel 4 showing the effect of the radiative forcing of the warm calibration target (depressed FG departures for scanlines 500 - 2000. The top panel shows the uncorrected first guess departures. The middle panel shows the effect of bias correcting all data, and the lower plot shows the result of screening out data from the descending node and bias correcting the remaining observations.

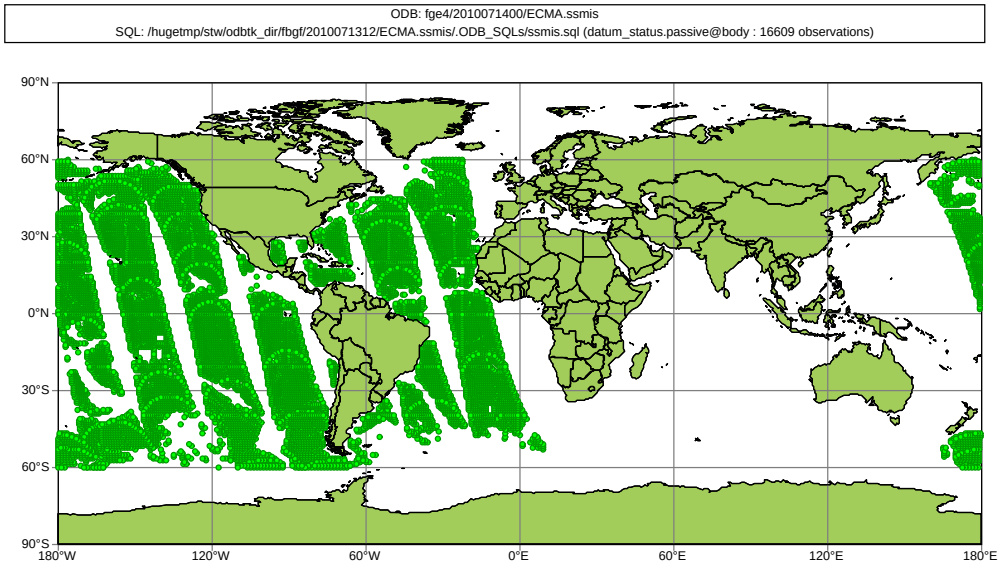

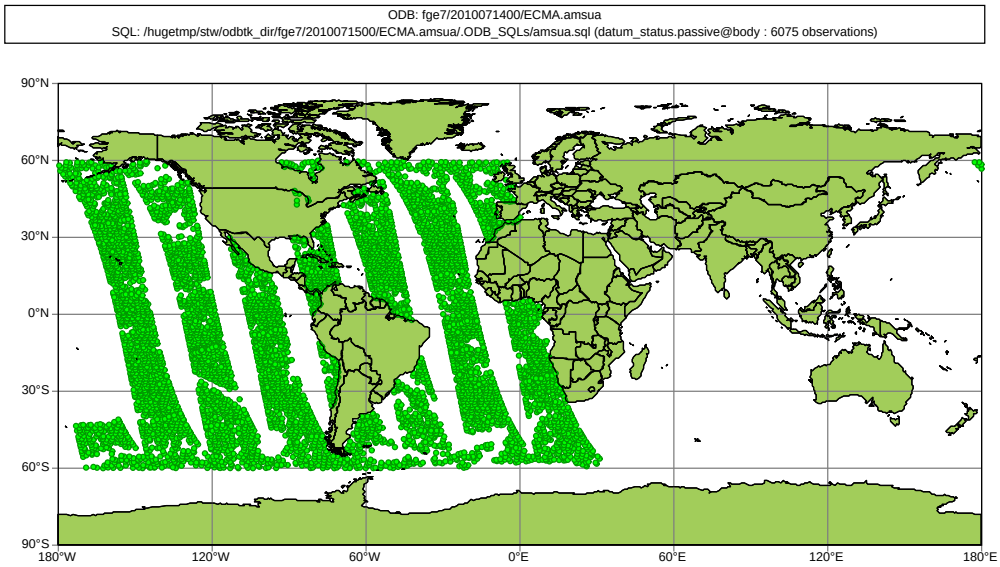

Figure 7.3: Typical data coverage from F-18 SSMIS (top) and MetOp-A (bottom) in a 12 hour assimilation cycle, for the experiments where only ascending node data is used for both sensors. Note the apparent superior coverage from SSMIS due to the blacklisting of (3) observations at the edge of the AMSU-A swath.

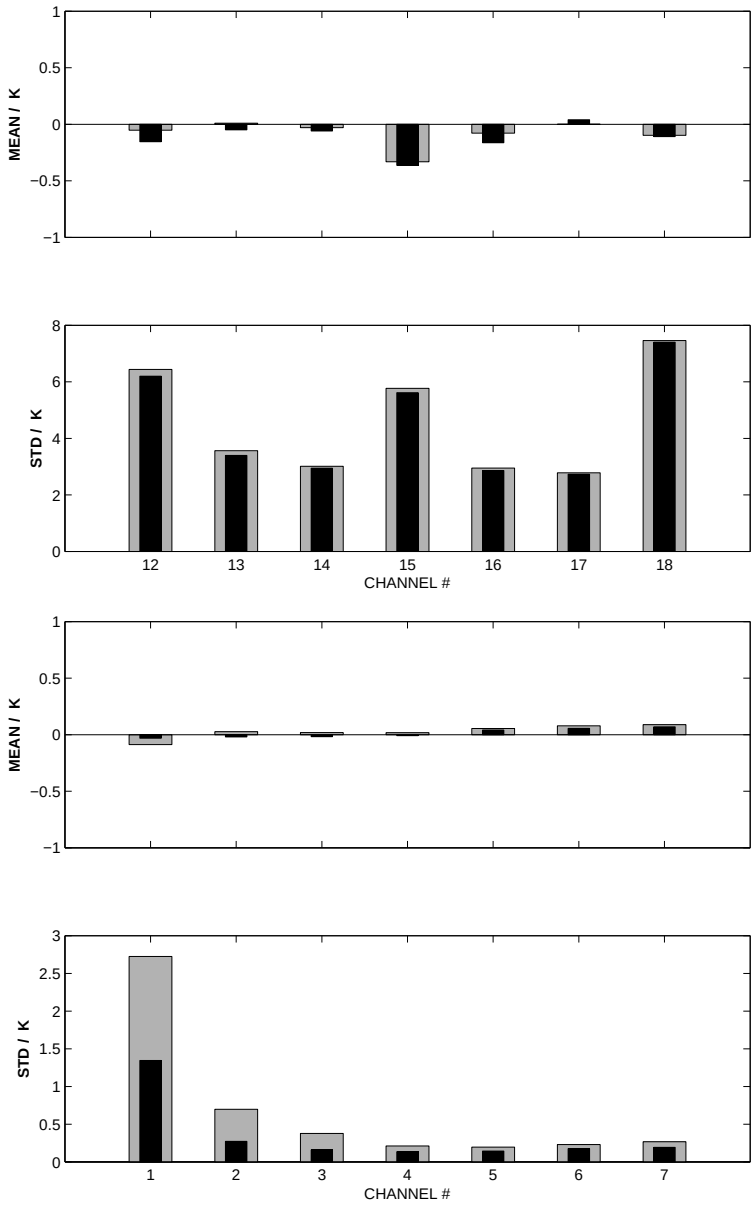

Figure 7.4: Mean and standard deviations for SSMIS imager channels 12-18 (top) and the temperature sounding channels (1-7, bottom). The grey bars show the statistics for the bias corrected global dataset including ascending and descending node data. The black bars show the statistics for bias corrected data using only the ascending node data.

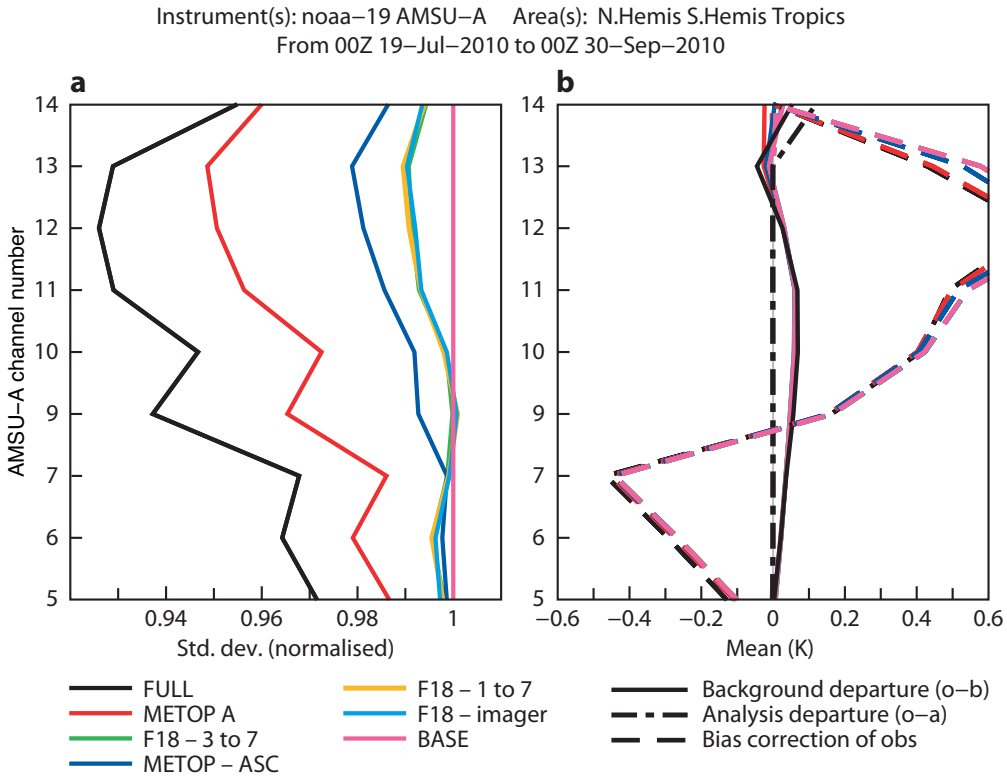

Figure 7.5: The panel on the left **(a)** *shows the normalised standard deviations of first guess departures for NOAA-19 AMSU-A over the period 17 July - 16 August 2010. Ther normalisation is relative to the departures for the* **BASE** *OSE. The right panel* **(b)** *shows the bias corrections applied.*

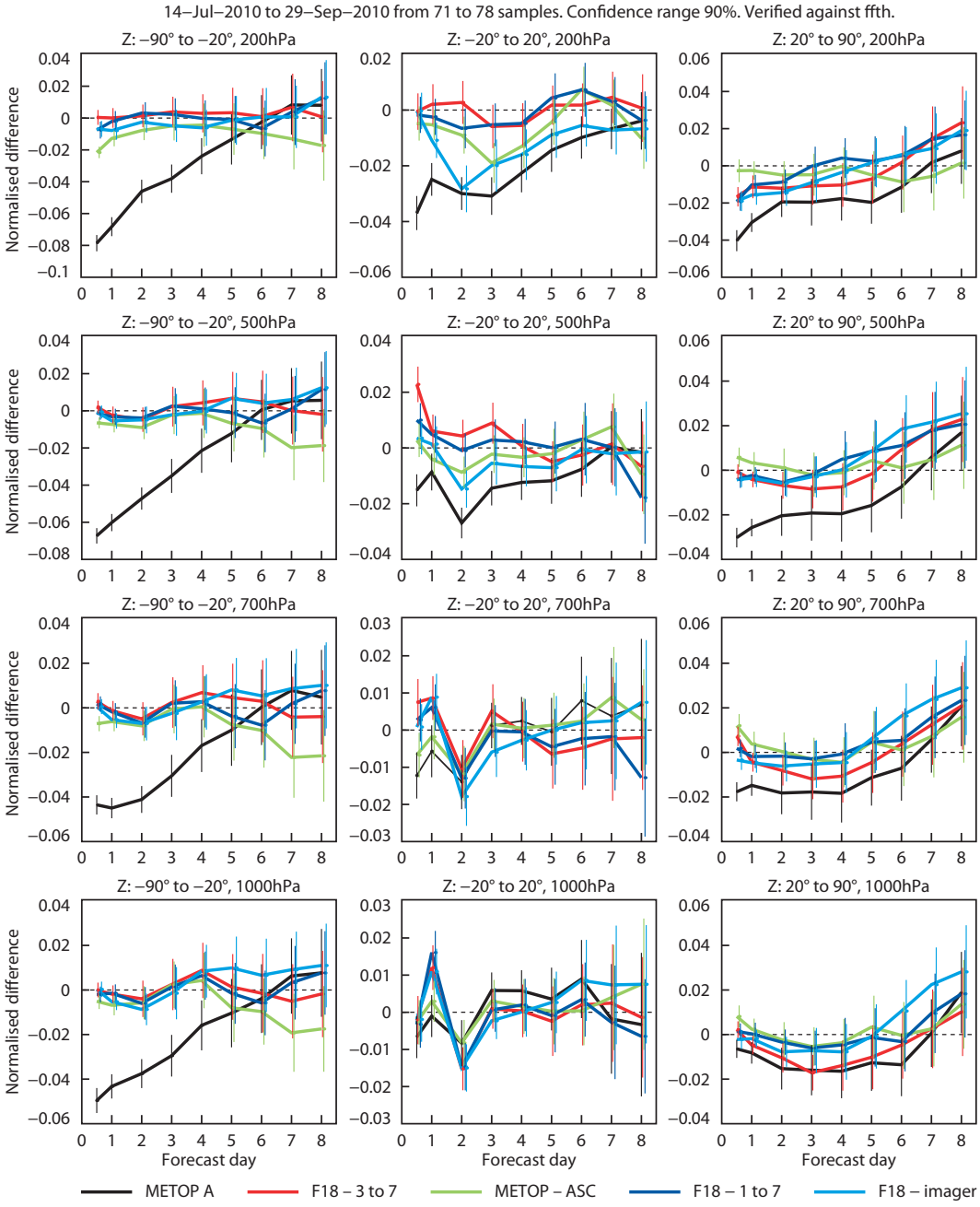

Figure 7.6: Normalised difference in RMS errors in geopotential for SH (left), tropics(middle) and NH (right) for levels from 200 hPa (top) to 1000hPa (bottom) for the OSEs described in Table 1.

Acknowledgements

The authors gratefully acknowledge the support of EUMETSAT through Contract EUM/CO/09/4600000629/PS and like to thank Gene Poe, Steve Swadley and Bill Blackwell for their advice on WP3200 concerning cross polarisation effects in microwave imagers. Rob Hine and Anable Bowen provided many of the figures included in this report.

8 References

Auligné T, McNally AP, Dee DP, 2007. Adaptive bias correction for satellite data in a numerical weather prediction system. *Q. J. R. Meteorol. Soc.* **133**, 631-642

Anderson, E. P. and al., 2005: Assimilation and Modelling ofthe Hydrological Cycle. *Bull. Amer. Meteorol. Soc.*, **86**, 387-402.

Bauer, P. and Di Michele S., 2007: Mission requirements for a post-EPS Microwave Radiometer, *EUMETSAT Contract No. EUM/CO/06/1510/PS*

Bauer, P., P. Lopez, A. Benedetti, D. Salmond, and E. Moreau, 2006a: Implementation of 1D+4D-Var assimilation of precipitation affected microwave radiances at ECMWF, Part I: 1DVar, *Q. J. R. Meteorol. Soc.*, 132, 2277-2306.

Bauer, P., P. Lopez, A. Benedetti, D. Salmond, S. Saarinen, and M. Bonazzola, 2006b: Implementation of 1D+4D-Var assimilation of precipitation affected microwave radiances at ECMWF, Part II: 4D-Var,*Q. J. R. Meteorol. Soc.*, 132, 2307-2332.

Chevallier, F., 2002: Sampled database of 60 levels atmospheric profiles from the ECMWF analysis, *NWPSAF Tech. Rep. No4.*

Chu, T and Turrin, R.H., 1973: Depolarization properties of offset reflector antennas. *IEEE Trans. Antennas Propagat.*, vol. AP-21, pp. 339-345.

Cook J.S., Elam, E.M. and Zucker, H., 1965: The open Cassegrain antenna: Part I-Electromagnetic design and analysis. *Bell Syst. Tech. J.*, vol. 44, pp.1255-1300.

Deblonde G. and S.J. English, 2001: Evaluation of the FASTEM-2 fast microwave oceanic surface emissivity model. *Tech. Proc. ITSC-XI Budapest*, 67-78.

DiMichele, S. and P. Bauer, 2006: Passive microwave radiometer channel selection based on precipitation information content estimation. *Q. J. Roy. Meteor. Soc.*, **132**, 1299-1323.

Eyre J.R., 1991: A fast radiative transfer model for satellite sounding systems. ECMWF Tech . Memo., 176., *available from* http://www.ecmwf.int.

Fourrié, N., and J.-N. Thépaut, 2003: Evaluation of the AIRS near-real-time channel selection for application to numerical weather prediction.*Q. J. Roy. Meteor. Soc.*,**128**, 2425-2439.

Karbou F., N.Bormann, J-N Thépaut, 2007: Towards the assimilation of satellite microwave observations over land: feasibility studies using SSMI/S, AMSU-A and AMSU-B. *NWP SAF Programme Research Report.*

Liebe, H.J., 1989: MPM-An atmospheric millimeter-wave propagation model, *Int. J. Infrared and Millimeter Waves*, 10, 631-650.

Lipton, A., 2003: Satellite sounding channel optimization in the microwave spectrum. *IEEE Trans. Geosci. Remote Sens.*, **41**, 761-781.

Moreau, E., J. Testud, E. Le Bouar, 2000: Rainfall spatial variability observed by X-band weather radar and its implication for the accurayc of rainfall estimates. 34th Conf. Radar Meteorol., P14.9, 5 pp.

Purser, R.J., and H.-L. Huang, 1993: Estimating effective data density in a satellite retrieval or an objective analysis. *J. Appl. Meteor.*, **32**, 1092-1107.

Rabier, F., N. Fourrié, D. Chafaï, and P. Prunet, 2002: Channel selection methods for Infrared Atmospheric Sounding Interferometer.*Q. J. Roy. Meteor. Soc.*, **128**, 1011–1027.

Rabier, F., 2005: Overview of global data assimilation developments in numerical weather-prediction centres.*Q. J. Roy. Meteor. Soc.*, **131**, 3215-3233.

Rodgers, C., 2000: Inverse methods for sounding, Theory and Practice. World Scientific Publishing, Singapore, New Jersey, London, Hong Kong.

Rudge, W., 1975: Multiple-beam antennas: Offset reflectors with offset feeds. *IEEE Trans. Antennas Propagat.*, vol. AP-23, pp. 317-322.

Saunders, R., 2008: RTTOV-9 science and validation report. NWP-SAF report NWPSAF-MO-TV-020.

AEG(AS), 2006: Position Paper - Post-EPS Developments on Atmospheric Sounding and Wind Profiling http://www.eumetsat.int/Home/Main/Satellites/PostEPS/Resources/index.htm

AEG(CPL), 2006: Position Paper - Cloud, Precipitation and Large Scale Land Surface Imaging (CPL)

http://www.eumetsat.int/Home/Main/Satellites/PostEPS/Resources/index.htm

AEG(LO), 2006: Position Paper - Requirements for Ocean Observations Relevant to post-EPS
http://www.eumetsat.int/Home/Main/Satellites/PostEPS/Resources/index.htm

ESA ESTEC Contract No.20711/07/NL/HE, 2008: Optimisation of the Oxygen and Water Vapour Sounding Channels Spectral and Radiometric Requirements for Cross Track and Conically Scanning Radiometers, Final Report, ECMWF.

ESA Contract No. 18101/04/NL/GS, 2005a: Development of an End-to-End Tool to Simulate the Performance of the European Contribution to the GPM Mission, Final Report, CNR/ISAC.

ESA Contract No. 17193/03/NL/GS, 2005b: Assimilation of Rain Observations at ECMWF in Preparation of EGPM, Final Report, ECMWF.

EUMETSAT Contract No. EUM/CO/06/1510/PS, 2006: Mission Requirements for a post-EPS Microwave Radiometer.

MRD, 2010: Post-EPS Mission Requirements Document, EUMETSAT Document,
No. EUM/PEPS/REQ/06/0043, Issue v3c, June 2010.
http://www.eumetsat.int/Home/Main/Satellites/PostEPS/Resources/index.htm

9 Appendix A: Parametrization coefficients for the drift in brightness temperature

channels	4	5	6	7	8	9	10
a	-0.1866E-4	0.1325E-1	0.2928E-4	0.1141E-4	0.4956E-5	-0.1038E-4	-0.4366E-4
s	-0.2561E+2	-0.1375E+2	0.9968E+1	0.9130E+0	0.6972E+0	0.3152E+0	0.3437E+1
g	0.3884E-3	0.1324E-1	0.4578E-4	0.3813E-4	-0.1389E-4	0.8143E-4	0.4037E-3
a*s	0.5570E+2	0.2116E+2	-0.9192E+1	0.2175E+1	0.1368E+1	0.5512E+0	0.5783E+0
g*s	-0.1605E+2	-0.2782E+2	-0.3847E+2	-0.1841E+2	-0.1687E+2	-0.1476E+2	0.7523E+1
g*a	-0.3493E-3	-0.5237E-2	-0.7688E-4	-0.5215E-4	0.1301E-4	-0.1213E-3	-0.4876E-3
g*s*a	0.1680E+2	0.1898E+2	0.1092E+2	-0.1040E+2	-0.1162E+2	0.2102E+1	-0.2211E+2
s^2	-0.2403E+2	0.4078E+3	0.1108E+3	0.1025E+3	0.9894E+2	0.1570E+2	0.3264E+3
s^2*a	0.2954E+2	-0.2973E+3	-0.6523E+2	-0.3674E+2	-0.5360E+2	0.3982E+2	0.1802E+2
s^2*g	-0.6300E+2	-0.5795E+3	-0.2708E+3	-0.1847E+3	-0.3203E+3	-0.7399E+3	-0.1066E+4
s^2*a*g	0.4867E+2	0.3590E+3	0.7123E+2	-0.5844E+2	0.8730E+2	0.2487E+3	-0.1084E+4
e	-0.1187E-4	-0.3179E-2	0.0000	0.0000	0.0000	0.0000	0.0000
a*e	0.1296E-3	0.5396E-2	0.0000	0.0000	0.0000	0.0000	0.0000
s*e	0.2221E+2	0.1491E+2	0.0000	0.0000	0.0000	0.0000	0.0000
g*e	-0.1023E-3	-0.3427E-3	0.0000	0.0000	0.0000	0.0000	0.0000
a*s*e	-0.5577E+2	-0.2628E+2	0.0000	0.0000	0.0000	0.0000	0.0000
g*s*e	0.8800E+0	0.3361E+1	0.0000	0.0000	0.0000	0.0000	0.0000
g*a*e	0.1622E-3	0.9113E-3	0.0000	0.0000	0.0000	0.0000	0.0000
g*s*a*e	-0.9472E+1	-0.7788E+1	0.0000	0.0000	0.0000	0.0000	0.0000
s^2*e	0.2543E+2	0.5975E+2	0.0000	0.0000	0.0000	0.0000	0.0000
s^2*a*e	-0.4105E+2	-0.1017E+3	0.0000	0.0000	0.0000	0.0000	0.0000
s^2*g*e	0.5344E+1	0.1811E+2	0.0000	0.0000	0.0000	0.0000	0.0000
s^2*a*g*e	-0.1193E+2	-0.3306E+2	0.0000	0.0000	0.0000	0.0000	0.0000
s^4	0.0000	0.0000	0.9340E+4	0.1255E+5	0.5858E+4	-0.4150E+3	0.1857E+5
s^4*a	0.0000	0.0000	-0.5364E+4	-0.8122E+4	-0.4334E+4	0.8364E+3	0.1421E+5
s^4*g	0.0000	0.0000	-0.1855E+4	0.3177E+4	-0.1096E+5	0.1775E+4	-0.6619E+5
s^4*a*g	0.0000	0.0000	-0.3449E+4	-0.5513E+4	0.1006E+5	-0.1265E+5	-0.7434E+0
K	-0.9065E-4	-0.2351E-1	-0.7214E-5	0.4233E-5	0.2823E-5	0.9868E-5	0.1259E-3

Table 1: Coefficients used in the parametrization of AMSU-A drift in brightness temperature. The corresponding parameters are in the first column: s=frequency shift, e=emissivity, a=cos(satellite zenith angle), g=temperature gradient (/43) weight-averaged by the weighting function for each channel, K=constant (in K).

channels	3
a	-0.6151E-2
s	0.2949E+0
e	0.3615E-2
a*s	0.5441E+0
e*a	0.3306E-2
e*s	-0.3618E+0
e*s*a	-0.5238E+0
g	0.2819E-2
g*s	-0.2393E+0
g*e	-0.2394E-2
g*a	0.2278E-2
e*g*s	0.1426E-1
a*g*e	-0.2157E-2
g*a*s	-0.4016E+0
g*e*a*s	0.5225E+0
w’	0.3291E-2
w’*a	-0.9037E-3
w’*s	-0.1895E+0
w’*a*s	-0.5611E-1
w’*e	-0.2497E-2
w’*e*a	0.5761E-3
w’*e*s	0.2962E+0
w’*e*a*s	-0.1852E-1
w’*g	-0.2253E-2
w’*g*s	0.6017E-1
w’*g*e	0.1613E-2
w’*g*a	0.6352E-3
w’*e*g*s	-0.1017E+0
w’*a*g*e	-0.3720E-3
w’*g*a*s	0.9418E-1
w’*g*e*a*s	-0.7068E-1
K	0.7617E-3

channels	4	5
a	-0.6845E-3	-0.2902E-3
s	0.3302E-1	0.1292E+0
e	-0.1643E-2	-0.7524E-3
a*s	0.4427E-1	-0.1298E+0
e*a	0.6627E-3	0.2807E-3
e*s	-0.7238E-1	-0.1389E+0
e*s*a	-0.2587E-1	0.1323E+0
w	-0.4557E-3	-0.1622E-3
n	-0.2148E-2	-0.1589E-2
a*n	0.4829E-2	0.4937E-2
a*w	0.1532E-3	0.6011E-4
e*n	0.2107E-2	0.1588E-2
e*w	0.4152E-3	0.1506E-3
s*n	0.1757E+1	0.6157E+1
s*w	-0.3938E-1	-0.4065E-1
w*n	-0.1112E-2	0.2621E-3
a*e*w	-0.1550E-3	-0.6405E-4
a*e*n	-0.4613E-2	-0.4870E-2
a*s*w	0.1177E-3	0.1937E-1
a*s*n	-0.1543E+1	-0.5788E+1
a*w*n	-0.2286E-2	-0.1710E-2
e*s*w	0.2655E-1	0.2076E-1
e*s*n	-0.1604E+1	-0.5911E+1
e*w*n	0.9651E-3	-0.2898E-3
s*w*n	-0.1650E+1	-0.2625E+1
a*e*s*w	-0.5062E-2	-0.2238E-1
a*e*s*n	0.1438E+1	0.5643E+1
a*e*w*n	0.2255E-2	0.1701E-2
a*s*w*n	0.2357E+1	0.2878E+1
e*s*w*n	0.1552E+1	0.2509E+1
a*e*s*w*n	-0.2246E+1	-0.2782E+1
K	0.1576E-2	0.7556E-3

Table 2: Coefficients used in the parametrization of MHS drift in brightness temperature. The corresponding parameters are in the first column: s=frequency shift, e=emissivity, a=cos(satellite zenith angle), g=temperature gradient (/43) weight-averaged by the weighting function for each channel, w’=water vapour column (x1.61) weight-averaged by the weighting function for each channel, w=log(total water vapour column x1.61), n=Gaussian parameter (see section 3.1), K=constant (in K).